UNIVERSIDAD DE CHILE
FACULTAD DE CIENCIAS FÍSICAS Y MATEMÁTICAS
DEPARTAMENTO DE INGENIERÍA MECÁNICA

SPLINE-BASED METHODS WITH ADAPTIVE REFINEMENT FOR PROBLEMS OF ACOUSTICS AND FRACTURE MECHANICS OF THIN PLATES

TESIS PARA OPTAR AL GRADO DE
MAGÍSTER EN CIENCIAS DE LA INGENIERÍA, MENCIÓN MECÁNICA

JAVIER ANDRÉS VIDELA MARIÓ

PROFESOR GUÍA:
ELENA ATROSHCHENKO

MIEMBROS DE LA COMISIÓN:
ALEJANDRO ORTIZ BERNARDIN
VIVIANA MERUANE NARANJO

SANTIAGO DE CHILE
2018

RESUMEN DE LA MEMORIA PARA OPTAR
AL TÍTULO DE MAGÍSTER EN CIENCIAS DE LA INGENIERÍA, MENCIÓN MECÁNICA
POR: JAVIER ANDRÉS VIDELA MARIÓ
FECHA: 2018
PROF. GUÍA: ELENA ATROSHCHENKO

SPLINE-BASED METHODS WITH ADAPTIVE REFINEMENT FOR PROBLEMS OF ACOUSTICS AND FRACTURE MECHANICS OF THIN PLATES

Both the CAD software and FEM software have a significant impact on engineering nowadays. Even though both are powerful tools for design and analysis, the main drawback is that CAD geometries and Finite Element models do not entirely match, which results in the necessity to re-parameterize the geometry many times during the solution cycle in FEM. Isogeometric Analysis (IGA) was proposed to fulfill this gap and create the direct link between the CAD design and FEM analysis. The main idea of IGA is to substitute the shape functions used in FEM by the shape functions used in the CAD software.

In particular, one of the main drawbacks of NURBS basis functions, and therefore of IGA, is the lack of local refinement, which makes them computationally highly expensive in applications that demands a non-uniform refinement of the geometry. Polynomial splines over Hierarchical T-meshes (PHT-splines) were introduced by Deng et al. as a type of spline that allows local refinement and adaptability by means of a polynomial basis capable of parameterizing the geometry.

In this work, we demonstrate the application of PHT-splines for two type of problems: time-harmonic acoustic problems, modeled by the Helmholtz equation, and fracture mechanics of thin plate problems, modeled by the Kirchhoff-Love theory.

Solutions of the Helmholtz equation have two features: global oscillations associated with the wave number and local gradients caused by geometrical irregularities. The results show that after a sufficient number of degrees of freedom is used to approximate global oscillations, adaptive refinement can capture local features of the solution. The residual-based and recovery-based error estimators are compared and the performance of p-refinement is investigated.

Moreover, an eXtended Geometry Independent Field approximaTion (XGIFT) formulation based on Polynomials Splines Over Hierarchical T-meshes (PHT-splines) for modeling both static and dynamic fracture mechanic problems for plates described by the Kirchhoff-Love theory is presented. Adaptive refinement is employed using a recovery-based error estimator. Results show that adaptive refinement can capture local features of the solution around the crack tip, improving results in both static and dynamic examples.

In both cases, the simulations are done in the context of recently introduced Geometry Independent Field approximaTion (GIFT), where PHT-splines are only used to approximate the solution, while the computational domain is parameterized with NURBS. This approach builds on the natural adaptation ability of PHT-splines and avoids the re-parameterization of the NURBS geometry during the solution refinement process.

RESUMEN DE LA MEMORIA PARA OPTAR
AL TÍTULO DE MAGÍSTER EN CIENCIAS DE LA INGENIERÍA, MENCIÓN MECÁNICA
POR: JAVIER ANDRÉS VIDELA MARIÓ
FECHA: 2018
PROF. GUÍA: ELENA ATROSHCHENKO

SPLINE-BASED METHODS WITH ADAPTIVE REFINEMENT FOR PROBLEMS OF ACOUSTICS AND FRACTURE MECHANICS OF THIN PLATES

Tanto los programas de Diseño Asistido por Computadora (CAD) como las herramientas de análisis por medio del Método de Elementos Finitos (FEM) han tenido un enorme impacto en la actividad ingenieril en las últimas décadas. Aun así, tienen la desventaja de que las geometrías CAD no son directamente compatibles con las geometrías utilizas en FEM, lo cual resulta en la necesidad de re-mallar la geometría varias veces durante un ciclo de soluciones FEM. Para solucionar esto, el Análisis Isogeométrico (IGA) ha sido propuesto como una metodología capaz de generar un vínculo directo entre el diseño mediante CAD y el análisis FEM. La principal idea dentro de IGA es sustituir las funciones de forma utilizadas en FEM por las funciones de base que utiliza el programa CAD, conocidas como NURBS.

En particular, una de las principales desventajas de los NURBS, y por ende del IGA, es la falta de refinamiento local, lo cual los hace computacionalmente costosos en aplicaciones que demandan mallas no uniformes. PHT-splines fue introducido por Deng et al. como un tipo de spline capaz de realizar refinamiento local por medio de una base polinomial que parametriza la geometría.

En esta tesis, utilizaremos PHT-splines para resolver dos tipos de problemas: Problemas de acústica modelados por la ecuación de Helmholtz, y problemas de mecánica de fractura en placas delgadas modelados por la teoría de Kirchhoff-Love.

Las soluciones de la ecuación de Helmholtz tiene dos características: oscilaciones globales asociadas al número de onda y gradientes locales causados por irregularidades geométricas. Los resultados muestran que después de utilizar un número suficiente de grados de libertad para aproximar las oscilaciones globales, el mallado adaptativo es capaz de capturar características locales de la solución. Estimadores de error residual y recuperativo fueron comparados, y además el rendimiento del refinamiento tipo p fue estudiado.

Para modelar problemas de estática y dinámica en placas delgadas con la teoría de Kirchhoff-Love con grietas, se utiliza una formulación extendida basada en la metodología Geometry Independent Field approximaTion (GIFT). El mallado adaptativo es controlado mediante un estimador de error recuperativo. Los principales resultados muestran que el mallado adaptativo es capaz de capturar características locales de la solución alrededor de la punta de la grieta, mejorando los resultados en los ejemplos de estática y dinámica estudiados.

En ambos casos, las simulaciones son realizadas dentro del contexto del recientemente introducido GIFT, donde PHT-splines son únicamente utilizados para aproximar la solución, mientras que el dominio geométrico es parametrizado con NURBS. Este enfoque se basa en la naturaleza adaptativa de los PHT-splines y evita la re-parametrización de la geometría NURBS durante el proceso de remallado.

Dedicada a Gastón, Ema y Mía. Gracias por su apoyo incondicional.

Acknowledgements

First, I would like to acknowledge my supervisor, Prof. Elena Atroshchenko for all the support, encouragement and help that she kindly brought during the last couple of years and in particular, during this thesis work. She always gave me good advice when there wasn't a clear path to follow in this project. Thank you for believing in me.

I would also like to express my sincere gratitude to Prof. Stéphane P. A. Bordas, who hosted me at the University of Luxembourg. I especially appreciate his guidance and suggestion regarding my work, particularly in the Kirchhoff-Love implementation. But, most importantly, I would like to thank him for being always willing to help me.

Besides, I want to give a sincere thanks to my friends at the MSc. group at the University of Chile: Patricio, Tomás, Philip K., Gabriel, Danilo, Andrés R.T., Cristián, Joaquín, Ignacio and especially to Sergio "Chachi" Cofré. We have shared cheerfulness and stressful moments over the last two years, and you all made this process a more enjoyable experience.

I want also express profound gratitude to my parents, who have always support me in all my decisions. I know how hard they've worked over their lives to give my brothers and me the best education possible, and I'm just trying to make their effort worth it.

And Finally, I want to thanks Ana Maria for his tremendous and unconditional support during all the years we have been together. It wouldn't be the same without your love, care, help, and support.

Contents

List of Tables

List of Figures

Chapter 1

Introduction

Nowadays, engineers perform designs using Computer-Aided Design (CAD) software and perform analyses by using Finite Element Method (FEM) commercial software. The typical situation in engineering practice is the one where designs are encapsulated in CAD systems, meshes are generated from CAD data, and FEM is performed over the meshes. This allows an entirely different geometric description for analysis, which is only approximate. In some instances, mesh generation can be done automatically, but in most circumstances, it can be done at best semi-automatically. There are still situations in major industries where drawings are made of CAD designs, and meshes are built from them. It is estimated that about 80% of overall analysis time is devoted to mesh generation in the automotive, aerospace, and shipbuilding industries [1].

1.1 Isogeometric Analysis and refinable splines

In order to overcome this gap between the design and engineering analysis, in 2005 Hughes et al. [1] proposed Isogeometric Analysis (IGA) as a method to use the original CAD geometry and the corresponding Non-Uniform Rational B-Spline (NURBS) functions to approximate solution in the FEM. The future implications of this merge are profound, since both the time and computational resources saved may lead to tremendous gains in the design work-flow. IGA has found many applications in different areas such as structural mechanics [2], shape optimization [3, 4, 5], fluid-structure interaction [6, 7, 8], shell analysis [9, 10], vibrations [11, 12, 13], fracture mechanics [14, 15, 16], hyper-elastic models [17, 18, 19] to name a few.

The main advantage of IGA over FEM is the fact that the splines basis functions outperform standard Lagrange polynomials basis functions in FEM in several aspects, such as higher continuity, and the exact representation of the geometry, leading to an increasing interest in the engineering and science community [20].

Despite its popularity, especially on the academia, IGA is still a relatively young method, and there still is a small number of tools available, especially in comparison with the Finite Element Method [21]. For example, the commercial software GiD recently included tools to handle model, pre- and post-processing, and visualization of results on NURBS based

geometries [22]. Lai et al. [23] proposed software framework for T-spline based isogeometric analysis (IGA), using Rhinoceros 3D (Rhino) to create the geometries and SIMULIA Abaqus (Abaqus) to perform the analysis through its user element subroutine.

In particular, one of the main drawbacks of NURBS basis functions, and therefore of IGA, is the lack of local refinement, which makes them computationally highly expensive in applications that demands a non-uniform refinement of the geometry.

In this context, Sederberg et al. [24, 25] introduced a generalization of NURBS called T-splines. T-splines have been successfully used in IGA. For example Bazilevs et. al. [26] proposed IGA with T-splines and applied it to solve 2D and 3D problems of fluid and structural interaction, Dörfel et. al. [27] studied the local h-refinement properties of T-splines applied on problems of stationary heat transfer and linear elasticity, and da Veiga et. al. [28] studied patch coupling using T-splines. T-splines has also been employed in Extended Isogeometric Analysis (XIGA) for fracture mechanics [29].

Furthermore, Polynomial splines over Hierarchical T-meshes (PHT-splines) were introduced by Deng et al. [30, 31] as a generalization of B-splines over hierarchical T-meshes, allowing local refinement and adaptability by means of a polynomial basis capable of parameterizing the geometry. PHT-splines have been used in IGA in elasticity problems [32, 33, 34], Kirchhoff-Love Thin Shell plates [35] and fracture mechanics [36] among others. PHT-splines were subsequently extended to rational polynomial splines, known as RPHT-splines [32] and have been successfully applied to model large deformation thin shell problems with multiple-patch coupling [37].

1.2 Geometry Independent Field approXimation: decoupling of the field and geometry

Following the work of Marussig et al. [38] in the context of Boundary Element Method (BEM), the idea of a Geometry-Independent Field approximaTion (GIFT) was proposed [20]. GIFT consists in allowing different spaces for the parameterization of the computational domain and the approximation of the solution field. In particular, it allows to preserve the exactness of the CAD geometry, while using a more suitable or flexible set of basis functions for the solution field. GIFT has been applied to problems of Poisson's equation and linear elasticity [20], yielding optimal convergence rates for pairs of geometry and field bases that do not pass the patch-test. Recently, Anitescu et al. [39] employed the GIFT idea in a high-order PHT-splines formulation for problems of 2 and 3D elasticity with adaptive refinement driven by a recovery-based error estimator, and Peng et al. [40] employed the GIFT formulation to study adaptive refinement on Reissner-Mindlin plate's based on a frequency-domain analysis. The main features of GIFT are:

1. Preserve exact CAD geometry provided in any form, including B-splines or NURBS, at any stage of the solution process.
2. Allow local refinement of the solution by choosing appropriate field approximations, as independently as possible of the geometrical parameterization of the domain.
3. Allow computational savings by not refining the geometry during the process of re-

fining the solution and by choosing simpler approaches for the solution, that is, using polynomial functions instead of rational functions.

In this work, a GIFT formulation will be employed, with a NURBS parameterization for the geometry together with PHT-splines basis functions to approximate the solution. This particular choice will allow us to preserve the exact geometry while exploiting computational savings by only refining the solution basis.

1.3 Error estimators and Adaptive refinement

A specific criterion needs to be defined to drive the adaptive refinement, usually an error estimator. As an *a posteriori* error estimator is used for evaluating the true error and guiding mesh refinement, it needs to be reliable at both local and global level. A posteriori error estimates aim at the estimation or approximation of the discretization error, i.e. at answering the question: "how well are we solving the problem?" In this work we are concerned with two types of error estimators: recovery-based [41, 42, 43] and residual-based [44, 45].

The residual type of error estimator was initially proposed by Babuška and Rheinboldt [46, 47, 48]. The error is computed by using the residual of the finite element solution as the approximate solution from the numerical method does not exactly satisfy the governing partial differential equations. Residual-based methods are further classified as explicit and implicit methods [49]. Explicit methods are based on estimating the norms of the interior and exterior residuals, corresponding to the equation inside the domain and the boundary conditions respectively, and based only on the obtained numerical solution. The main feature of implicit methods is a presence of additional parameters obtained from solving an auxiliary problem.

Recovery-based error estimates, first introduced by Zienkiewicz and Zhu on 1987 [41], are based on the construction of an enhanced solution u^* (or the gradients ∇u^*) by means of the original numerical solution u_h (or ∇u_h), and then estimates the norm of the error as

$$\|\mathrm{e}\| \approx \|\mathrm{e}^*\| = \|u_h - u^*\|_{L^2} \tag{1.1}$$

This error estimator has been improved by the same authors with the introduction of the Superconvergent Patch Recovery (SPR) [42, 43, 50]. Recovery based error estimators are more commonly used in finite elements, as they are relatively simple to implement, computationally inexpensive and usually provide reliable error estimates. The key ingredient of SPR methods are the locations of points where the solution is more accurate (superconvergent) under some regularity assumptions, and a method to fit the solution at those points with a higher-order function.

The theory involved in SPR was studied for the p-version FEM based on triangular meshes in [51], where a computer-based proof for determining the superconvergent points was provided. In the recent years, the theory of superconvergence was studied in the context of the isogeometric collocation method [52], where the superconvergent points for B-Splines have been derived. An SPR method was applied for PHT-splines in [39], where improved convergence rates for 2D and 3D elasticity problems with singularities have been observed. We

also refer to [53] for a detailed description of recovery procedures relevant to isogeometric analysis using Locally Refined (LR) B-Splines to drive local adaptivity.

Among other methods derived from SPR we mention XMLS (Extended moving least-squares recovery) [54, 55], which is a local recovery of the stresses in the context of XFEM which does not require the existence of super-convergent points. Another related procedure is XGR (extended global derivative recovery) [56], which is a global recovery of the stress in the context of XFEM. In this case, a new basis function capable of span the near-tip strain fields is introduced in the recovery solution.

1.4 Selected applications

Two branches of problems have been selected to test this GIFT formulation with NURBS and PHT-splines, time-harmonic acoustics and fracture mechanics on thin plates. Both of these problems present numerical challenges to domain-based methods, where the couple between exact parameterization and adaptive refinement can lead to improvement on the results.

1.4.1 Time-harmonic acoustics

Many physical phenomena such as seismic movements [57] or tsunamis [58], and applications such as ocean wave energy [59, 60, 61], sonar systems [62], radar systems, electromagnetic waves to ultrasonic transmission tomography [63], to name a few, can be characterized by means of the wave equation. In general, this equation can be expressed as:

$$\frac{\partial p}{\partial t} = c^2 \Delta p \tag{1.2}$$

where $p = p(\boldsymbol{x}, t)$ is the function describing the wave, Δ is the Laplace operator, c is the wave speed, $\boldsymbol{x}$ is a generic point in the physical space and t is the time variable. Function p can be interpreted as the energy carried by a particle of the media positioned at the point $\boldsymbol{x}$ in the time t. Helmholtz equation arises from the time-independent version of the wave equation. Assuming that p can be written as $p(\boldsymbol{x}, t) = u(\boldsymbol{x})\mathrm{e}^{-iwt}$, where w is the time frequency and i is the complex unity ($i = \sqrt{-1}$), the spatial part of the wave equation becomes:

$$\Delta u + k^2 u = 0 \tag{1.3}$$

where u is the sought spatial component of the wave and parameter $k \in \mathbb{C}$ is the wave number. The relationship between k and c is given by $k = \frac{w}{c}$. We also introduce λ as the wavelength, so the relationship between λ and k is given by $\lambda = \frac{2\pi}{k}$. With this definition we can interpret k as the number of wavelengths per 2π.

The first applications of finite elements analysis to acoustic problems date back to 1960s [64], and despite progress in numerical methods made during the subsequent years, accompanied by the rapid growth in computational capabilities, the main challenges of numerical acoustics are still not resolved. One of the main difficulties is related to the high-frequency regimes, characterized by large values of parameter k in eq.(1.3), or small values of the wavelength λ in comparison with the characteristic size of the system. In such cases, the overall

accuracy of the solution is affected not only by the discretization error, but also by the so-called pollution or numerical dispersion error [65, 66, 67], associated with a loss of stability of the Helmholtz operator at large values of k. The second major difficulty is related to solving the Helmholtz problem in an unbounded domain, which requires an efficient treatment of the Sommerfeld radiation condition at infinity. Commonly, an unbounded computational domain is truncated by an artificial surface, where the Sommerfeld condition is approximated, which introduces an additional error into the overall solution.

Pollution error in the higher-order FEM

Mathematically, the overall error for the Helmholtz equation is expressed in the following inequality for the relative difference in the H^1 semi-norm between the numerical solution u^h and the exact solution u [67]:

$$\frac{||u^h - u||_{H^1}}{||u||_{H^1}} < \underbrace{C_1 \left(\frac{kh}{2p}\right)^p}_{\text{approximation error}} + \underbrace{C_2 k \left(\frac{kh}{2p}\right)^{2p}}_{\text{pollution error}} \tag{1.4}$$

The first term in right hand side of the inequality (1.4) represents the approximation error and the second term corresponds to the pollution error, p is the degree of polynomial shape functions and h is the mesh size. The condition $\frac{kh}{p} < 1$ defines the so-called pre-asymptotic range, where the error in eq.(1.4) is governed by the second term, while the condition $\frac{k^2 h}{p} < 1$ defines the asymptotic range, where the error in eq.(1.4) is governed by the first term, i.e. the pollution error is negligibly small in comparison to the approximation error [49]. Since for large values of k, the condition $\frac{k^2 h}{p} < 1$ is difficult to achieve in practice, a large amount of research on error estimation for the Helmholtz problem has been done under assumption on kh or $\frac{kh}{p}$ only. For example, in [68] it is shown that if $\frac{kh}{p}$ is sufficiently small, the convergence rate is quasi-optimal if the polynomial order p is at least $O(\log k)$. In [69] it is shown that if for small h the value of k is big enough to have $kh \gg 1$, the pollution error can be eliminated if the polynomial order is chosen such that $p + \frac{1}{2} > kh + c(kh)^{1/3}$ where $c = 1$ is suggested.

As it can be seen from eq.(1.4) approximations of degree $p \geq 2$ are more efficient for reducing pollution error than linear basis functions in the standard FEM. However, for fixed p and increasing k, the pollution effect cannot be fully eliminated [70]. A significant amount of research has been done with the purpose of reducing the pollution error of the linear FEM, which can be extended to higher order approximations. Analytical approaches are commonly based on extracting the highly oscillatory frequency component and reformulating the problem in terms of a new, slowly-varying unknown amplitude, which can be seen as a general extension of the wave envelope method introduced in [71]. For example, in [72] a Galerkin finite element method with asymptotically derived basis functions is proposed; in [73] a procedure is proposed, in which first a priori determination of the phase of the scattered wave is done and then a variational formulation concerning the amplitude is solved. In [74] a phase reduction method is proposed. In this method, the solution is split into a phase function and an amplitude function. In this case, a low-cost approximation solution of the phase is obtained to use it to solve the amplitude problem with a slowly varying unknown envelope function.

Another approach consists in employing the Partition of Unity Finite Element Method

(PUFEM), introduced in [75] for FEM; it consists in to enrich the solution basis by including plane wave functions. This PUFEM has also been proposed for high order FEM in [76], and recently proposed for IGA in [77]. A similar approach was made in [78], where an Extended Isogeometric Boundary Element Method (XIBEM) was proposed.

Acoustic problems in exterior domains

The second major difficulty in numerical analysis of wave propagation relates to solving the boundary value problems for the Helmholtz equation in an exterior (unbounded) domain. The physical requirement that the wave cannot be reflected at infinity is mathematically represented by the so-called Sommerfeld radiation condition:

$$\lim_{r\to\infty} r^{\frac{\mathrm{d}-1}{2}} \left(\frac{\partial u}{\partial r} - iku \right) = 0, \tag{1.5}$$

where $r = |x|$, $\mathrm{d} = 2, 3$ is the dimension of the domain, $\dfrac{\partial u}{\partial r}$ is the radial derivative of the wave.

Domain-based methods, like FEM, are designed for bounded domains and therefore, the exterior domain is usually truncated by an artificial boundary Σ (typically, a circle in 2D and a ball in 3D) and the Sommerfeld condition (1.5) is transformed into a boundary condition on Σ. A family of such boundary conditions was developed by Bayliss, Gunzburger and Turkel in [79, 80] (often refereed as BGT). In this work we employ the so-called BGT2 condition, which is characterized by the presence of second-order tangential derivatives. A number of generalizations and extensions of the BGT conditions have been proposed, see for example, [81], [82] and [83], as well as [84] and [85] for a comprehensive review. The numerical solution, obtained after solving the resulting boundary value problem (BVP) in a bounded domain, will contain domain truncation error and numerical discretization error if compared to the exact solution of the original problem in the unbounded domain. In this work we limit our attention to studying the accuracy of GIFT-solutions for a given BVP in a bounded domain, and therefore compare the obtained numerical results with the corresponding analytical solutions, which include the truncation error.

1.4.2 Kirchhoff–Love thin plates and fracture mechanics

Plate elements have found their applications in broad areas of engineering analysis from structural slabs in houses and buildings to aircraft's wings. The most commonly used model to predict the behaviours of plates is derived from the Kirchhoff-Love theory [86] as it requires only three degree of freedoms (DOF) of displacement without including rotation unknowns. The fundamental assumption of this theory is that the transverse shear deformations are neglected. This means if a cross-section is normal to the mid plane of the plate before deformation, it remains normal to the mid plane after deformation. For this reason, the transverse shear stresses are neglected while the in-plane ones remain accountable. Therefore, Kirchhoff-Love theory is applicable for thin plates in which the aspect ratio between the length and thickness is large. It is worth noting that the Kirchhoff-Love theory results in a fourth-order problem which requires C^1-continuity of the basis function if a numerical approach is involved to solve for approximate solutions. While this requirement causes a challenging

issue for traditional finite element method with Lagrange basis function, such higher-order formulation can be handled efficiently by means of isogeometric analysis (IGA).

Regarding the fracture analysis, there has been a well-established body of work on the investigation of structures with cracks using numerical tools including the well-known extended finite element method (XFEM) [87]. The main idea of this method is that the approximation functions are enriched in both discontinuous fields across the crack faces and near tip asymptotic fields. Consequently, the mesh does not need to comply with the crack geometry, which simplifies the meshing procedure. A survey of the XFEM can be found in the work of Abdelaziz and Hamouine [88] while Mohammadi [89] explained the concept in more details. The same enrichment idea of the XFEM has been applied to several methods, such as meshless methods [90], extended isogeometric analysis (XIGA) [91, 14, 15], isogeometric boundary element [92], isogeometric-meshfree [93], and recently to XIGA based on T-splines [29] and PHT-splines [36]. Although all the previous formulations have been proved to be effective to tackle 2D and 3D fracture mechanics problems, there is not the same amount of literature regarding their applications in plates.

Application of the XFEM and its variations has already been done to different plate's theories. Dolbow et al. [94] initially proposed an XFEM formulation applied to Reissner-Mindlin (RM) plates, Baiz et al. [95] then employed a smoothed FEM and XFEM for plates using similar theory. And recently, Xing et al. [96] employed a new set of high-order crack tip enrichment functions applied to the MITC element in the context of RM plates. Concerning thin shell theory, Belytschko and Areias [97] proposed an XFEM formulation to thin-shell structures, Bayesteh and Mohammadi [98] studied the effect of crack tip enrichment functions in the analysis of shells, Rabczuk et al. [99, 100] proposed a mesh-free method for thin-shell, while Nguyen-Thanh et al. studied [101] a XIGA shell formulation based on the Kirchhoff-Love theory. In pure Kirchhoff-Love plate theory the only works available are the ones of Lasry et al. [102, 103], where an XFEM formulation is proposed.

1.5 Introduction to the present work

In the present work, the GIFT framework will be employed to pair NURBS geometries with a PHT-splines solution basis, to study adaptive refinement techniques applied to problems of acoustics and fracture mechanics on thin plates. In both types of problems, this choice will allow improving the numerical solution by employing local adaptive refinement while preserving the geometry exactness. The efficiency of the adaptive refinement is analyzed by comparing residual and recovery based error estimators, as well as different refinement strategies. For acoustic problems, we investigate the performance of the refinement in the presence of pollution error. For Thin plates, we evaluate fracture parameters (J-integral and Stress Intensity Factors) and compare them with reference solutions.

1.6 Objectives and Statement

The objectives and scope for the thesis work are presented as follows.

1.6.1 General Objective

Develop and implement a posteriori error estimator and adaptive refinement scheme to study the coupling of NURBS geometry and PHT-splines field basis applied to two kind of problems: wave propagation and fracture mechanics on thin plates.

1.6.2 Specific Objectives

- Develop a GIFT code for 2 and 3D Helmholtz equation problems.
- Develop a GIFT code for static and vibration problems of thin plates with cracks.
- Analyze and compare the Helmholtz results in terms of convergence plots for the L^2 error norm, H^1 error semi-norm and effectivity index.
- Analyze and compare the fracture mechanics results in terms of convergence plots for the H^2 error semi-norm and effectivity index. Calculate fracture parameters by means of the J-integral, and compute natural frequencies for dynamic problems.

1.6.3 Statement and Thesis Scope

This thesis work is intended to propose and validate an adaptive refinement scheme using the GIFT formulation with NURBS parameterizations of the geometry and PHT-splines on the field basis. This proposed work will only be tested on benchmark problems, and the performance results are properly presented in convergence plots, figures and tables.

Chapter 2

Methodology

In order to successfully fulfill the objectives of the present thesis work, the following steps are implemented:

2.1 Literature review

Over the last twenty years, a vast volume of literature related to both FEM and error estimator has been published. Moreover, since Hughes and its team proposed IGA, several ideas and techniques from FEM have been revisited to study the gains and drawbacks of its applications on IGA. Therefore, a literature review of the principal topics that cover this thesis must be performed, which should include: Isogeometric Analysis, PHT-Splines, error estimators and adaptive refinement, among other subjects.

2.2 PHT-Splines GIFT code

According to the literature review, and based on the open-source codes available online, a Matlab®routine capable of performing GIFT using PHT-Splines will be implemented. This implementation will be oriented to two kind of problems: wave propagation and fracture mechanics on thin plates. The numerical implementation will be based on the open-source package IGAPACK, available at `https://github.com/canitesc/IGAPack`. In particular, the fracture mechanics routines will be based on the ones available from the open-source code IGAFEM [104], available at `https://sourceforge.net/projects/cmcodes/`.

2.3 Adaptive refinement strategies

A specific criterion needs to be defined to drive the adaptivity, usually an error estimator. As an *a posteriori* error estimator is used for evaluating the true error and guiding mesh refinement, it needs to be reliable at both local and global level. Two types of error estimator will be implemented on this thesis: the residual-based error estimators and recovery-based error estimator (or error estimators using recovery techniques).

2.4 Applications on wave propagation problems

The first area of application of the proposed formulation will be the propagation of waves on 2D and 3D domains. It is well known that this kind of problem present challenges to any numerical domain method, such as the pollution error that occurs when solving the equation with a high wave-number k, or the correct treatment of boundary conditions when moving from unbounded domain to bounded domains. Hence, adaptive refinement will be studied in this kind of problems to how adaptive refinement can improve the solution.

2.5 Applications on fracture mechanics on thin plates

The second area of applications of the proposed formulation is fracture mechanics on thin plates. For this purpose, an XFEM formulation will be coupled with the proposed code in order to solve static and dynamic fracture mechanics problems.

Chapter 3

Theoretical background

The following chapter details the necessary background to achieve the objectives stated for this thesis work successfully. First, a quick review is given on the concepts of Isogeometric Analysis and NURBS. Then a definition of PHT-Splines is given. Following this, a revision of the GIFT formulation is given, then a quick summary of the error estimators and adaptive refinement is stated. Finally, a small review of the two main applications, namely the Helmholtz equation and Kirchhoff-Love thin plates is performed.

3.1 Isogeometric Analysis

Hughes and its co-workers introduced IGA [1] with the aim to bridge the gap between the computer-aided design (CAD) system and the analysis, or generally referred as computer-aided engineering (CAE) in the commercial sector. To achieve this seamless integration, they proposed to employ the same basis functions that are used to represent the geometry in CAD accurately as basis functions to approximate the unknown fields. CAD geometries are usually constructed using B-splines/NURBS curves, surfaces and volumes, so this means that both the physical model and the solution space are constructed by B-spline/NURBS functions, and a scheme similar to FEM is applied using B-Splines/NURBS as basis functions. The main idea of IGA is schematized in Figure 3.1. For a complete overview of work in the field of the IGA the interested reader is referred to [1, 104, 105]. The following section briefly covers the definitions of NURBS curves and surfaces.

3.1.1 Non Uniform Rational B-Spline (NURBS)

Let $\Xi = \{\xi_0, ..., \xi_{n+p+1}\}$ be a non-decreasing sequence of real numbers, i.e., $\xi_i < \xi_{i+1}$ with the sub-index $i = 0, ..., n+p+1$. The ξ_i are called knots and Ξ is called the knot vector, n is the number of basis functions which comprise the NURBS and p is the polynomial order of the NURBS. If knots are equally-spaced in the parametric space, they are said to be *uniform*. If they are unequally spaced, then they are *non-uniform*.

A p-th degree NURBS curve is defined by:

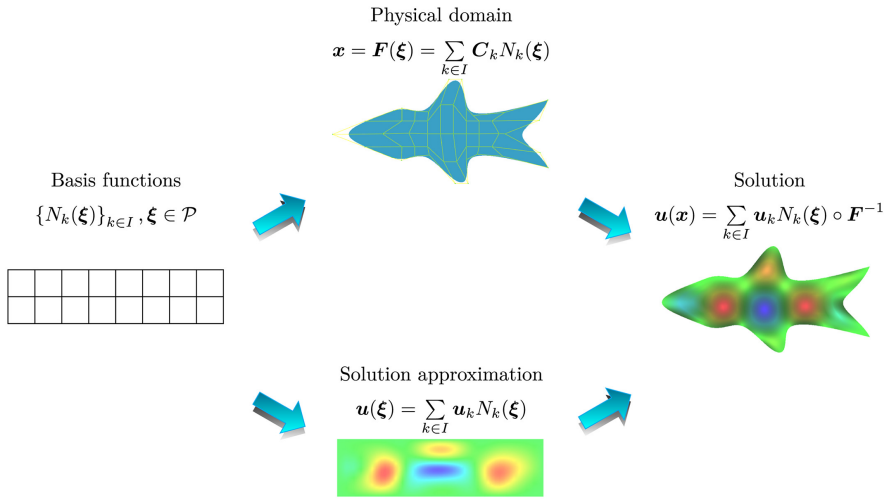

Figure 3.1: Main idea of the isogeometric analysis: the same shape functions are used for geometry parameterization and solution approximation [20].

$$C(\xi) = \sum_{i=1}^{n} R_{i,p}(\xi)\mathbf{P_i} \tag{3.1}$$

where $\mathbf{P_i}$ are the control points of the curve and $R_{i,p}$ are the Rational basis functions, defined by:

$$R_{i,p}(\xi) = \frac{N_{i,p}(\xi)w_i}{\sum_{j=0}^{n} N_{j,p}(\xi)w_j} \tag{3.2}$$

where w_i are the weights associated to each $R_{i,p}(\xi)$ and $N_{i,p}(\xi)$ are the p-th degree B-Spline basis functions, which are defined in a recursive way:

$$N_{i,0}(\xi) = \begin{cases} 1 & \text{if } \xi_i < \xi < \xi_{i+1} \\ 0 & \text{otherwise} \end{cases}$$

$$N_{i,p}(\xi) = \frac{\xi - \xi_i}{\xi_{i+1} - \xi_i} N_{i,p-1}(\xi) + \frac{\xi_{i+p+1} - \xi}{\xi_{i+p+1} - \xi_{i+1}} N_{i+1,p-1}(\xi) \tag{3.3}$$

Figure 3.2 shows an example of a 2D cubic NURBS curve with their control points. This curve is created with the following knot vector: $\Xi = \{0, 0, 0, 0, 0.4, 0.5, 0.6, 1, 1, 1, 1\}$. The control points are given on Table 3.1, and the respective basis functions are shown on Figure 3.3

Control Points P_i		
x	y	w
-4	-4	1
-4	0	$\sqrt{2}/2$
0	0	1
0	4	$\sqrt{2}/2$
4	4	1
4	0	1
2	-4	1

Table 3.1: NURBS curve: Control points and their respective weights

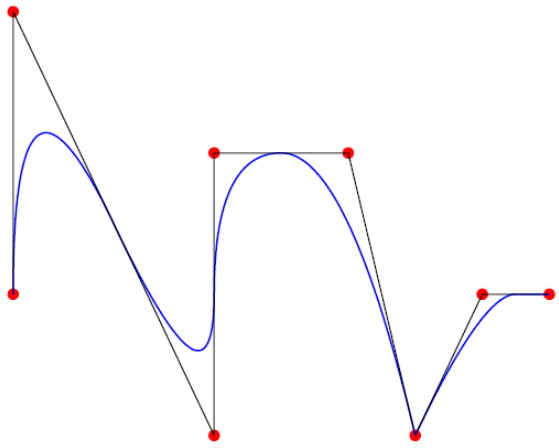

Figure 3.2: NURBS curve in 2D: curve (blue line) and control points (red dots)

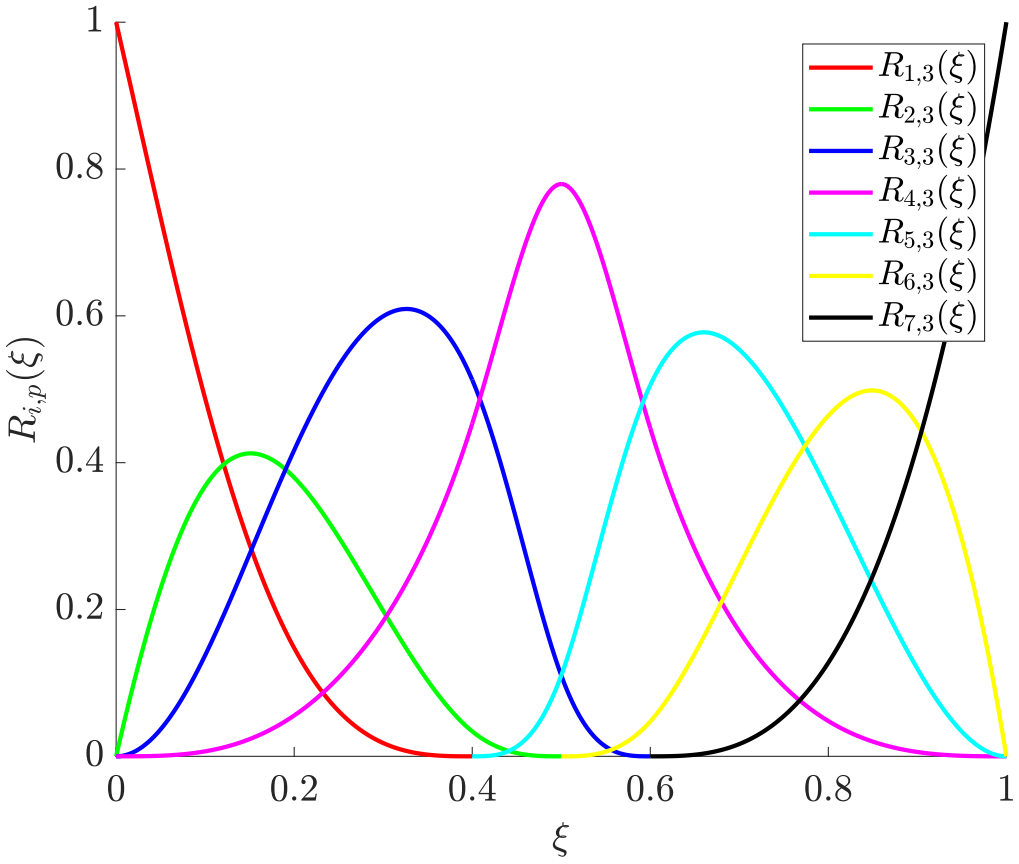

Figure 3.3: NURBS basis functions of Figure 3.2

Analogously, a NURBS surface of p-th degree in the ξ direction and q-th degree in the η direction is defined by:

$$\mathbf{S}(\xi,\eta) = \sum_{i=1}^{n}\sum_{j=1}^{m} R_{i,j}^{p,q}(\xi,\eta)\mathbf{P_{ij}} \tag{3.4}$$

where $\mathbf{P_{ij}}$ is a set of $n \times m$ bidirectional control net and $R_{i,j}^{p,q}$ is defined by:

$$R_{i,j}^{p,q}(\xi,\eta) = \frac{N_{i,p}(\xi)M_{j,q}(\eta)}{\sum_{\hat{i}}^{n}\sum_{\hat{j}}^{m} N_{\hat{i},p}(\xi)M_{\hat{j},q}w_{\hat{i},\hat{j}}} \tag{3.5}$$

where $N_{\hat{i},p}(\xi)$ and $M_{\hat{j},q}(\eta)$ are B-splines functions defined on knots sets Ξ_1 and Ξ_2, respectively.

Figure 3.4 shows an example of a 2D linear-quadratic NURBS surface. The polynomial order and knot vectors are given on Table 3.2, while the control points are shown on Table 3.3. Figure 3.5 shows the basis functions expanded over the aforementioned surface.

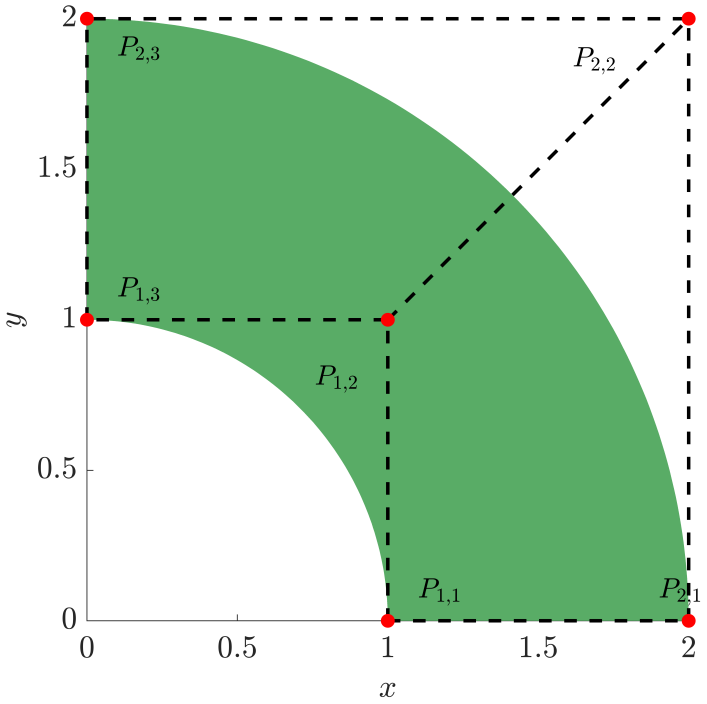

Figure 3.4: NURBS surface in 2D: curve (blue line) and control points (red dots)

Direction	Order	Knot Vector
ξ	$p = 1$	$\Xi = \{0, 0, 1, 1\}$.
η	$q = 2$	$\Xi = \{0, 0, 0, 1, 1, 1\}$

Table 3.2: NURBS surface: Polynomial orders and knot vectors for the surface shown in Figure 3.4

Control Points P_{ij}		
x	y	w
1	0	1
$\sqrt{2}/2$	$\sqrt{2}/2$	$\sqrt{2}/2$
0	1	1
2	0	1
$\sqrt{2}$	$\sqrt{2}$	$\sqrt{2}/2$
0	2	1

Table 3.3: NURBS surface: Control points and their respective weights for the surface shown in Figure 3.4

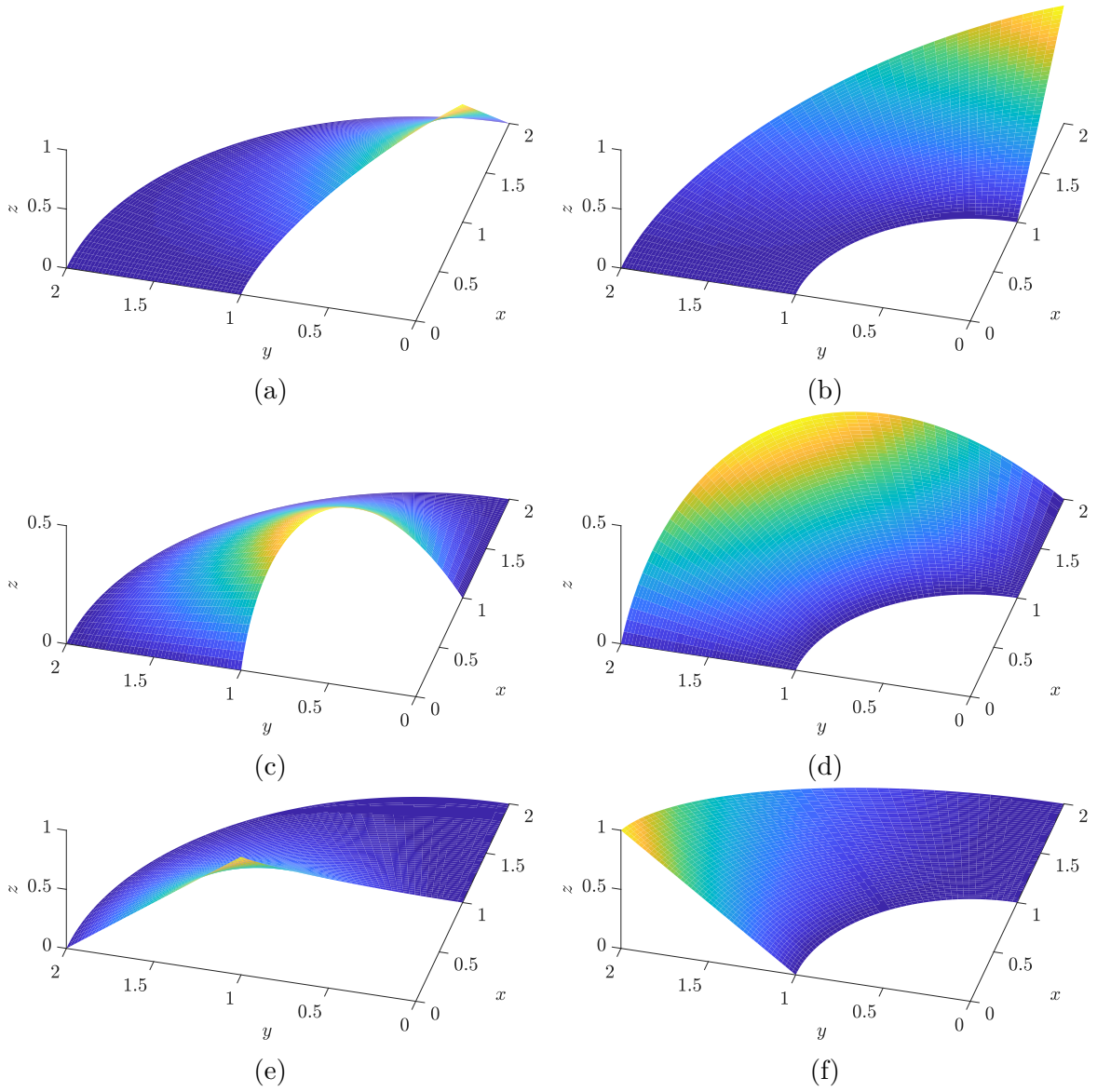

Figure 3.5: NURBS basis functions of the surface on Figure 3.3. Each basis functions is plotted over the geometrical space

The B-spline basis functions have the following properties:

- Linear independence.
- Partition of unity.
- Compact support for each $N_{i,p}$in the interval $[u_i, u_{i+p+1}]$.
- Non-negative basis functions.

Since NURBS are transformations of the B-spline basis functions they inherit their main properties and obtain more. Some of them include:

- Partition of unity.
- Continuity and support of B-spline.
- Affine transformations in a physical space are achieved by applying them to the control points. This means NURBS have the property of affine covariance.
- If the weights of all control points are equal, NURBS become B-splines.

3.2 Polynomials Splines Over Hierarchical T-meshes

Polynomial Splines over hierarchical T-meshes (PHT-Splines) where introduced by Deng et al. [30, 31] as a generalization of B-splines over hierarchical T-meshes, allowing local refinement and adaptability by means of a polynomial basis capable of parameterize the geometry. The following section briefly covers the formulation of PHT-splines.

3.2.1 T-meshes

Given a rectangular domain, a T-mesh is a mesh based on rectangular grids that allow T-junctions [24]. In T-meshes, the end points of each grid line must lie on two other grid lines, and each cell or facet in the grid is formed by a quadrilateral. A vertex of the T-mesh is assigned to each grid point. If a vertex is inside the domain, it's called an interior vertex, otherwise it's called a boundary vertex. The interior vertices have two types: crossing vertices and T-junctions. A T-junctions terminates a row or column of vertices and edges before the boundary of the T-mesh is reached. An edge of the T-mesh is defined by the line segment connecting two adjacent vertices on a grid line.

3.2.2 Hierarchical T-meshes

A hierarchical T-mesh can be considered as a special form of T-mesh, which has a natural level structure. Hierarchical T-mesh is initiated from a tensor product mesh which is assumed to be a level-0. If a level-k mesh is given, then the level-$(k+1)$ mesh is obtained by subdividing some of the cells in level-k. Each cell is subdivided into four sub-cells by connecting the middle points of the opposite edges in the cell. Figure 3.6 exemplifies a 2D hierarchical T-mesh.

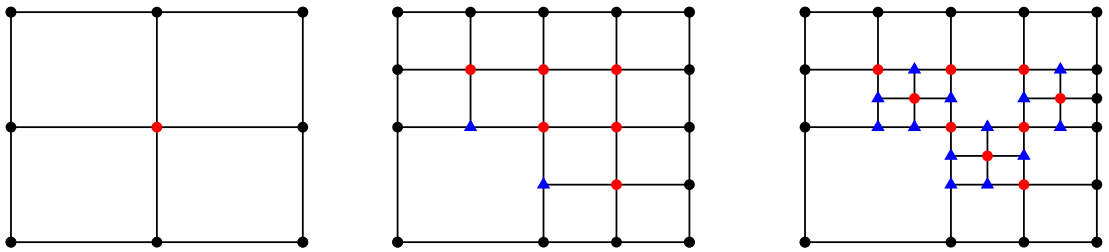

(a) Initial Regular Mesh (b) First adaptive mesh (c) Second adaptive mesh

Figure 3.6: Initial T-Mesh and two levels refinement. Black dots denote the boundary vertexes, red dots denote the crossing vertexes, while blue triangles denote T-junctions

3.2.3 PHT-Splines Space

Let $\mathscr{T}$ be the T-mesh, $\mathscr{H}$ be the cells in $\mathscr{T}$, $\Omega \subset \mathbb{R}^2$ be the region occupied by $\mathscr{T}$. The spline space over the given T-mesh $\mathscr{T}$ is defined as:

$$\mathscr{L}(p,q,\alpha,\beta,\mathscr{T}) = \left\{ s(x,y) \in C^{\alpha,\beta}(\Omega) \,|s(x,y)|_{\phi} \in \mathbb{P}_{pq}(\forall \phi \in \mathscr{H}) \right\} \tag{3.6}$$

Where the space $\mathbb{P}_{pq}$ consists of all the bi-degree (p,q) polynomials and the space $C^{\alpha,\beta}$ corresponds of all the continuously bi-variate functions up to order α in the x-direction and order β in the y-direction. The dimension formula of the spline space $\mathscr{L}(p,q,\alpha,\beta,\mathscr{T})$, when $p \geq 2\alpha+1$ and $q \geq 2\beta+1$, has already been proved in previous studies. For a C^1-continuous cubic spline, where every interior knots is of multiplicity two, the evaluation of the dimension formula is reduced to the following form:

$$\dim \mathscr{L}(3,3,1,1,\mathscr{T}) = 4(V^b + V^+) \tag{3.7}$$

Where V^b and V^+ are boundary vertices and interior crossing vertices, respectively. (3.7) shows that how many basis functions corresponding to the number of boundary and crossing vertices need to be constructed. It's also implied that each boundary vertex or each crossing vertex is connected by four basis functions.

3.2.4 PHT-Splines Surfaces

Let $\mathscr{T}$ be a hierarchical T-mesh, $b_i(\xi,\eta)$, $i = 1,2,...,n$ be a set of Bézier splines (B-splines), ξ and η two parametric coordinates defined on the space $[0,1 \times 0,1]$, and $\mathbf{P}_i$ be the control points. Then, the polynomial spline surface over $\mathscr{T}$ at level 0 is defined by:

$$\mathbf{S}(\xi,\eta) = \sum_{i=1}^{n} b_i(\xi,\eta)\mathbf{P}_i \tag{3.8}$$

A spline basis function can be represented locally as a linear combination of Bernstein polynomials. In particular, each B-Spline $b_i(\xi,\eta)$ is defined as

$$b_i(\xi,\eta) = \sum_{j=1}^{p+1}\sum_{k=1}^{p+1} C_{jk}^{i}\hat{B}_{j,k}(\xi,\eta) \tag{3.9}$$

where $\hat{B}_{j,k}(\xi,\eta) = B_j(\xi)B_k(\eta)$ is a tensor product of Bernstein polynomials defined on the reference interval $[-1,1]$:

$$B_j(\xi) = \frac{1}{2^p}\binom{p}{j-1}(1-\xi)^{p-j+1}(1+\xi)^{j-1} \tag{3.10}$$

The procedure to compute Bézier coefficients C_{jk}^{i} based on a particular NURBS curve is detailed in [106]. Then, based on a B-spline surface written over a initial regular T-mesh (level-k), we briefly explains how to compute the new coefficients given a refinement on a level-$k+1$:

1. Construct a *Bézier* representation of the basis functions. This is done using Bernstein polynomials and *Bézier* coefficients (other authors refers them as *Bézier* ordinates).
2. Once a level refinement is applied, the shape functions whose support was lying on refined element must be modified. Given the Bézier representation of the basis function, the process consist in to truncate by zeroing out Bézier coefficients. This process is also explained in introductory paper to PHT-splines [31] and also in the works of Garau and Vásquez [107].
3. After the truncation of coefficients comes the insertion of new basis functions. For each new basis function, this involves the computation of the corresponding Bézier ordinates and the assignment of a new global basis index. We note that the new basis' functions are standard (non-truncated) B-splines, which can be computed based on local knot-vector information. In the case of a removed T-junction, the local knot-vectors need to be computed based on the neighbor connectivity of the elements which is stored in the quad-tree structure Finally, the new basis indices corresponding to the new basis functions are determined.

It is worth noticing that this thesis is based on the open-source package IGAPACK (`https://github.com/canitesc/IGAPack`), which already have implementations for the aforementioned routines.

3.3 Geometry Independent Field approximaTion (GIFT)

The Geometry Independent Field approximaTion (GIFT) [20] is a generalization of the concept of IsoGeometric Analysis (IGA), that allows the coexistence of different spaces for the parametrization of the computational domain and the approximation of the field of the solution. This means that GIFT preserves the exact geometry of the CAD that uses for example, NURBS functions; but, in the approximation space of the solution, it allows the use of more flexible and/or suitable functions for the analysis, such as: T-Splines, LR-Splines, Hierarchical B-Splines and PHT-Splines. In particular, GIFT allows a local refinement adapted without the need to re-parameterize the geometry of the domain given by the CAD model.

The main idea of GIFT is to preserve the original geometry of the CAD while adapting the base of the solution with flexibility and thus improving the approximation of the solution field. The main features of GIFT are:

1. Preserve exact CAD geometry provided in any form, including B-splines or NURBS, at any stage of the solution process.
2. Allow local refinement of the solution by choosing appropriate field approximations, as independently as possible of the geometrical parameterization of the domain.
3. Allow computational savings by not refining the geometry during the process of refining the solution and by choosing simpler approaches for the solution, that is, using polynomial functions instead of rational functions.

In Figure 3.7 the main idea of the GIFT is schematized: Two different sets of basis functions are defined, namely, $N_\alpha(\boldsymbol{\xi})$ for the physical space, and $M_\beta(\boldsymbol{\xi})$ for the field space. Then, the solution is constructed as a composition between the physical space and the field space.

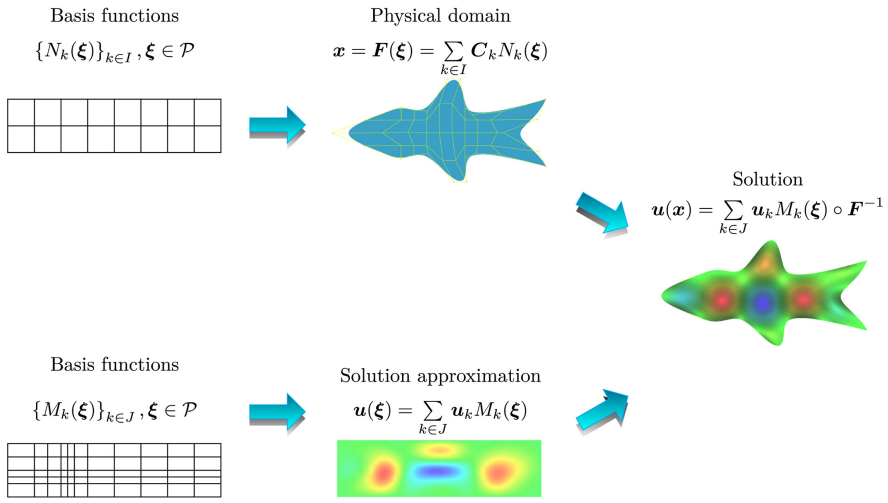

Figure 3.7: Main Idea of the GIFT: different basis functions are used to parameterize the geometry of the object and the approximation of the solution [20].

3.3.1 Formulation of GIFT

First, let's consider a boundary-value problem (BVP) defined on a domain Ω. The domain Ω is parameterized on a parametric domain Ξ by a mapping function $\mathbf{F}$:

$$\boldsymbol{x} := \mathbf{F}(\boldsymbol{\xi}) = \sum_{i=1}^{n} \mathbf{C}_i N_i(\boldsymbol{\xi}) \tag{3.11}$$

where $\boldsymbol{x}$ are the coordinates in the physical space, $\mathbf{C}_i$ are the control points, $N_i(\boldsymbol{\xi})$ are the NURBS basis functions and n is the number of NURBS functions.

The unknown field u^h of the boundary value problem can be approximated with a different finite dimensional space, whereas for this thesis we choose the PHT-splines basis $M_i(\boldsymbol{\xi})$. The approximation can be defined with the help of the inverse of the mapping $\mathbf{F}$ as:

$$u^h(\boldsymbol{x}) = \sum_{i}^{m} U_i (M_i \circ \mathbf{F}^{-1})(\boldsymbol{x}) \tag{3.12}$$

where U_i are the control variables corresponding to basis functions $M_i(\boldsymbol{\xi})$ and m is the number of PHT-splines basis functions. If the weak form of the boundary value problem is given by:

$$a(u, v) = l(v), \tag{3.13}$$

then, using the representation (3.12) together with $v = M_j(\boldsymbol{\xi})$, the weak form (3.13) can be transformed into the following linear system of equations:

$$\mathbf{K}\mathbf{u} = \mathbf{f} \tag{3.14}$$

where $\mathbf{K}$ correspond to the Global Stiffness Matrix, $\mathbf{U}$ is the vector of all unknown control variables U_k and $\mathbf{f}$ is the vector of Global Nodal Forces; which are given by:

$$\mathbf{K}_{ij} = a(M_i \circ \mathbf{F}^{-1}, M_j \circ \mathbf{F}^{-1}) \tag{3.15}$$

$$\mathbf{f}_i = l(M_i \circ \mathbf{F}^{-1}). \tag{3.16}$$

More details about the weak form and the specific terms of equations (3.15) and (3.16) for the Helmholtz equation and Kirchhoff-Love equation will be given in their respective sections.

3.4 Error estimators and Adaptive refinement

Based on the local refinement of PHT-splines, the main goal of this thesis is to study how an error driven adaptive refinement can lead to better results. In this sense, the usual loop process is schematized as [108, 109, 110, 111]:

Solve → *Estimate* → *Mark* → *Refine*

In this work, both recovery and residual-based error estimator will be studied. In the following section, a description of the error estimators and marking algorithm employed in this thesis is given.

3.4.1 Residual-based error estimator

The residual type of error estimator was initially proposed by Babuška and Rheinboldt [46, 47, 48]. The error is computed by using the residual of the finite element solution as the approximate solution from the numerical method does not exactly satisfy the governing partial differential equations.

The residual-based error estimator consists in approximating the numerical error of the solution using the residual of equation that describes the BVP, as a quantity of interest. Consider a cell K from the numerical discretization of the field. The local residual error indicator e_K on a cell K in the parametric domain, is defined as [45]:

$$\mathrm{e}_K = h_K \left\| r \right\|_{L^2(\Omega_K)} \tag{3.17}$$

where Ω_K is the element in the physical domain, corresponding to element K in the parametric domain, h_K is the diameter of Ω_K and r is known as the residual of equation. For instance, if we consider the Helmholtz equation (eq. (1.3)), the residual can be defined as:

$$r = \Delta u^h + k^2 u^h \tag{3.18}$$

Then e_K can be interpreted as the error of the numerical solution of the weak form measured in a L^2 norm by means of the original equation of the strong form.

In the same way, the global error in the solution can be defined as:

$$\left\| \mathrm{e}^h \right\| = \sum_K \mathrm{e}_K \tag{3.19}$$

Some works, e.g. [112], include boundary error terms in the residual-based error indicator as:

$$\mathrm{e}_{BC_k} = \left[h_K^2 \left\| r \right\|^2_{L^2(\Omega_K)} + h_k \left\| R_k^h \right\|^2_{L^2(\mathrm{d}\Omega_K \cap \mathrm{d}\Omega)} \right]^{1/2} \tag{3.20}$$

where r is defined as in equation (3.18), $\mathrm{d}\Omega_K$ and $\mathrm{d}\Omega$ are the boundaries of Ω_K and Ω, respectively, R_k^h is defined as the boundary residual, and h_k is the length/area of a boundary element.

3.4.2 Recovery-based error estimator

The recovery-based error estimator for PHT-Splines using super-convergent patch recovery has been proposed by Anitescu et al. in [39] in the context of linear elasticity. What follows is the adaption of that procedure to the Helmholtz equation. The recovery-based error estimator for the Kirchhoff-Love equation is given in Section 3.6.7.

The main idea behind recovery-based error estimators is to create a more accurate approximation of the gradient of the solution utilizing for example, the super-convergent patch recovery procedure. Then, the recovered gradient solution is considered as a substitute for the exact gradient of the solution, which can be employed to compute error norms with high precision.

The original procedure, proposed by Zienkiewicz and Zhu [41], consist in computing a more accurate solution at the carefully chosen points that are capable of generating a better approximation of the desired quantity. At those points a higher-order polynomial fit will be performed in order to obtain the recovery solution. Then, the error estimator is computed in the normalized H^1 semi-norm as:

$$\frac{\|\mathrm{e}_{rec}\|_{H^1}}{\|G\left[\nabla u_h\right]\|_{H^1}} = \frac{\left(\int_\Omega \left(G\left[\nabla u_h\right] - \nabla u_h\right)^T \left(G\left[\nabla u_h\right] - \nabla u_h\right) \mathrm{d}\Omega\right)^{1/2}}{\left(\int_\Omega \left(G\left[\nabla u_h\right]\right)^T \left(G\left[\nabla u_h\right]\right) \mathrm{d}\Omega\right)^{1/2}} \tag{3.21}$$

where ∇u_h is the gradient of the numerical solution u_h and $G\left[\nabla u_h\right]$ is the recovery gradient computed using the numerical gradient ∇u_h. In the same way, the error indicator on each cell K can be computed as:

$$\mathrm{e}_{rec_K} = \left(\int_\Omega \left(G\left[\nabla u_h\right] - \nabla u_h\right)^T \left(G\left[\nabla u_h\right] - \nabla u_h\right) \mathrm{d}\Omega\right)^{1/2} \tag{3.22}$$

The carefully chosen points are the super-convergent points, which are computed in the same way as in [39]. Table 3.4 shows the super-convergent points on an interval $[-1, 1]$ for several values of spline degree p and continuity orders α.

p	α	Super-convergent points
3	1	± 1, 0
4	1	$\pm\sqrt{(3/7) \pm (2/7)\sqrt{6/5}}$
5	2	± 1, $\pm\sqrt{1/3}$, 0
6	2	± 0.790208564, ± 0.2800702925
7	3	± 1, ± 0.5294113738, 0

Table 3.4: Super-convergent points for splines of degree p and continuity C^α on interval $[-1, 1]$

Next, we briefly outline the procedure of computation of the recovery gradient solution $G\left[\nabla u_h\right]$. The reader is referred to [39] for details regarding the implementation of this process

with PHT-Splines.

Let be Ω be the domain and Ω_k, $k = 1, ..., n$ a set of n non-overlapping patches such that together they form Ω: $\cup_{k=1}^{n} \Omega_k = \Omega$. Let $\boldsymbol{x}_{i,k}^*$ $(i = 1, ...N_k)$ be a set of N_k super-convergent points defined over the patch Ω_k. Let also $\phi_{i,k}^*$ be the set of basis functions employed for the recovery solution. In this case we employ B-splines functions of degree $p^* \geq p$ and continuity $\alpha^* \geq \alpha$. The $G\left[\nabla u_h\right]$ is constructed as:

$$G\left[\nabla u_h\right](\boldsymbol{x}) = \sum \phi_{i,k}^*(\boldsymbol{x}) \boldsymbol{C}_{i,k}^* \tag{3.23}$$

where $\boldsymbol{C}_{i,k}^*$ are the new DOF associated with the recovery gradient solution. We require equation (3.23) to fulfill the condition:

$$G\left[\nabla u_h\right](\boldsymbol{x}_{i,k}^*) = \nabla u_h(\boldsymbol{x}_{i,k}^*) \tag{3.24}$$

Equation (3.24) can be rewritten as the following linear system:

$$\boldsymbol{A}^k \boldsymbol{C}_k^* = \boldsymbol{b}^{\boldsymbol{k}} \tag{3.25}$$

where

$$\boldsymbol{A}_{ij}^k = \phi_{j,k}^*(\boldsymbol{x}_{i,k}^*) \tag{3.26}$$

$$\boldsymbol{b}_i^{\boldsymbol{k}} = \left[\frac{\partial u_h(\boldsymbol{x}_{i,k}^*)}{\partial x}, \frac{\partial u_h(\boldsymbol{x}_{i,k}^*)}{\partial y}\right] \tag{3.27}$$

Finally, the recovery solution can be computed by solving equation (3.25).

Lastly, we say that the recovery-based error estimator is asymptotically exact if the ratio between the error estimator and the error itself tends to 1 as the mesh size h tends to 0, ie:

$$\theta(\nabla u_h, \Omega) := \frac{\left\|\mathrm{e}_{rec}\right\|_{H^1}}{\left\|u - u_h\right\|_{H^1}} \rightarrow 1 \ \ as \ h \rightarrow 0 \tag{3.28}$$

where $\theta(\nabla u_h, \Omega)$ is known as the effectivity index of the error estimator.

3.4.3 Marking strategies

It is important to consider for the adaptive refinement process not just the accuracy and robustness of the error estimator itself, but also the choice of the marking algorithm, that is, the algorithm that decides with elements should be refined on each step. In general, there is a trade-off between the number of refinement steps required to reach a certain (estimated) accuracy and the number of elements in the final mesh: refining in small increments results

in “optimal” meshes that have as few as possible elements while refining more elements at each refinement step results in fewer overall refinement steps but less optimal meshes. This is particularly true in case of problems in singularities, as for coarse meshes the presence of a singularity results in significant errors even some distance away in the domain (the so-called "pollution errors"); however these errors become less significant as the area around the singularity is refined [39].

Marking strategy for the residual-based error estimator

For the residual-based error estimator, after e_K is calculated for each element, all elements are arranged in a descending error order and the first 50% of elements are marked for refinement. After that, the mean error estimator of the remaining elements is computed and any element whose error is bigger than the mean is also refined. This is done in order to ensure smoothness of the results across the domain and ensure a relatively well-graded mesh. This strategy is also applied in [20].

Marking strategy for the recovery-based error estimator

After the recovery-based error estimator is calculated, the refinement is guided using "Dörfler marking" strategy [113]. The strategy consists in sorting the elements according to their error contribution and then refining all elements where the error is bigger than a certain percentage α of the error estimator.

3.5 Helmholtz equation

3.5.1 Boundary-value problem (BVP)

In what follows we consider domain $\Omega \in \mathbb{R}^{\mathrm{d}}(\mathrm{d} = 2, 3)$ (interior or exterior) with boundary Γ, such that $\Gamma = \overline{\Gamma_D \cup \Gamma_N \cup \Gamma_R}$ and $\Gamma_D \cap \Gamma_N = \Gamma_D \cap \Gamma_R = \Gamma_R \cap \Gamma_N = \varnothing$. We seek the acoustic pressure u that satisfies the Helmholtz equation:

$$\Delta u + k^2 u = 0 \quad \text{in} \quad \Omega \tag{3.29}$$

where Δu is the Laplace operator, k is the wave number. In the most general case, three types of boundary conditions are possible:

$$\begin{array}{lrcll} \text{Dirichlet:} & u & = & g & \text{on} \quad \Gamma_D \\ \text{Neumann:} & \dfrac{\partial u}{\partial n} & = & ikh & \text{on} \quad \Gamma_N \\ \text{Robin:} & \dfrac{\partial u}{\partial n} + \alpha u & = & f & \text{on} \quad \Gamma_R \end{array} \tag{3.30}$$

where α is the given constant, $i^2 = -1$, n is the unit normal vector on Γ, pointing outward to Ω and functions g, h and f are prescribed on the corresponding parts of Γ.

In the case of an exterior domain, the solution u usually represents the acoustic field, produced by incident wave u^{inc}, scattered by domain $D = \mathbb{R}^{\mathrm{d}} \setminus \Omega$. In this case functions g, h

and f in eq.(3.30) are given by

$$g = -u^{\text{inc}}, \qquad ikh = -\frac{\partial u^{\text{inc}}}{\partial n}, \qquad f = -\frac{\partial u^{\text{inc}}}{\partial n} - \alpha u^{\text{inc}} \tag{3.31}$$

Additionally, u has to satisfy the Sommerfeld radiation condition at infinity, given by eq.(1.5). However, in domain-based numerical analysis, the exterior domain is usually truncated by an artificial boundary Σ, and the Sommerfeld condition is replaced by the absorbing boundary condition (ABC):

$$\frac{\partial u}{\partial n} + \mathcal{B}u = 0 \quad \text{on} \quad \Sigma, \tag{3.32}$$

where linear operator $\mathcal{B}$ is known as the Dirichlet-to-Neumann map and n is a unit outward normal vector. In the numerical examples, presented in this thesis, we consider the so-called second order Bayliss-Turkel ABC (BGT2), given by

$$\mathcal{B}u = \left(-ik + \frac{\kappa}{2} - \frac{\kappa^2}{8\left(\kappa - ik\right)}\right) u - \frac{1}{2\left(\kappa - ik\right)} \frac{\partial^2 u}{\partial s^2} \tag{3.33}$$

If in equation (3.33) domain Σ is a circle/ball of radius R, then $\dfrac{\partial u}{\partial n} = \dfrac{\partial u}{\partial r}$, the curvature $\kappa = 1/R$ and tangential derivative $\dfrac{\partial^2 u}{\partial s^2} = \dfrac{1}{R^2}\dfrac{\partial^2 u}{\partial \theta^2}$ in polar coordinates (r, θ) centered at the center of the circle.

3.5.2 Weak Form

Multiplying eq. (3.29) by a test function v, integrating over Ω and applying the boundary conditions with eq. (3.30), the weak form is obtained, which corresponds to finding solution $u \in H^1(\Omega)$ such that

$$a(u, v) = l(v), \qquad \forall v \in V \tag{3.34}$$

where $a(u, v)$ and $l(v)$ are:

$$a(u, v) = \int_\Omega \nabla u \nabla v \mathrm{d}\Omega - k^2 \int_\Omega uv \mathrm{d}\Omega + \alpha \int_{\Gamma_R} uv \mathrm{d}\Gamma + \int_\Sigma \mathcal{B}uv \mathrm{d}\Gamma \tag{3.35}$$

$$l(v) = ik \int_{\Gamma_N} hv \mathrm{d}\Gamma + \int_{\Gamma_R} fv \mathrm{d}\Gamma \tag{3.36}$$

In the weak formulation the test V is the space of all the functions $v \in H^1(\Omega)$ such that v vanishes on Γ_D.

Following the procedure described in Section 3.3.1, the discretization of the weak form (3.35), (3.36) with GIFT leads to the following coefficients for the linear system of equations (eq.(3.14)):

$$\mathbf{K}_{ij} = \int_{\Omega} \nabla \left(M_i \circ \mathbf{F}^{-1}\right) \nabla \left(M_j \circ \mathbf{F}^{-1}\right) \mathrm{d}\Omega - k^2 \int_{\Omega} \left(M_i \circ \mathbf{F}^{-1}\right) \left(M_j \circ \mathbf{F}^{-1}\right) \mathrm{d}\Omega \\ + \alpha \int_{\Gamma_R} \left(M_i \circ \mathbf{F}^{-1}\right) \left(M_j \circ \mathbf{F}^{-1}\right) \mathrm{d}\Gamma + \int_{\Sigma} \mathcal{B} \left(M_i \circ \mathbf{F}^{-1}\right) \left(M_j \circ \mathbf{F}^{-1}\right) \mathrm{d}\Gamma \tag{3.37}$$

$$\mathbf{f}_j = ik \int_{\Gamma_N} h \left(M_j \circ \mathbf{F}^{-1}\right) \mathrm{d}\Gamma + \int_{\Gamma_R} f \left(M_j \circ \mathbf{F}^{-1}\right) \mathrm{d}\Gamma \tag{3.38}$$

3.5.3 A posteriori error-estimates for the Helmholtz equation

In this work, both a residual-based and recovery-based error indicators are employed for estimating the error approximation of the numerical solution. Following the theory introduced in Section 3.4, we proceed to present the error estimator employed.

Residual-based error estimates for the Helmholtz equation

Section 3.4 already outlined the process to derive a residual-based error estimator for the Helmholtz equation. Here we recall the main results from that section.

The residual-based error estimator is given by

$$\mathrm{e}_K = h_K \left\| r \right\|_{L^2(\Omega_K)} \tag{3.39}$$

and the residual-based error estimator with boundary terms is given by

$$\mathrm{e}_{BC_k} = \left[h_K^2 \left\| r \right\|_{L^2(\Omega_K)}^2 + h_k \left\| R_k^h \right\|_{L^2(\mathrm{d}\Omega_K \cap \mathrm{d}\Omega)}^2 \right]^{1/2} \tag{3.40}$$

where Ω_K is the element in the physical domain, corresponding to element K in the parametric domain, h_K is the diameter of Ω_K and r is known as the residual of equation, in this case, defined as

$$r = \Delta u^h + k^2 u^h \tag{3.41}$$

while R_k^h is the boundary error, defined as

$$R_k^h = \begin{cases} 0 & \text{on} \quad \Gamma_D \\ \dfrac{\partial u}{\partial n} - ikh & \text{on} \quad \Gamma_N \\ \dfrac{\partial u}{\partial n} + \alpha u - f & \text{on} \quad \Gamma_R \end{cases} \tag{3.42}$$

and h_k is the length/area of a boundary element. In the numerical examples throughout this thesis, we used the residual error estimator defined by equation (3.39), (3.41), since the

preliminary simulations showed that the residual defined by eq.(3.40), (3.42) over-estimated the error in the boundary conditions of Robin type and as a consequence, lead adaptive refinement towards the boundary instead of the areas with high gradients.

Recovery-based error estimates for the Helmholtz equation

The recovery-based error estimates for the Helmholtz equation was already derived on Section 3.4.

3.6 Kirchhoff-Love plate theory and fracture mechanics

Let $\Omega \subset \mathbb{R}^2$ be an open-bounded region with boundary Γ. We consider a plate occupying a domain $V = \Omega \times \left[\frac{-h}{2}, \frac{h}{2}\right]$, where h is the thickness. It is assumed that the material plate is homogeneous and isotropic, with a Young's Modulus E and Poisson's ratio ν.

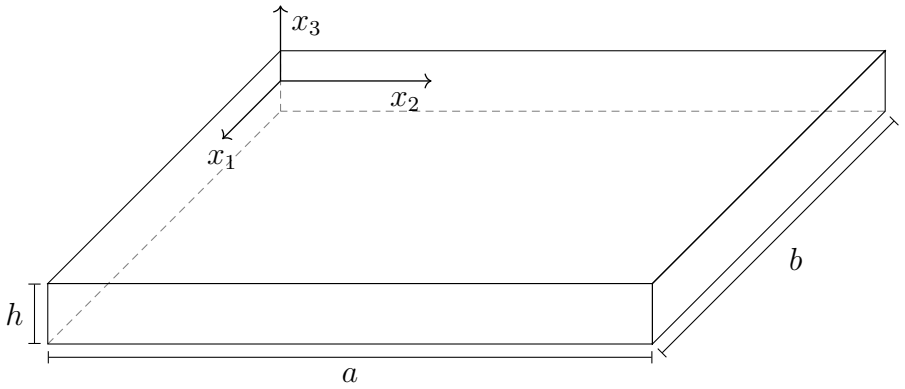

Figure 3.8: Plate geometry and reference system

The displacement $\mathbf{u} = \{u_1, u_2, u_3\}$ under the Kirchhoff-Love theory can be written as

$$\mathbf{u}(x_1, x_2, x_3) = \begin{cases} u_1(x_1, x_2, x_3) &= -x_3 \partial_1 u(x_1, x_2) \\ u_2(x_1, x_2, x_3) &= -x_3 \partial_2 u(x_1, x_2) \\ u_3(x_1, x_2, x_3) &= u(x_1, x_2) \end{cases} \tag{3.43}$$

where the notation $\partial_\alpha(\cdot)$ represents the partial derivative with respect to x_α. In the Kirchhoff-Love model, the kinematic actions are such that the normal vectors to the undeformed reference surface remain orthogonal to the deformed surface and doesn't change in length. Thus, the transverse shear strains are zero.

The strains in terms of the displacements are given by:

$$\boldsymbol{\varepsilon} = \begin{cases} \varepsilon_{11} &= -x_3 \partial_{11} u \\ \varepsilon_{22} &= -x_3 \partial_{22} u \\ \varepsilon_{12} &= -2 x_3 \partial_{12} u \end{cases} \tag{3.44}$$

while the stresses are given by

$$\boldsymbol{\sigma} = \begin{Bmatrix} \sigma_{11} \\ \sigma_{22} \\ \sigma_{12} \end{Bmatrix} = \frac{E}{(1-\nu^2)} \begin{bmatrix} 1 & \nu & 0 \\ \nu & 1 & 0 \\ 0 & 0 & \dfrac{(1-\nu)}{2} \end{bmatrix} \begin{Bmatrix} \varepsilon_{11} \\ \varepsilon_{22} \\ \varepsilon_{12} \end{Bmatrix} \tag{3.45}$$

which can be written as

$$\boldsymbol{\sigma} = \frac{E}{(1-\nu^2)} \mathbf{D}\boldsymbol{\varepsilon} \tag{3.46}$$

where $\mathbf{D}$ is the constitutive matrix:

$$\mathbf{D} = D \begin{bmatrix} 1 & \nu & 0 \\ \nu & 1 & 0 \\ 0 & 0 & (1-\nu)/2 \end{bmatrix} \tag{3.47}$$

and D is known as the plate bending stiffness

$$D = \frac{Eh^3}{12(1-\nu^2)} \tag{3.48}$$

The bending moments are defined as

$$\mathbf{m} = \begin{Bmatrix} m_{11} \\ m_{22} \\ m_{12} \end{Bmatrix} = D \begin{bmatrix} 1 & \nu & 0 \\ \nu & 1 & 0 \\ 0 & 0 & \dfrac{(1-\nu)}{2} \end{bmatrix} \begin{Bmatrix} -\partial_{11} u \\ -\partial_{22} u \\ -2\partial_{12} u \end{Bmatrix} \tag{3.49}$$

Finally, the shear forces are defined as

$$\mathbf{Q} = \begin{cases} Q_1 &= -D\left(\partial_{111} u + \partial_{122} u\right) \\ Q_2 &= -D\left(\partial_{222} u + \partial_{112} u\right) \end{cases} \tag{3.50}$$

3.6.1 Strong Form

The outward unit normal vector to the boundary is $\mathbf{n}$, and $\mathbf{s}$ is the unit tangent vector such that $\mathbf{n} \times \mathbf{s} = x_3$. Greek indices, α and β, take the values 1 and 2 respectively, and repeated indices imply summation. Normal and tangential components are denoted $(\cdot)_n = ()_\alpha n_\alpha$ and $(\cdot)_s = ()_\alpha s_\alpha$, respectively.

If the boundary Γ is not smooth, the corners, where the normal undergoes a discontinuity, are denoted $\partial\Gamma = x_c$. Here, $x_c \in \Gamma$, $c = 1, 2, ...$ are the corner locations.

Applying all the constitutive equations presented on the previous section, we obtain the following BVP for the Kirchhoff-Love plate theory:

$$\begin{array}{ccc} -D\partial_{\alpha\beta}m_{\alpha\beta} = q & \text{in} & \Omega \\ u = W & \text{on} & \Gamma_W \\ \partial_n u = \Theta & \text{on} & \Gamma_\Theta \\ m_{nn} = M_n & \text{on} & \Gamma_M \\ \partial_\alpha m_{n\alpha} + \partial_s m_{ns} = Q + \partial s M_s & \text{on} & \Gamma_Q \\ [m_{ns}] = [M_s] & \text{on} & \partial\Gamma \cap \Gamma_Q \end{array} \tag{3.51}$$

where q is the distributed loading on the plate, W is the prescribed displacement on Γ_W of the plate, Θ is the prescribed rotation on Γ_Θ, M_n the prescribed normal bending moment on Γ_M, Q and M_s the prescribed tangential bending moment and shear force on Γ_Q, respectively, and $[M_s]$ represents a corner force imposed on non smooth domains.

3.6.2 Weak Form

The variational formulation or weak form of the Kirchhoff-Love plate theory [114] corresponds to find a function $u \in H^2(\Omega)$ that satisfy $u = W$ on Γ_W and $\partial_n u = \Theta$ on Γ_Θ such that for any $v \in H^2(\Omega)$ that satisfy $v = 0$ on Γ_W and $\partial_n v = 0$ on Γ_Θ:

$$a(v,u) = l(v) \tag{3.52}$$

$$a(v,u) = D\int_\Omega \left[\nu\Delta u\delta_{\alpha\beta} + (1-\nu)\partial_{\alpha\beta}u\right]\partial_{\alpha\beta}v\mathrm{d}\Omega \tag{3.53}$$

$$l(v) = \int_\Omega qv\mathrm{d}\Omega + \int_{\Gamma_Q}\left(Q + \partial sM_s\right)v\mathrm{d}\Gamma - \int_{\Gamma_M} M_n\partial_n v\mathrm{d}\Gamma - [M_s]v \tag{3.54}$$

Again, following the procedure described in Section 3.3.1, the discretization of the weak form (3.53), (3.54) with GIFT leads to the following coefficients for the linear system of equations (eq.(3.14)):

$$\mathbf{K}_{ij} = D\int_\Omega \left[\nu\Delta\left(M_i\circ\mathbf{F}^{-1}\right)\delta_{\alpha\beta} + (1-\nu)\partial_{\alpha\beta}\left(M_i\circ\mathbf{F}^{-1}\right)\right]\partial_{\alpha\beta}\left(M_j\circ\mathbf{F}^{-1}\right)\mathrm{d}\Omega \tag{3.55}$$

$$\begin{aligned}\mathbf{f}_j = &\int_\Omega q\left(M_j\circ\mathbf{F}^{-1}\right)\mathrm{d}\Omega + \int_{\Gamma_Q}\left(Q+\partial sM_s\right)\left(M_j\circ\mathbf{F}^{-1}\right)\mathrm{d}\Gamma \\ &- \int_{\Gamma_M} M_n\partial_n\left(M_j\circ\mathbf{F}^{-1}\right)\mathrm{d}\Gamma - [M_s]\left(M_j\circ\mathbf{F}^{-1}\right)\end{aligned} \tag{3.56}$$

Also, the stiffness matrix and the force vector can be denoted by the following matrix products [13]:

$$\mathbf{K} = \int_{\Omega} \mathbf{B}\mathbf{D}\mathbf{B}^{\mathbf{T}} \mathrm{d}\Omega \tag{3.57}$$

With,

$$\mathbf{B} = \begin{bmatrix} -\partial_{11}\left(M_1 \circ \mathbf{F}^{-1}\right) & -\partial_{11}\left(M_2 \circ \mathbf{F}^{-1}\right) & \cdots & -\partial_{11}\left(M_{n-1} \circ \mathbf{F}^{-1}\right) & -\partial_{11}\left(M_m \circ \mathbf{F}^{-1}\right) \\ -\partial_{22}\left(M_1 \circ \mathbf{F}^{-1}\right) & -\partial_{22}\left(M_2 \circ \mathbf{F}^{-1}\right) & \cdots & -\partial_{22}\left(M_{n-1} \circ \mathbf{F}^{-1}\right) & -\partial_{22}\left(M_m \circ \mathbf{F}^{-1}\right) \\ -2\partial_{12}\left(M_1 \circ \mathbf{F}^{-1}\right) & -2\partial_{12}\left(M_2 \circ \mathbf{F}^{-1}\right) & \cdots & -2\partial_{12}\left(M_{n-1} \circ \mathbf{F}^{-1}\right) & -2\partial_{12}\left(M_m \circ \mathbf{F}^{-1}\right) \end{bmatrix}^T \tag{3.58}$$

The force vector is written as

$$\mathbf{f} = \int_{\Omega} q\mathbf{N}\mathrm{d}\Omega + \int_{\Gamma_Q} \left(Q + \partial s M_s\right)\mathbf{N}\mathrm{d}\Gamma - \int_{\Gamma_M} M_n \partial_n \mathbf{N}\mathrm{d}\Gamma - [M_s]\mathbf{N} \tag{3.59}$$

With,

$$\mathbf{N} = \begin{bmatrix} \left(M_1 \circ \mathbf{F}^{-1}\right) & \left(M_2 \circ \mathbf{F}^{-1}\right) & \cdots & \left(M_{n-1} \circ \mathbf{F}^{-1}\right) & \left(M_n \circ \mathbf{F}^{-1}\right) \end{bmatrix}^T \tag{3.60}$$

$$\mathbf{dN} = \begin{bmatrix} \partial_1\left(M_1 \circ \mathbf{F}^{-1}\right) & \partial_1\left(M_2 \circ \mathbf{F}^{-1}\right) & \cdots & \partial_1\left(M_{n-1} \circ \mathbf{F}^{-1}\right) & \partial_1\left(M_n \circ \mathbf{F}^{-1}\right) \\ \partial_2\left(M_1 \circ \mathbf{F}^{-1}\right) & \partial_2\left(M_2 \circ \mathbf{F}^{-1}\right) & \cdots & \partial_2\left(M_{n-1} \circ \mathbf{F}^{-1}\right) & \partial_2\left(M_n \circ \mathbf{F}^{-1}\right) \end{bmatrix}^{\mathbf{T}} \tag{3.61}$$

$$\partial_n \mathbf{N} = \mathbf{dN} \cdot \mathbf{n} \tag{3.62}$$

In the previous equations $\partial_i\left(M_k \circ \mathbf{F}^{-1}\right)$ and $\partial_{ik}\left(M_k \circ \mathbf{F}^{-1}\right)$ are the first and second derivatives with respect to the geometry $\boldsymbol{x}(\boldsymbol{\xi}) = (x_1, x_2)$ computed by the chain rule, while n is the number of PHT-splines basis functions.

3.6.3 Vibration of plates

The strong form of the dynamic equilibrium equation for homogeneous and isotropic plates can be expressed by including the mass density ρ and plate thickness h into eq.(3.51)

$$-D\partial_{\alpha\beta} m_{\alpha\beta} + \rho h \ddot{u} = q \tag{3.63}$$

Considering that there is no damping or external loads acting on the solid, the equation of motion can be expressed in the following weak form:

$$D\int_{\Omega} \left[\nu \Delta u \delta_{\alpha\beta} + (1-\nu)\partial_{\alpha\beta} u\right] \partial_{\alpha\beta} v \mathrm{d}\Omega + \int_{\Omega} v\rho h \ddot{u} \mathrm{d}\Omega = 0 \tag{3.64}$$

Analogously to the previous section, the discretized week form can be written as

$$\mathbf{M}\ddot{\mathbf{U}} + \mathbf{K}\mathbf{U} = 0 \tag{3.65}$$

where $\mathbf{K}$ is the aforementioned stiffness matrix and $\mathbf{M}$ is known as the mass matrix, given by:

$$\mathbf{M} = \int_{\Omega} \rho h \mathbf{N}\mathbf{N}^{\mathbf{T}} d\Omega \tag{3.66}$$

The general solution of Eq. (3.65) that describes the unforced and undamped vibrations of a solid is [13]:

$$u = \overline{u}\mathrm{e}^{i\omega t} \tag{3.67}$$

In this equation, i is the imaginary unit, ω is the natural frequency, t is the time and $\overline{u}$ is the eigenvector associated to ω. Replacing this solution in the Eq. (3.67) [115], the natural frequencies of the plate can be found by solving the following eigenvalue problem:

$$\left(\mathbf{K} - \omega^2\mathbf{M}\right)\overline{\mathbf{U}} = 0 \tag{3.68}$$

The equation of eigenvalues has a non-trivial solution when it is fulfilled that:

$$\det\left(\mathbf{K} - \omega^2\mathbf{M}\right) = 0 \tag{3.69}$$

This last equation yields a discrete set of eigenvalues ω_i, with $i = 1, 2, 3, ...$; where each ω_i has an associated vector $\overline{\mathbf{U_i}}$, as shown in the following equation [104]:

$$\left(\mathbf{K} - \omega_i^2\mathbf{M}\right)\overline{\mathbf{U_i}} = 0 \tag{3.70}$$

3.6.4 XGIFT: Extended formulation for GIFT

In presence of a crack, the field approximation (eq.(3.12)) is enriched by additional degrees of freedom, representing the jump of displacement across the crack (Heaviside function) and a set of functions representing the asymptotic behaviour of the solution near the crack tip, i.e

$$u(\boldsymbol{x}) = \sum_{k\in J} \boldsymbol{U}_k M_k \circ \mathbf{F}^{-1}(\boldsymbol{x}) + \sum_{k\in L} M_k \circ \mathbf{F}^{-1}(\boldsymbol{x}) H(\boldsymbol{x}) \mathbf{d}_k + \sum_{k\in M} M_k \circ \mathbf{F}^{-1}(\boldsymbol{x}) \left(\sum_{i=1}^{4} F_i(r,\theta)\boldsymbol{c}_k^i\right) \tag{3.71}$$

where $\boldsymbol{U}_k$ are the regular unknown variables from eq.(3.12), $\mathbf{d}_k$ and $\boldsymbol{c}_k^i$ are the additional DOF related to the crack face and crack tip enrichment, respectively. The set J is the set of indexes for the PHT-Splines basis functions, while the sets L and M are the sets of indexes for crack face and crack tip enriched DOF, respectively.

The Heaviside function is defined as follows:

$$H(\boldsymbol{x}) = \begin{cases} 1 \text{ for nodes on one side of the crack} \\ -1 \text{ for nodes on another side of the crack} \end{cases} \tag{3.72}$$

The basis functions for the crack tip enrichment are defined as:

$$\{F_k(r,\theta)\} = \left\{ r^{3/2}\sin\left(\frac{3\theta}{2}\right), r^{3/2}\cos\left(\frac{3\theta}{2}\right), r^{3/2}\sin\left(\frac{\theta}{2}\right), r^{3/2}\cos\left(\frac{\theta}{2}\right) \right\} \tag{3.73}$$

where (r,θ) is the local polar coordinate system at the crack tip (see Figure 3.9).

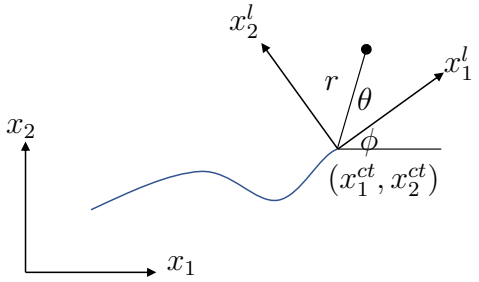

Figure 3.9: Local and global coordinates at the crack tip. (x_1, x_2) are the global coordinates, while (x_1^{ct}, x_2^{ct}) are the coordinates of the crack tip in the global system. ϕ is the angle between the crack tip and the horizontal line. (x_1^l, x_2^l) are the local coordinates rotated with respect to ϕ, and (r,θ) are the polar coordinates defined at (x_1^l, x_2^l). The blue line represents the crack

The transformation between the local polar coordinate system to the local Cartesian coordinate system at the crack tip is given as follows:

$$\begin{cases} r = \sqrt{{x_1^l}^2 + {x_2^l}^2} \\ \theta = \arctan\left(\dfrac{x_2^l}{x_1^l}\right) \end{cases} \tag{3.74}$$

The following is the transformation between the local Cartesian coordinate system at the crack tip (x_1^l, x_2^l) and the physical coordinates:

$$\begin{Bmatrix} x_1^l \\ x_2^l \end{Bmatrix} = \begin{bmatrix} \cos(\phi) & \sin(\phi) \\ -\sin(\phi) & \cos(\phi) \end{bmatrix} \begin{Bmatrix} x_1 - x_1^{ct} \\ x_2 - x_2^{ct} \end{Bmatrix} \tag{3.75}$$

Where (x_1, x_2) are the physical coordinates defined by eq.(3.11), (x_1^{ct}, x_2^{ct}) are the crack tip coordinates at the physical space and ϕ is the angle between the crack tip with respect to the horizontal line.

The level set method is a numerical method used to track interfaces and shapes, it was originally introduced by Osher and Sethian [116] for tracking the evolution of moving boundaries and now is typically used in XFEM method [117, 89] or XIGA method [15] to identify discontinuities on the geometry like cracks, inclusions or voids.

In this work, we employ both level set functions to select which elements in the field discretization (eq.(3.12)) should be enriched by the Heaviside or crack tip criteria. Then, their respective DOF are enriched with the criteria aforementioned. Figure 3.10 illustrates an example of the enriched vertex of a T-mesh.

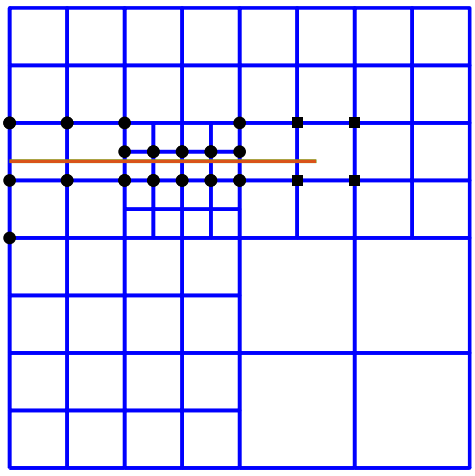

Figure 3.10: Illustration of the enriched vertex on a T-mesh. The red thick line denotes the crack. The black dots denotes the Heaviside enriched vertex, while the black squares denotes the crack tip enriched vertex

Using the generalized formulation for the unknown vector give by eq.(3.71), the eq.(3.14) and the level set method to identify elements enriched with the Heaviside and crack tip functions, the generalized linear system is given by:

$$\mathbf{K_{enr}U_{enr}} = \mathbf{f_{enr}} \tag{3.76}$$

Where the displacement control variables and additional enrichment DOF are as follow:

$$\mathbf{U_{enr}} = \begin{Bmatrix} \mathbf{U} & \mathbf{d} & \mathbf{c_1} & \mathbf{c_2} & \mathbf{c_3} & \mathbf{c_4} \end{Bmatrix}^{\mathbf{T}} \tag{3.77}$$

where $\mathbf{U}$, $\mathbf{d}$ and $\mathbf{c_i}$, $i = 1, 2, 3, 4$, are the vectors of regular DOF, crack face DOF and crack tip DOF, respectively.

In this section, we will denote the composition $M_k \circ \mathbf{F}^{-1}$ as N_k^*. The stiffness matrix enriched $\mathbf{K_{enr}}$ is a generalization for the eq.(3.57) and is given by:

$$\mathbf{K_{enr}} = \int_\Omega \mathbf{B_{enr}} \mathbf{D} \mathbf{B_{enr}^T} \mathrm{d}\Omega \tag{3.78}$$

with $\mathbf{B_{enr}}$ defined as

$$\mathbf{B_{enr}} = \begin{bmatrix} \mathbf{B} & \mathbf{B_d} & \mathbf{B_{c_1}} & \mathbf{B_{c_2}} & \mathbf{B_{c_3}} & \mathbf{B_{c_4}} \end{bmatrix}^\mathbf{T} \tag{3.79}$$

$$\mathbf{B} = \begin{bmatrix} -\partial_{11} N_1^* & -\partial_{11} N_2^* & \cdots & -\partial_{11} N_{n-1}^* & -\partial_{11} N_n^* \\ -\partial_{22} N_1^* & -\partial_{22} N_2^* & \cdots & -\partial_{22} N_{n-1}^* & -\partial_{22} N_n^* \\ -2\partial_{12} N_1^* & -2\partial_{12} N_2^* & \cdots & -2\partial_{12} N_{n-1}^* & -2\partial_{12} N_n^* \end{bmatrix} \tag{3.80}$$

$$\mathbf{B_d} = \begin{bmatrix} -\partial_{11} N_1^* H & -\partial_{11} N_2^* H & \cdots & -\partial_{11} N_{n_{cf}-1}^* H & -\partial_{11} N_{n_{cf}}^* H \\ -\partial_{22} N_1^* H & -\partial_{22} N_2^* H & \cdots & -\partial_{22} N_{n_{cf}-1}^* H & -\partial_{22} N_{n_{cf}}^* H \\ -2\partial_{12} N_1^* H & -2\partial_{12} N_2^* H & \cdots & -2\partial_{12} N_{n_{cf}-1}^* H & -2\partial_{12} N_{n_{cf}}^* H \end{bmatrix} \tag{3.81}$$

$$\mathbf{B_{c_i}} = \begin{bmatrix} -\partial_{11}\left(N_1^* F_i\right) & -\partial_{11}\left(N_2^* F_i\right) & \cdots & -\partial_{11}\left(N_{n_{ct}-1}^* F_i\right) & -\partial_{11}\left(N_{n_{ct}}^* F_i\right) \\ -\partial_{22}\left(N_1^* F_i\right) & -\partial_{22}\left(N_2^* F_i\right) & \cdots & -\partial_{22}\left(N_{n_{ct}-1}^* F_i\right) & -\partial_{22}\left(N_{n_{ct}}^* F_i\right) \\ -2\partial_{12}\left(N_1^* F_i\right) & -2\partial_{12}\left(N_2^* F_i\right) & \cdots & -2\partial_{12}\left(N_{n_{ct}-1}^* F_i\right) & -2\partial_{12}\left(N_{n_{ct}}^* F_i\right) \end{bmatrix} \quad , \quad i = 1,2,3,4 \tag{3.82}$$

where n is the number of PHT-splines basis functions, n_{cf} the number of Heaviside enriched basis functions, and n_{ct} the number of crack tip enriched basis functions. Analogously, the enriched force $\mathbf{f_{enr}}$ and mass $\mathbf{M_{enr}}$ are generalizations of eq.(3.59) and (3.66), respectively:

$$\mathbf{f_{enr}} = \int_\Omega q \mathbf{N_{enr}} \mathrm{d}\Omega + \int_{\Gamma_Q} \left(Q + \partial s M_s\right) \mathbf{N_{enr}} \mathrm{d}\Gamma - \int_{\Gamma_M} M_n \partial_n \mathbf{N_{enr}} \mathrm{d}\Gamma - [M_s] \mathbf{N_{enr}} \tag{3.83}$$

$$\mathbf{M_{enr}} = \int_\Omega \rho h \mathbf{N_{enr}} \mathbf{N_{enr}^T} d\Omega \tag{3.84}$$

where

$$\mathbf{N_{enr}} = \begin{bmatrix} \mathbf{N} & \mathbf{N_d} & \mathbf{N_{c_1}} & \mathbf{N_{c_2}} & \mathbf{N_{c_3}} & \mathbf{N_{c_4}} \end{bmatrix}^\mathbf{T} \tag{3.85}$$

$$\mathbf{N} = \begin{bmatrix} N_1^* & N_2^* & \cdots & N_{n-1}^* & N_n^* \end{bmatrix} \tag{3.86}$$

$$\mathbf{N_d} = \begin{bmatrix} N_1^* H & N_2^* H & \cdots & N_{n_{cf}-1}^* H & N_{n_{cf}}^* H \end{bmatrix} \tag{3.87}$$

$$\mathbf{N_{c_i}} = \begin{bmatrix} N_1^* F_i & N_2^* F_i & \cdots & N_{n_{ct}-1}^* F_i & N_{n_{ct}}^* F_i \end{bmatrix} \quad , \quad i = 1, 2, 3, 4 \tag{3.88}$$

$$\mathbf{dN_{enr}} = \begin{bmatrix} \mathbf{dN} & \mathbf{dN_d} & \mathbf{dN_{c_1}} & \mathbf{dN_{c_2}} & \mathbf{dN_{c_3}} & \mathbf{dN_{c_4}} \end{bmatrix}^{\mathbf{T}} \tag{3.89}$$

$$\mathbf{dN} = \begin{bmatrix} \partial_1 N_1^* & \partial_1 N_2^* & \cdots & \partial_1 N_{n-1}^* & \partial_1 N_n^* \\ \partial_2 N_1^* & \partial_2 N_2^* & \cdots & \partial_2 N_{n-1}^* & \partial_2 N_n^* \end{bmatrix} \tag{3.90}$$

$$\mathbf{dN_d} = \begin{bmatrix} \partial_1 N_1^* H & \partial_1 N_2^* H & \cdots & \partial_1 N_{n_{cf}-1}^* H & \partial_1 N_{n_{cf}}^* H \\ \partial_2 N_1^* H & \partial_2 N_2^* H & \cdots & \partial_2 N_{n_{cf}-1}^* H & \partial_2 N_{n_{cf}}^* H \end{bmatrix} \tag{3.91}$$

$$\mathbf{dN_{c_i}} = \begin{bmatrix} \partial_1 \left(N_1^* F_i \right) & \partial_1 \left(N_2^* F_i \right) & \cdots & \partial_1 \left(N_{n_{ct}-1}^* F_i \right) & \partial_1 \left(N_{n_{ct}}^* F_i \right) \\ \partial_2 \left(N_1^* F_i \right) & \partial_2 \left(N_2^* F_i \right) & \cdots & \partial_2 \left(N_{n_{ct}-1}^* F_i \right) & \partial_2 \left(N_{n_{ct}}^* F_i \right) \end{bmatrix} \quad , \quad i = 1, 2, 3, 4 \tag{3.92}$$

$$\mathbf{dN_n^{enr}} = \mathbf{dN_{enr}} \cdot \mathbf{n} \tag{3.93}$$

Again, in the previous equations $\partial_i N_k^*$ and $\partial_{ik} N_k^*$ are the first and second derivatives with respect to the geometry $\boldsymbol{x}(\boldsymbol{\xi}) = (x_1, x_2)$ computed by the chain rule. And N^* denotes the composition between the physical mapping and the field basis $M_k \circ \mathbf{F}^{-1}$.

Two types of crack tip enrichment criteria can be applied, namely the geometrical criteria and the topological criteria [118]. In the first one, the element containing the crack tip is enriched, while in the second one, a fixed area of enrichment remains constant in the refinement process. In this work we opted for the topological criteria, since the main goal is to apply adaptive refinement, and geometrical enrichment makes the model computationally expensive.

3.6.5 Computation of Stress Intensity Factors (SIF)

In this section we briefly explain the theory and procedure employed in order to compute the stress intensity factors (SIF) in the context of Kirchhoff-Love plate theory.

Asymptotic Displacement near the Crack Tip and Fracture Modes

In the Kirchhoff-Love plate theory, there are two fracture modes depending on the loading type: a symmetric bending, known as mode k_1, and anti-symmetric bending mode k_2. Both fracture modes are showing in Figure 3.11.

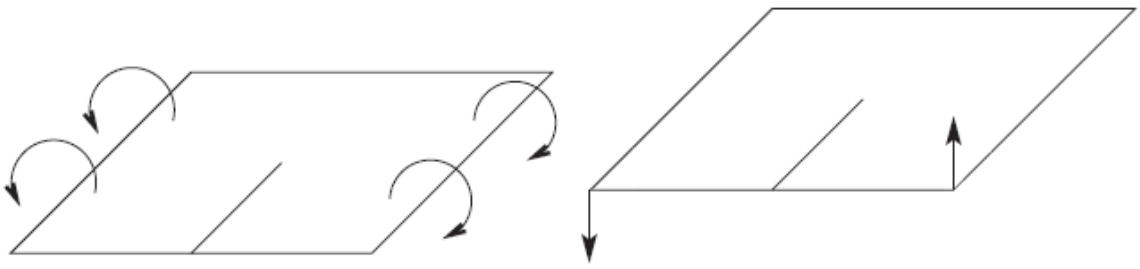

(a) k_1 (b) k_2

Figure 3.11: Loading modes for Kirchhoff-Love plate theory: (a) Symmetric bending (k_1) and (b) Anti-symmetric bending (k_2)

The stress field close to the tip of a through crack in a plate was first obtained by Williams [119] in the context of Kirchhoff-Love plate model using an eigenfunction approach to solve the bi-harmonic equation, given by eq. (3.51). The asymptotic displacement field u_{asymp} is given by [120, 121, 122]:

$$u_{asymp} = k_1 \frac{(2r)^{\frac{3}{2}}(1-\nu^2)}{2Eh(3+\nu)} \left[\frac{1}{3} \left(\frac{7+\nu}{1-\nu} \right) \cos\left(\frac{3\theta}{2} \right) - \cos\left(\frac{\theta}{2} \right) \right] + k_2 \frac{(2r)^{\frac{3}{2}}(1-\nu^2)}{2Eh(3+\nu)} \left[\frac{1}{3} \left(\frac{5+3\nu}{1-\nu} \right) \sin\left(\frac{3\theta}{2} \right) - \sin\left(\frac{\theta}{2} \right) \right] \tag{3.94}$$

Where k_1 and k_2 are defined as:

$$k_1 = \lim_{r \to 0} \sqrt{2r} \sigma_{\theta\theta}(r, 0) \quad , \quad k_2 = \lim_{r \to 0} \left(\frac{3+\nu}{1+\nu} \right) \sqrt{2r} \sigma_{r\theta}(r, 0) \tag{3.95}$$

The stress field due to bending for Kirchhoff-Love plate theory, in polar coordinate (r, θ) with respect to the crack tip, are given as follow [123, 101]:

$$\begin{Bmatrix} \sigma_{rr} \\ \sigma_{\theta\theta} \\ \sigma_{r\theta} \end{Bmatrix} = k_1 \frac{x_3}{2h\sqrt{2r}(3+\nu)} \begin{Bmatrix} (3+5\nu)\cos\left(\frac{\theta}{2}\right) - (7+\nu)\cos\left(\frac{3\theta}{2}\right) \\ (5+3\nu)\cos\left(\frac{\theta}{2}\right) + (7+\nu)\cos\left(\frac{3\theta}{2}\right) \\ -(1-\nu)\sin\left(\frac{\theta}{2}\right) + (7+\nu)\sin\left(\frac{3\theta}{2}\right) \end{Bmatrix} + k_2 \frac{x_3}{2h\sqrt{2r}(3+\nu)} \begin{Bmatrix} -(3+5\nu)\sin\left(\frac{\theta}{2}\right) + (5+3\nu)\sin\left(\frac{3\theta}{2}\right) \\ -(5+3\nu)\left(\sin\left(\frac{\theta}{2}\right) + \sin\left(\frac{3\theta}{2}\right)\right) \\ (\nu-1)\cos\left(\frac{\theta}{2}\right) + (5+3\nu)\cos\left(\frac{3\theta}{2}\right) \end{Bmatrix} \tag{3.96}$$

The relation between the stress in polar coordinates with the local coordinates with respect to the crack tip is given by [124],

$$\begin{Bmatrix} \sigma_{rr} \\ \sigma_{\theta\theta} \\ \sigma_{r\theta} \end{Bmatrix} = \begin{bmatrix} \cos^2(\phi) & \sin^2(\phi) & 2\sin(\phi)\cos(\phi) \\ \sin^2(\phi) & \cos^2(\phi) & -2\sin(\phi)\cos(\phi) \\ -\sin(\phi)\cos(\phi) & \sin(\phi)\cos(\phi) & \cos^2(\phi) - \sin^2(\phi) \end{bmatrix} \begin{Bmatrix} \sigma_{11}^l \\ \sigma_{22}^l \\ \sigma_{12}^l \end{Bmatrix} \tag{3.97}$$

where ϕ is the angle defined in Section 3.6.4. The previous stress relationship can also be written in the following matrix form as

$$\boldsymbol{\sigma_{polar}} = \mathbf{T}(\phi)\boldsymbol{\sigma_{local}} \tag{3.98}$$

The inverse relationship also holds:

$$\boldsymbol{\sigma_{local}} = \mathbf{T^{-1}}(\phi)\boldsymbol{\sigma_{polar}} \tag{3.99}$$

3.6.6 J-Integral and Interaction Integral

J-integral is commonly used in fracture mechanics to determine SIF. In this work we use the domain integral definition for a through-the-thickness crack with the crack front normal to the mid-surface [123, 125], i.e.

$$J = \frac{1}{h}\int_V \left(\sigma_{ij}\frac{\partial u_i}{\partial x_1} - \frac{1}{2}\sigma_{ij}\varepsilon_{ij}\delta_{1j}\right)\frac{\partial q}{\partial x_j}\mathrm{d}V \tag{3.100}$$

where V is an arbitrary volume that encloses the crack tip, q is the value of weight function varying from 0 (the outer contour of V) to 1 (the inner contour of V). Figure 3.12 shows the volume V and the different surfaces which comprise it. The relationship between the J-integral value and the stress intensity factors in the cases of mixed-mode loadings for the Kirchhoff-Love plate theory is given by [121]:

$$J = G = \frac{\pi}{3E}\left(\frac{1+\nu}{3+\nu}\right)\left(k_1^2 + k_2^2\right), \tag{3.101}$$

where k_1 and k_2 are the symmetric and anti-symmetric bending SIF [121]. To calculate the SIF for a particular mode of loading in cases of mixed-mode loading, we follow the scheme which was derived in [87, 126] for two and three-dimensional problems. We consider two states of a cracked solid: corresponding to the present state $\left(\sigma_{ij}^{(1)}, \varepsilon_{ij}^{(1)}, u_i^{(1)}\right)$ and an auxiliary state $\left(\sigma_{ij}^{(2)}, \varepsilon_{ij}^{(2)}, u_i^{(2)}\right)$ which will be chosen as the numerical field and the asymptotic field, respectively. From eq. (3.100), the domain form of the J-integral for the superposition of the two state is:

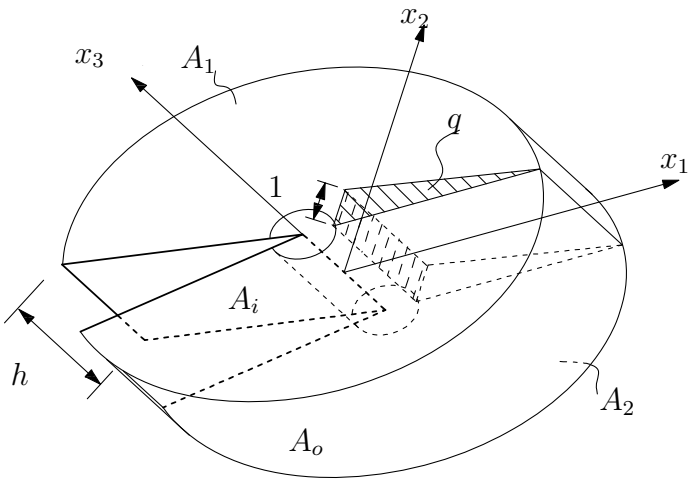

Figure 3.12: J-integral: Definition of the domain in the equivalent domain integral method. Adapted from [123].

$$J^{(1+2)} = \frac{1}{h}\int_V \left[\left(\sigma_{ij}^{(1)} + \sigma_{ij}^{(2)}\right)\left(\frac{\partial u_i^{(1)}}{\partial x_1} + \frac{\partial u_i^{(2)}}{\partial x_1}\right) - \frac{1}{2}\left(\sigma_{ij}^{(1)} + \sigma_{ij}^{(2)}\right)\left(\varepsilon_{ij}^{(1)} + \varepsilon_{ij}^{(2)}\right)\delta_{1j}\right]\frac{\partial q}{\partial x_j}\mathrm{d}V \tag{3.102}$$

Expanding and grouping terms of similar states in the eq. (3.102), we can written this as:

$$J^{(1+2)} = J^{(1)} + J^{(2)} + I^{(1,2)} \tag{3.103}$$

Where,

$$J^{(\alpha)} = \frac{1}{h}\int_V \left(\sigma_{ij}^{(\alpha)}\frac{\partial u_i^{(\alpha)}}{\partial x_1} - \frac{1}{2}\sigma_{ij}^{(\alpha)}\varepsilon_{ij}^{(\alpha)}\delta_{1j}\right)\frac{\partial q}{\partial x_j}\mathrm{d}V \quad , \quad \alpha = 1,2 \tag{3.104}$$

And the interaction integral $I^{(1,2)}$ is given by:

$$I^{(1,2)} = \frac{1}{h}\int_V \left(\sigma_{ij}^{(1)}\frac{\partial u_i^{(2)}}{\partial x_1} + \sigma_{ij}^{(2)}\frac{\partial u_i^{(1)}}{\partial x_1} - \sigma_{ij}^{(1)}\varepsilon_{ij}^{(2)}\delta_{1j}\right)\frac{\partial q}{\partial x_j}\mathrm{d}V \tag{3.105}$$

Using the eq. (3.101), the J-integral for the combination of the states 1 and 2 is:

$$J^{(1+2)} = J^{(1)} + J^{(2)} + \frac{2\pi}{3E}\left(\frac{1+\nu}{3+\nu}\right)\left(k_1^{(1)}k_1^{(2)} + k_2^{(1)}k_2^{(2)}\right) \tag{3.106}$$

Using the equations (3.103) and (3.106), the relationship between the interaction integral $I^{(1,2)}$, given by eq. (3.105), and the stress intensity factors is:

$$I^{(1,2)} = \frac{2\pi}{3E}\left(\frac{1+\nu}{3+\nu}\right)\left(k_1^{(1)}k_1^{(2)} + k_2^{(1)}k_2^{(2)}\right) \tag{3.107}$$

To obtain the stress intensity factor, we choose the auxiliary state as one of the two modes of the plate: pure symmetric bending loading or pure anti-symmetric bending loading, as shown in Figure 3.11; and then, we use the eq. (3.107) to express $k_1^{(1)}$ and $k_2^{(1)}$. For instance, if we choose the pure symmetric bending mode, the asymptotic fields will have $k_1^{(2)} = 1$ and $k_2^{(2)} = 0$. Then, the stress intensity factors $k_1^{(1)}$ is expressed as

$$k_1^{(1)} = \frac{3E}{2\pi}\left(\frac{3+\nu}{1+\nu}\right) I^{(1,2)} \tag{3.108}$$

A similar procedure can be done to derive an expression for $k_2^{(1)}$.

Concerning the numerical implementation, the J-integral domain is defined by the elements that cut a circular cylinder with central axis being the crack front and radius r_d equal to 2.5 times the mean value of the square root of the fully cracked elements' areas [123, 127] (Figure 3.13). This strategy is further refereed as $r_{\mathrm{d}_{shrinking}}$ in our results. Another approach is to take r_d fixed. In this work both approach were tested, leading to similar results.

The q function is defined inside each PHT-spline element of the Interaction integral domain as:

$$q = \sum_{i=1}^{4} N_i(x_1, x_2) q_i \tag{3.109}$$

where N_i are linear basis function, and the coefficients q_i is defined as 1 for the vertices of the element that lies on the inner boundary, while is equal to zero is the node is on the outer boundary of the volume V.

3.6.7 A posteriori error-estimates for the Kirchhoff-Love equation

Again, following the theory introduced in Section 3.4, we proceed to present the error estimator employed for the Kirchhoff-Love equation. For this particular case, only the recovery-based error estimator was proposed, since the results for the Helmholtz equation proved that both error estimators lead to similar outcome and the implementation of the recovery-based error estimator is cheaper in terms of coding and computation cost compared to the residual based, error estimator.

Recovery-based error estimates for the Helmholtz equation

Section 3.4 already showed how to derive the recovery-based error estimator for PHT-Splines using super-convergent patch recovery for the Helmholtz equation. What follows is the adaption of this procedure to the Kirchhoff-love plate theory [128].

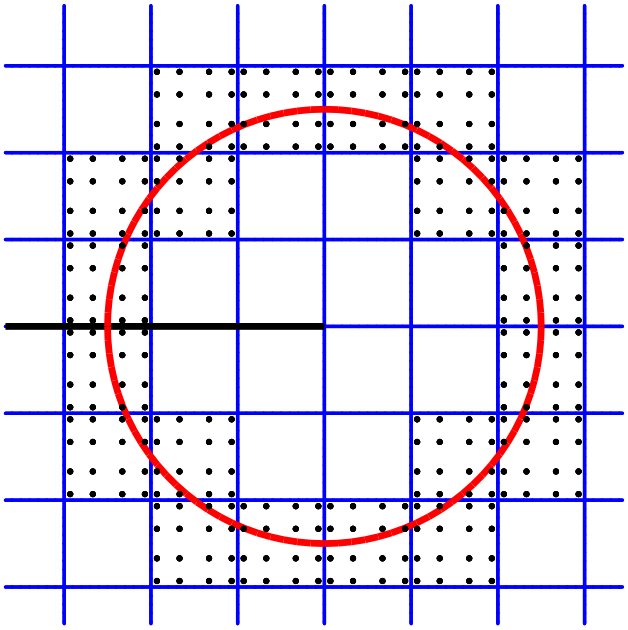

Figure 3.13: J-integral: selected domain for the integration. Red line represents the circle of radius r_{d}, the black line represents the crack

Eq. (3.21) showed the error estimator proposed for the Helmholtz equation. Analogously, the error estimator for the Kirchhoff-Love equation is computed in the normalized H^2 semi-norm as:

$$\frac{\|\mathrm{e}_{rec}\|_{H^2}}{\|G\left[\mathbf{m}(u_h)\right]\|_{H^2}} = \frac{\left(\int_\Omega \left(G\left[\mathbf{m}(u_h)\right] - \mathbf{m}(u_h)\right)^T \mathbf{D}^{-1} \left(G\left[\mathbf{m}(u_h)\right] - \mathbf{m}(u_h)\right) \mathrm{d}\Omega\right)^{1/2}}{\left(\int_\Omega \left(G\left[\mathbf{m}(u_h)\right]\right)^T \mathbf{D}^{-1} \left(G\left[\mathbf{m}(u_h)\right]\right) \mathrm{d}\Omega\right)^{1/2}} \tag{3.110}$$

where $\mathbf{m}(u_h)$ is the numerical moment, computed using eq.(3.49), $G\left[\mathbf{m}(u_h)\right]$ is the recovery moment computed using $\mathbf{m}(u_h)$. In the same way as for the Helmholtz equation, the error indicator on each cell K can be computed as:

$$\mathrm{e}_k = \left(\int_\Omega \left(G\left[\mathbf{m}(u_h)\right] - \mathbf{m}(u_h)\right)^T \mathbf{D}^{-1} \left(G\left[\mathbf{m}(u_h)\right] - \mathbf{m}(u_h)\right) \mathrm{d}\Omega\right)^{1/2} \tag{3.111}$$

The same superconvergent points (Table 3.4) are employed to computed the recovery solution.

The procedure to compute the recovery moment solution $G\left[\mathbf{m}(u_h)\right]$ is explained as follows:

Let be Ω be the domain and Ω_k, $k = 1, ..., n$ a set of n non-overlapping patches such that together they form Ω: $\cup_{k=1}^{n} \Omega_k = \Omega$. Let $\boldsymbol{x}^*_{i,k}$ $(i = 1, ...N_k)$ be a set of N_k super-convergent points defined over the patch Ω_k. Let also $\phi^*_{i,k}$ be the set of basis functions employed for the recovery solution. In this case we employ B-splines functions of degree $p^* \geq p$ and continuity $\alpha^* \geq \alpha$. The $G\left[m(u_h)\right]$ is constructed as:

$$G\left[\mathbf{m}(u_h)\right](\boldsymbol{x}) = \sum \phi^*_{i,k}(\boldsymbol{x})\boldsymbol{C}^*_{i,k} \tag{3.112}$$

where $\boldsymbol{C}^*_{i,k}$ are the new DOF associated with the recovery gradient solution. In this case, we require equation (3.112) to fulfill the condition:

$$G\left[\mathbf{m}(u_h)\right](\boldsymbol{x}^*_{i,k}) = \mathbf{m}(u_h)(\boldsymbol{x}^*_{i,k}) \tag{3.113}$$

Equation (3.113) can be rewritten as the following linear system:

$$\boldsymbol{A}^k\boldsymbol{C}^*_k = \boldsymbol{b}^{\boldsymbol{k}} \tag{3.114}$$

where

$$\boldsymbol{A}^k_{ij} = \phi^*_{j,k}(\boldsymbol{x}^*_{i,k}) \tag{3.115}$$

$$\boldsymbol{b}^{\boldsymbol{k}}_i = \left[\frac{\partial u_h(\boldsymbol{x}^*_{i,k})}{\partial x_1}, \frac{\partial u_h(\boldsymbol{x}^*_{i,k})}{\partial x_2}\right] \tag{3.116}$$

Finally, the recovery solution can be computed by solving equation (3.114).

3.6.8 Dynamic analysis and adaptive refinement

In the case of the dynamic analysis, two different schemes can drive the adaptive results: The first one consists in taking each mode independently and drive the adaptive refinement based on the recovery-based error estimator computed using that particular vibration mode. This scheme leads to high memory costs since for each vibration mode the corresponding refinement needs to be stored and processed. The second scheme consists in taking a particular static solution (for instance, the result for the clamped problem with constant loading) and using it to drive the adaptive refinement and compute the desired vibration modes.

In this work, both methods were tried, leading to similar results, we, therefore, choose for the second method, since this one requires less computational resources.

Chapter 4

Numerical results: Helmholtz equation

The following chapter is devoted to show the numerical results obtained for the Helmholtz equation for 2 and 3D problems.

For problems with known analytical solutions, we use the following relative L^2 norm and H^1 semi-norm of the error:

$$\frac{\|u-u_h\|_{L^2}}{\|u\|_{L^2}} = \sqrt{\frac{\int_\Omega (u-u_h)^2 \,\mathrm{d}\Omega}{\int_\Omega (u)^2 \,\mathrm{d}\Omega}} \tag{4.1}$$

$$\frac{\|u-u_h\|_{H^1}}{\|u\|_{H^1}} = \sqrt{\frac{\left(\int_\Omega (\nabla u - \nabla u_h)^T (\nabla u - \nabla u_h) \,\mathrm{d}\Omega\right)}{\left(\int_\Omega (\nabla u)^T (\nabla u) \,\mathrm{d}\Omega\right)}} \tag{4.2}$$

4.1 2D Numerical Examples

4.1.1 The L-shape domain

In this example, we consider the Helmholtz boundary value problem in an L-shape domain, studied in [129]. The geometry of the domain in shown in Figure 4.1. The part of the boundary, corresponding to edges $x = 0$ and $y = 0$ is considered as homogeneous Dirichlet boundary Γ_D. On the rest of the boundary, Γ_R, Robin condition is prescribed.

We solve the following boundary value problem:

$$\begin{aligned} \Delta u + k^2 u &= 0 && \text{in } \Omega, \\ u &= 0 && \text{on } \Gamma_D, \\ \frac{\partial u}{\partial n} + iku &= g + ikg && \text{on } \Gamma_R. \end{aligned} \tag{4.3}$$

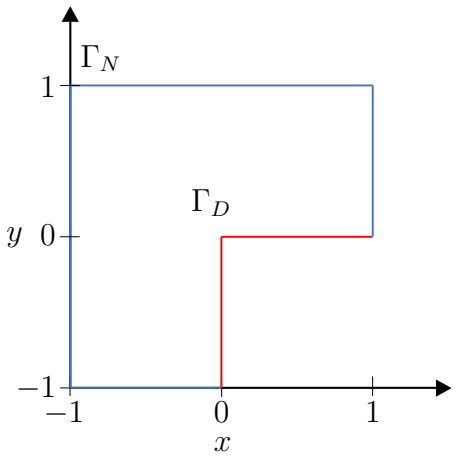

Figure 4.1: The L-Shape problem: domain

where g is the exact solution given by:

$$u^{\text{exact}}(r,\theta) = g(r,\theta) = J_\alpha(kr)\sin(\alpha\theta) \tag{4.4}$$

where $J_\alpha(x)$ is the Bessel function of the first kind of order $\alpha = \frac{2n}{3}$ with n integer. In this study we consider two cases: $n = 1$ and $n = 2$. In both cases the solution tends to 0 as $r \to 0$. However, for $n = 1$ the derivatives of order $k \geq 1$ are singular at $r = 0$, while in the case $n = 2$ the derivatives of order $k \geq 2$ are singular at $r = 0$. The real and imaginary parts of the analytic solution (4.4) for $\alpha = 2/3$ and $k = 40$ are shown in Fig. 4.2.

The L-shape domain is composed of three rectangular patches modeled by linear NURBS. The geometry is kept unaltered during the solution refinement process. Table A.1 shows the control points and knot vectors employed for the geometry parameterization.

In what follows we describe the numerical results for various degrees of polynomials p and different values of k, for uniform and adaptive refinements with two types of error estimators.

Figure 4.3 shows an initial mesh and five different adaptive meshes obtained by the recovery-based adaptive refinement, using $k = 10$ and $p = 3$. It can be seen that the algorithm performs gradient refinement towards the singular point. Similar patterns were observed in all simulations.

In figure 4.4 we show the comparison of the recovery-based and the residual-based error estimators for $k = 10$ and $p = 3$. It can be seen that in both cases, for $\alpha = 2/3$ and $\alpha = 4/3$ both error estimators yield quasi-identical results. It is interesting to notice that due to the reduced regularity of the solution for both values of parameter α, uniform refinement yields a sub-optimal convergence rate, while the adaptive refinement is capable of recovering the optimal convergence rate.

In figure 4.5 we analyze the performance of the refinement algorithm depending on the size of the initial mesh, i.e. the uniform mesh at which the adaptive refinement is started. Each initial mesh can be characterized by parameters $n_\lambda = \lambda/h$ (discretization density), kh/p, k^2h/p, listed in table 4.1 with $p = 3$ and $k = 40$. As it can be seen, meshes 0-2 are coarse,

	$n_\lambda = \lambda/h$	kh/p	k^2h/p
mesh 0	0.63	3.3333	133.3333
mesh 1	1.07	1.9518	78.0720
mesh 2	1.96	1.0675	42.7008
mesh 3	3.74	0.5601	22.4045
mesh 4	7.29	0.2872	11.4861
mesh 5	14.40	0.1454	5.8168
mesh 6	28.62	0.0732	2.9272
mesh 7	57.05	0.0367	1.4684

Table 4.1: Parameters, characterizing uniform mesh in figure 4.5, at which adaptive refinement is started

meshes 3-7 are in the pre-asymptotic range, where condition $kh/p < 1$ is fulfilled, but k^2h/p is still large. In the pre-asymptotic range, the full error is dominated by the pollution term, however, as it can be seen from figure 4.5, it has no effect on the performance of the error estimators and for all initial meshes, the error obtained by the adaptive algorithm converges to the same curve (optimal rate). It is interesting to notice, that the finer the initial mesh is, the faster the algorithm converges to the optimal rate curve. However, if the adaptive refinement is started on a coarse mesh, it has been observed in all studies, that the adaptive algorithm refines the mesh uniformly until the pre-asymptotic range is reached, and only after that starts capturing the local features of the solution. This is an expected result, since the global error of a solution in acoustics depends on the mesh density per wavelength.

While in both cases, $\alpha = 2/3$ and $\alpha = 4/3$, for the same value of k, adaptive algorithm return the optimal convergence rate, the gain in the convergence rate and the overall error is much more pronounced for solutions with higher order of singularity.

The same observation can be made from figure 4.7, which shows the L^2 error plot for different values of parameter k. In all cases, adaptive algorithms return optimal convergence rates. However, the efficiency of adaptive refinement in comparison with the uniform refinement for the solution with a higher order of singularity ($\alpha = 2/3$) is significantly higher than for the solution with the lower order of singularity ($\alpha = 4/3$), especially for increasing value of k. Both, recovery-based and residual-based error estimators yield quasi-identical results.

Figure 4.8 shows the L^2 error plot using uniform and recovery-based adaptive refinement with $k = 40$ for different degrees of PHT-splines. Due to the reduced regularity of the solution, the convergence rate is sub-optimal for all values of $p = 3, 4, 5, 6$ for the uniform refinement. In all cases, the adaptive refinement recovers the optimal convergence rate of $(p + 1)/2$, which demonstrates the efficiency of higher order approximations. For example, for DOF$\approx 10^5$, the L^2 error norm obtained with the adaptive refinement for $\alpha = 2/3$ and $\alpha = 4/3$ is about five orders of magnitude and three orders of magnitude smaller than their corresponding error in the approximation with the uniform refinement, respectively.

Figure 4.6 shows the effectivity index computed for the recovery-based adaptive refinement for $p = 3$ and different values of parameter k. The plots show that the effectivity index tends to 1 for every case, which implies that this error estimator is asymptotically exact.

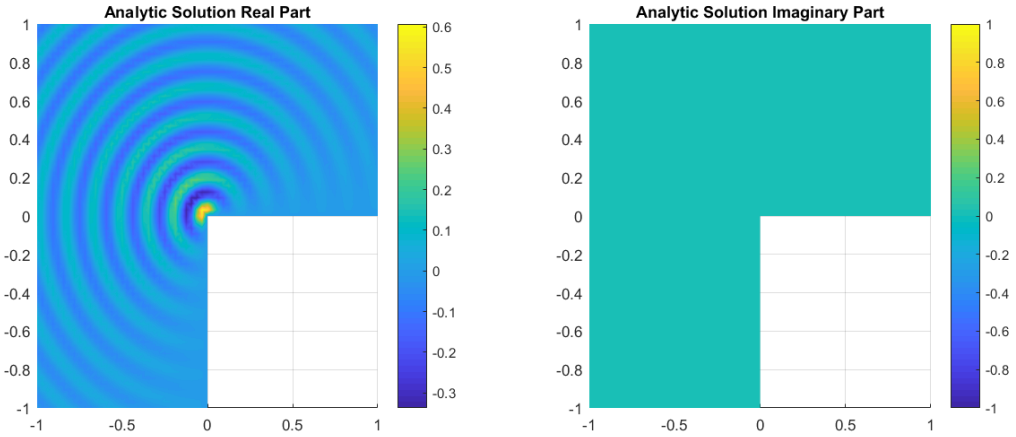

Figure 4.2: Analytical solution for the L-shaped problem with $\alpha = 2/3$ and $k = 40$

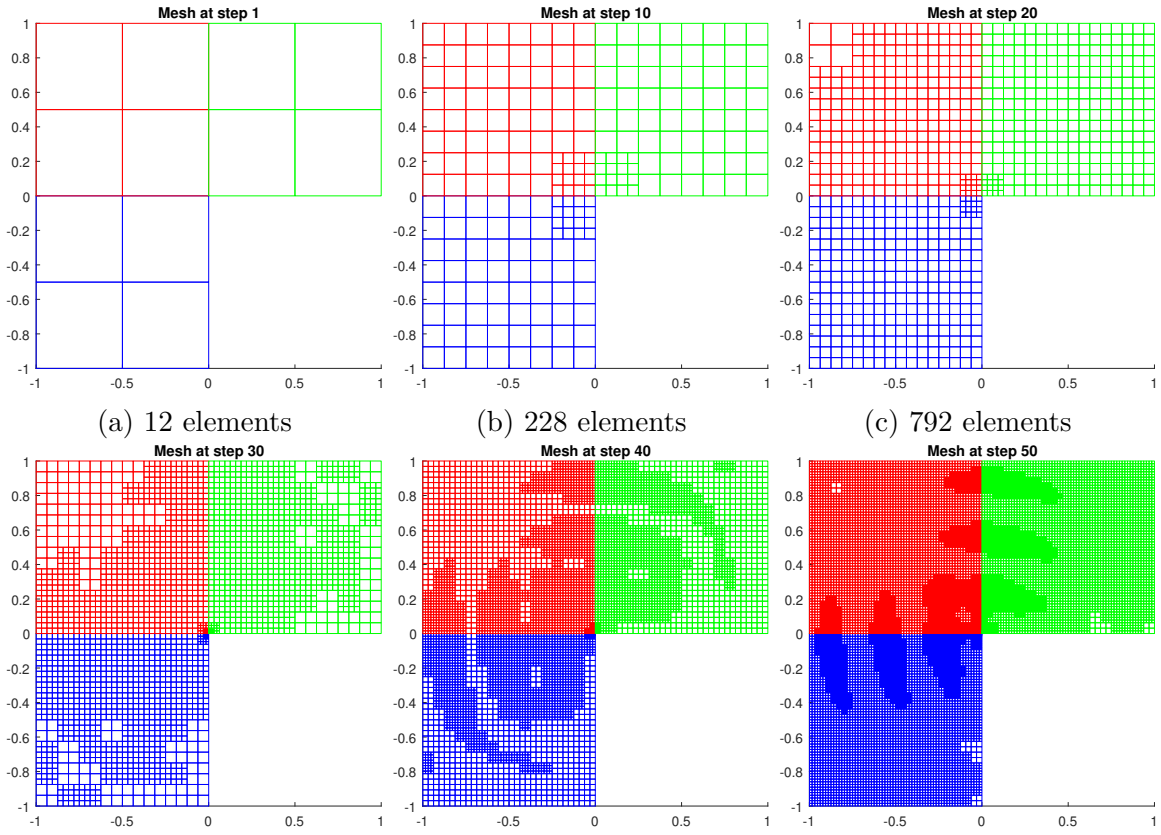

(a) 12 elements (b) 228 elements (c) 792 elements

(d) 2556 elements (e) 7668 elements (f) 20472 elements

Figure 4.3: L-shape problem: Initial and refined meshes obtained by using the recovery-based error estimator. $k = 10$, $\alpha = 2/3$ and $p = 3$

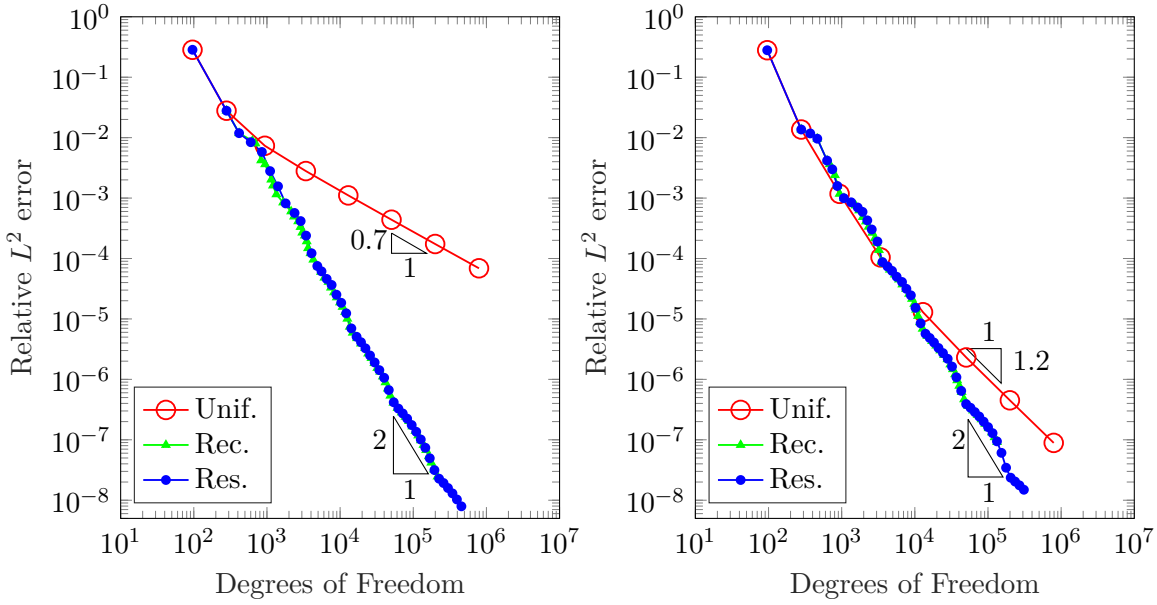

(a) $\alpha = 2/3$ (b) $\alpha = 4/3$

Figure 4.4: L-shape problem: Comparison of different error estimators. Relative error in L^2 norm vs. the number of degree of freedom for $p = 3$, and $k = 10$ using uniform (Unif.) recovery-based (Rec.) and residual-based (Res.) error estimators. Both adaptive strategies improve the error, yielding better convergence rate and quasi-identical results

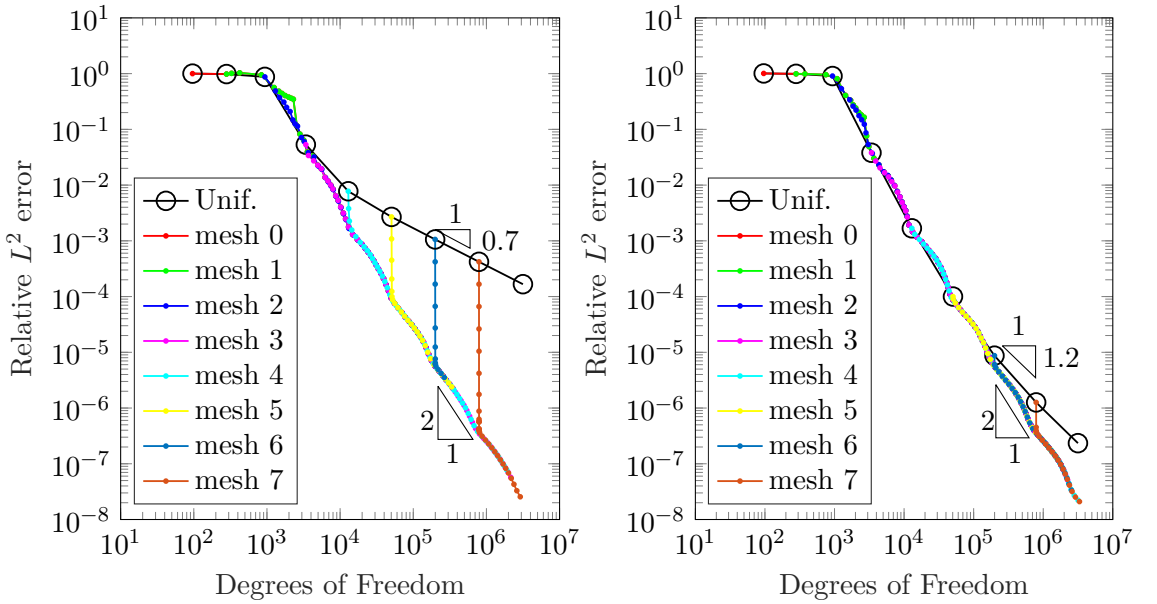

(a) $\alpha = 2/3$ (b) $\alpha = 4/3$

Figure 4.5: L-shape problem: Study of different initial meshes for the recovery-based error estimator. Relative error in L^2 norm vs. the number of degrees of freedom for $p = 3$, and $k = 40$. For all the initial meshes, the error returned by the adaptive refinement converges to the same curve with optimal convergence rate.

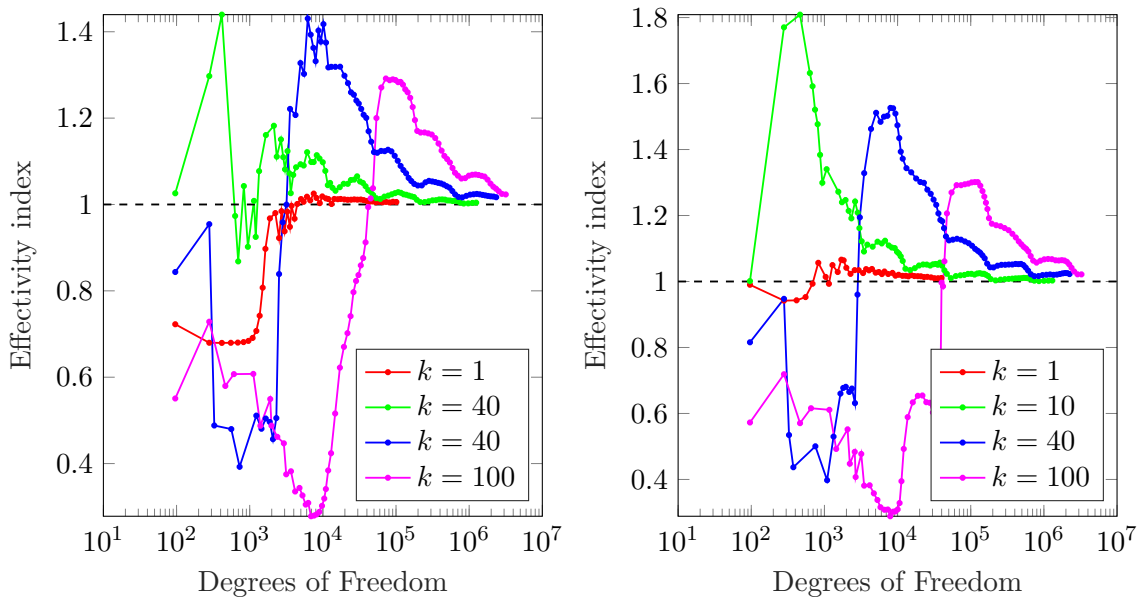

(a) $\alpha = 2/3$ (b) $\alpha = 4/3$

Figure 4.6: L-shape problem: effectivity index for the recovery-based error estimator. Ratio between the recovery-based error estimator and the H^1 semi-norm vs. the number of degrees of freedom for $p = 3$, and different k. In all the cases the ratio between the error estimator and the H^1 semi-norm tends to 1, which means that the estimator is a good approximation of the error

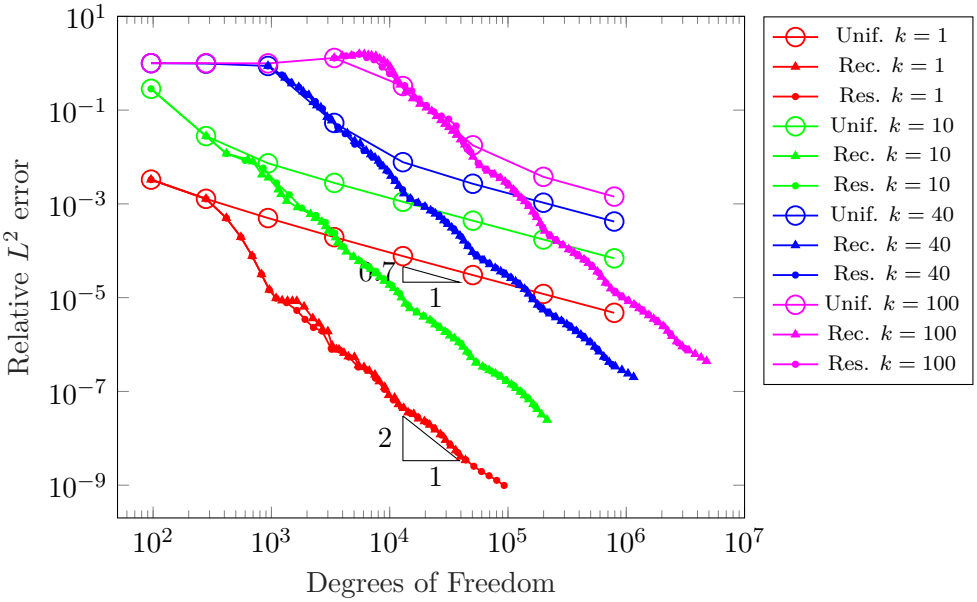

(a) $\alpha = 2/3$

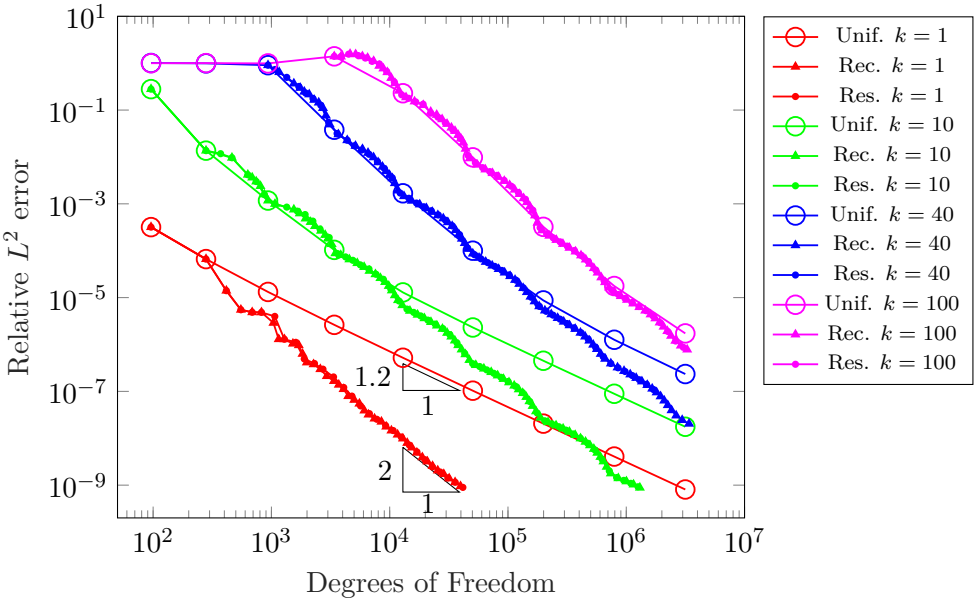

(b) $\alpha = 4/3$

Figure 4.7: L-shape problem: relative error in L^2 norm vs. the number of degree of freedom for $p = 3$ and different k using recovery-based and error-based adaptive and uniform refinements. Unif. stands for uniform refinement, Rec. stands for adaptive refinement using the recovery-based estimator and Res. stands for adaptive refinement using the residual-based error estimator. Both error estimators perform similarly even when the wave number k is increased

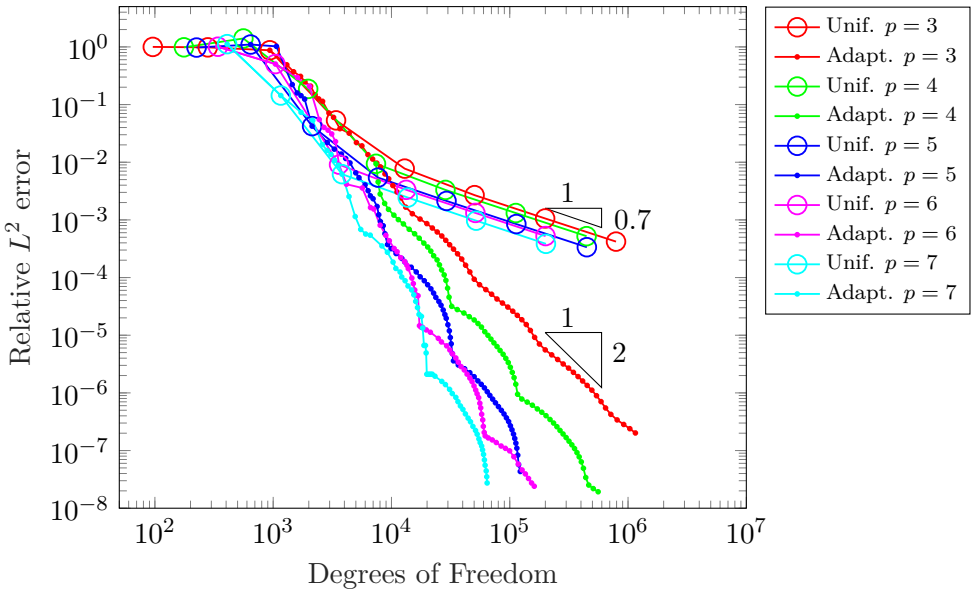

(a) $\alpha = 2/3$

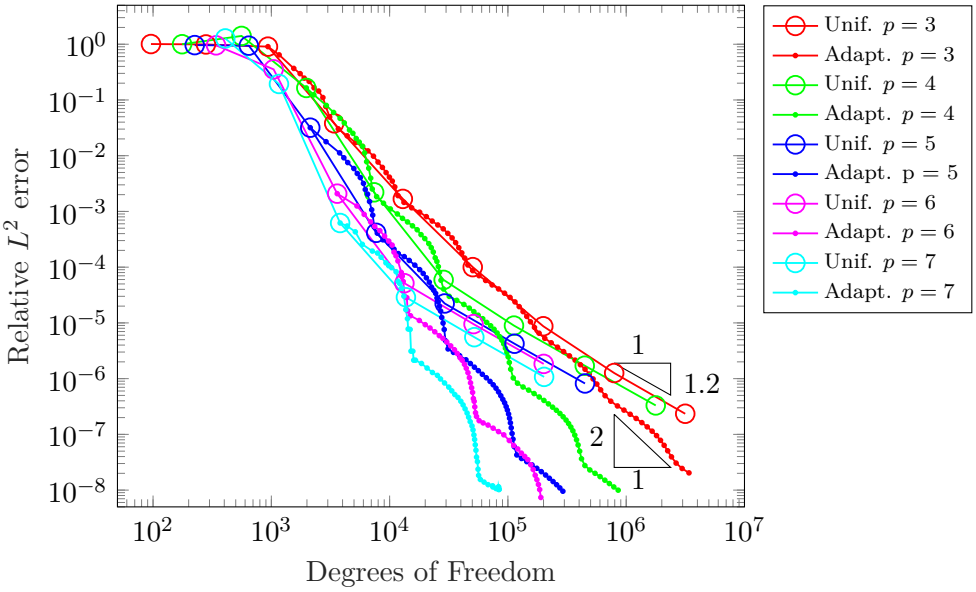

(b) $\alpha = 4/3$

Figure 4.8: L-shape problem: relative error in L^2 norm vs. the number of degree of freedom for $k = 40$ and different values of p using uniform (Unif.) and recovery-based adaptive (Adapt.) refinements. Due to the reduced regularity of the solution, the convergence rate is sub-optimal for all values of $p = 3, 4, 5, 6$ for the uniform refinement, while the adaptive refinement recovers the optimal convergence rate of $(p + 1)/2$

4.1.2 The thin plate example

In this example, we study a thin plate under an oblique plane incident wave, just as in [130]. The geometry consists in a thin plate of dimensions $2L \times 2W$ centered at the origin (denoted as Γ). The scatterer is surrounded by an outer fictitious circular boundary Σ, also centered at the origin and with radius $R_1 = 2$. Therefore, the computational domain Ω is the region bounded by the inner rectangle Γ and the outer circle Σ (Figure 4.9).

The boundary value problems is formulated as follows:

$$\begin{aligned} &\Delta u + k^2 u = 0 && \text{in } \Omega, \\ &\frac{\partial u}{\partial n} = -\frac{\partial u^{inc}(\boldsymbol{x})}{\partial n} && \text{on } \Gamma, \\ &\frac{\partial u}{\partial n} + \left(-ik + \frac{\kappa}{2} - \frac{\kappa^2}{8\,(\kappa - ik)}\right) u - \frac{1}{2\,(\kappa - ik)} \frac{\partial^2 u}{\partial s^2} = 0 && \text{on } \Sigma. \end{aligned} \tag{4.5}$$

Function $u^{inc}(\boldsymbol{x})$ in the first boundary condition corresponds to an incident plane wave, given by

$$u^{inc}(\boldsymbol{x}) = \mathrm{e}^{ik\mathbf{d}\cdot\boldsymbol{x}}, \tag{4.6}$$

where $\mathbf{d}$ is the incident direction $\mathbf{d} = (\cos(\theta^{inc}), \sin(\theta^{inc}))$ and θ^{inc} is the incident angle. In this study we take $\theta^{inc} = 45°$.

The geometry is generated using four symmetrical NURBS patches, as shown in figure 4.10 with control points listed in table A.2.

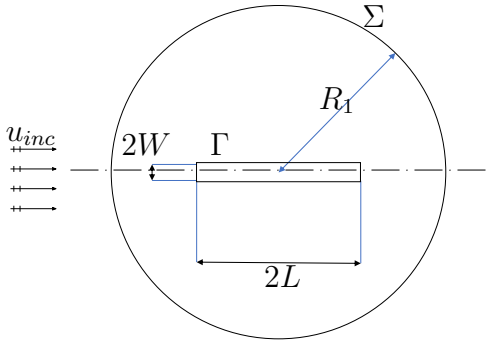

Figure 4.9: The thin plate problem: domain

Figure 4.11 shows the numerical solution for the thin plate problem with inner dimensions $L = 1$ and $W = 0.01$, using $k = 25$ and PHT-splines $p = 3$.

There is no analytical solution available for this problem, so the following convergence plots will be presented in terms of the recovery-based error estimator, which has been probed to be an excellent approximation of the H^1 error norm [39]. In all study cases, the plates are generated using six-patches, except for the case $W = 0$, which was generated using four patches.

Figure 4.12 shows an initial mesh and five different adaptive meshes obtained by the recovery-based adaptive refinement, using $k = 10$ and $p = 3$. In this case the algorithm per-

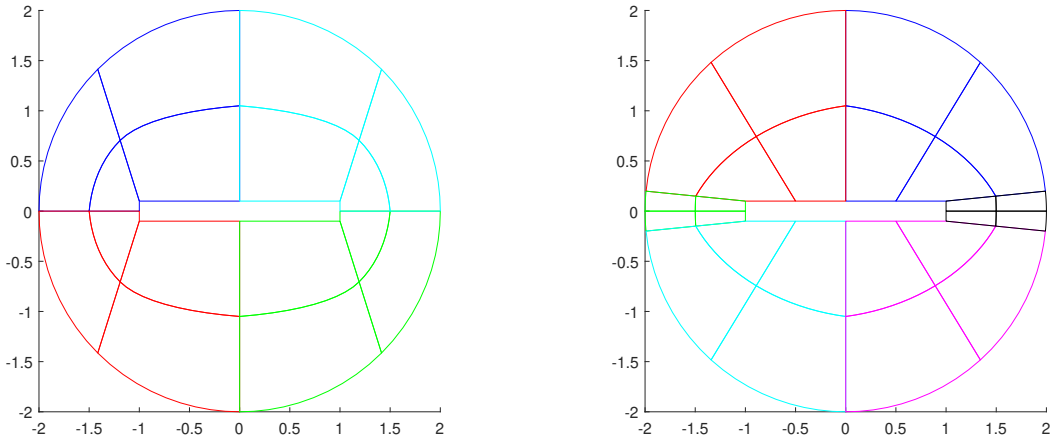

(a) four patches (b) six patches

Figure 4.10: Thin-plate problem: NURBS parameterization using 4 and 6 patches

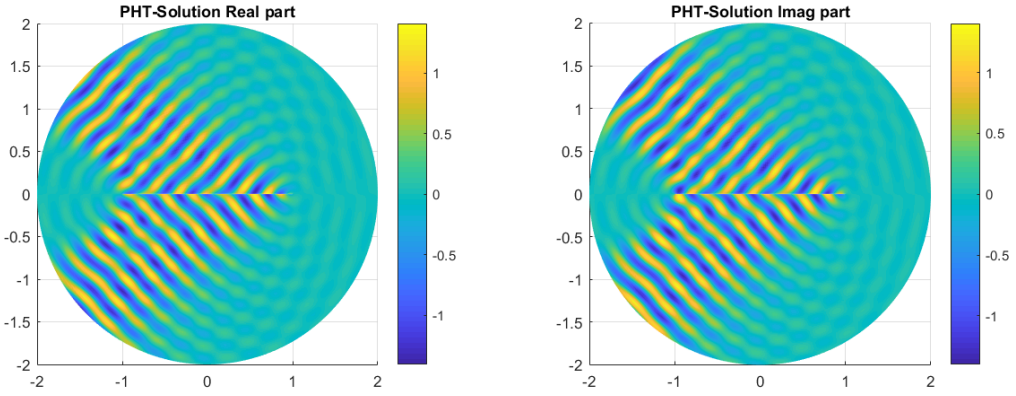

Figure 4.11: The thin plate problem: numerical solution with $k = 25$, $L = 1$ and $W = 0.01$

forms gradient refinement towards the wave direction, with special emphasis on the corners. Similar patters were also observed in all simulations.

Figure 4.13 shows the convergence study for different plate dimensions with $k = 2\pi$ and $p = 3$. In all test cases, adaptive refinement demonstrates a significant advantage in comparison with uniform refinement, returning the optimal convergence rate $p/2$ in the case $W = 0.1$. For the other cases, the convergence rates (1.08 for $W = 0.0001$, 1.02 for $W = 0.001$ and 0.3 for $W = 0$) were superior compared with their respective uniform refinement (0.3, 0.3 and 0.1, respectively), but sub-optimal.

Figure 4.14 shows the convergence studies for different values of the wave parameter k, for two different plates. Figure 4.15 shows the convergence studies in terms of the PHT-Splines degree p and fixed wave parameter $k = 25$, for two different plates.

By comparing the geometry dimensions of the thin plate in figures 4.13, 4.14 and 4.15 ,

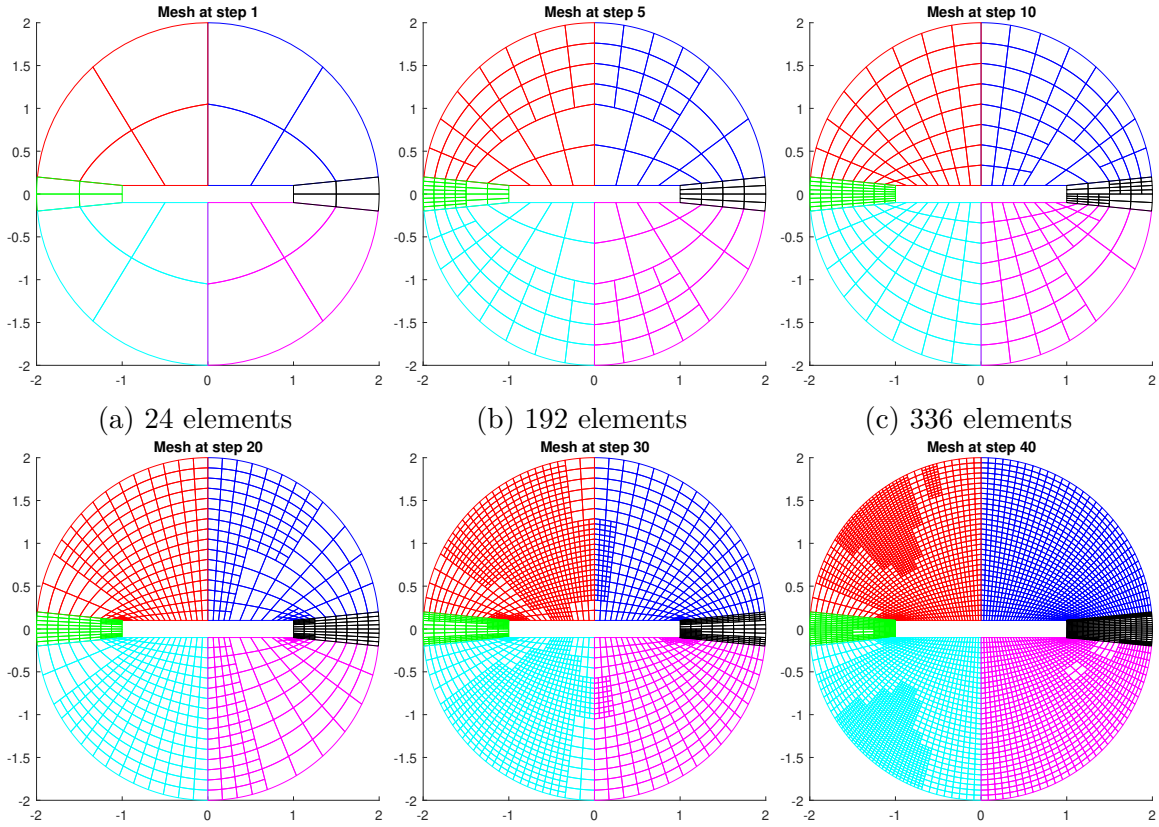

(a) 24 elements (b) 192 elements (c) 336 elements

(d) 984 elements (e) 3240 elements (f) 8484 elements

Figure 4.12: Thin plate problem: Initial and refined meshes obtained by using the recovery-based error estimator. $k = 10$, $L = 1$, $W = 0.2$ and PHT-splines $p = 3$

we can see the effect of the plate geometry on the performance of the adaptive refinement. In the case of the strong singularity with $W = 0$ the improvement in the convergence rate and the overall error is quite insignificant. But for all study cases with $W > 0$ adaptive algorithms yield optimal or close to optimal convergence rate. Even for very thin plates adaptive algorithms are able to efficiently capture the behavior of the solutions around the corners for all values of p and k considered in this study. Note, however, that the adaptive refinement outperforms the uniform refinement only after the pre-asymptotic range is reached, i.e. the size of the biggest elements satisfies the condition $kh/p < 1$.

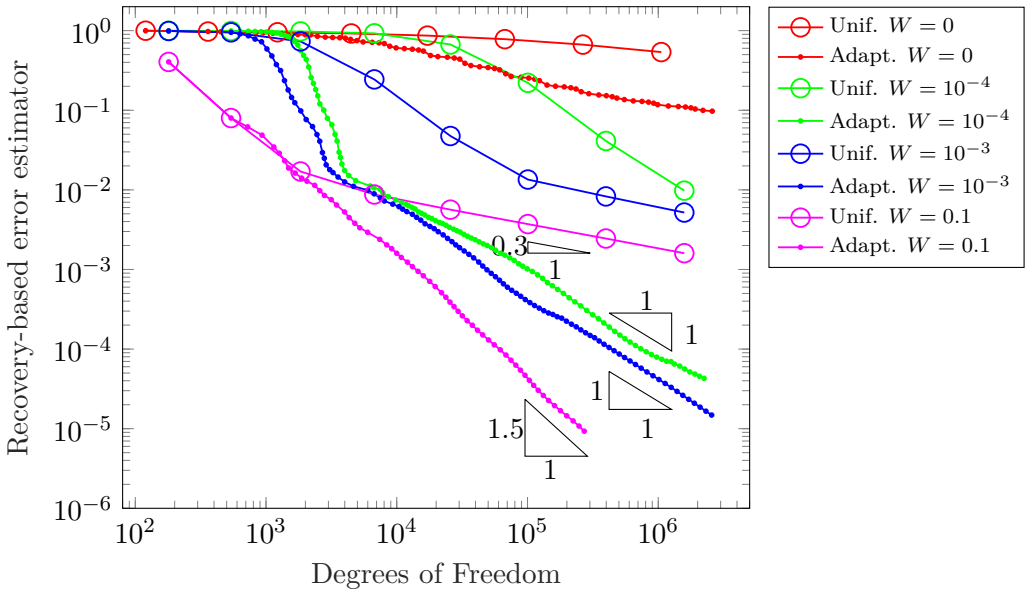

Figure 4.13: Thin-plate problem: recovery error estimator in H^1 norm vs. the number of degree of freedom for $p = 3$ and different thickness for the thin plate ($k = 2\pi$, $L = 1$)

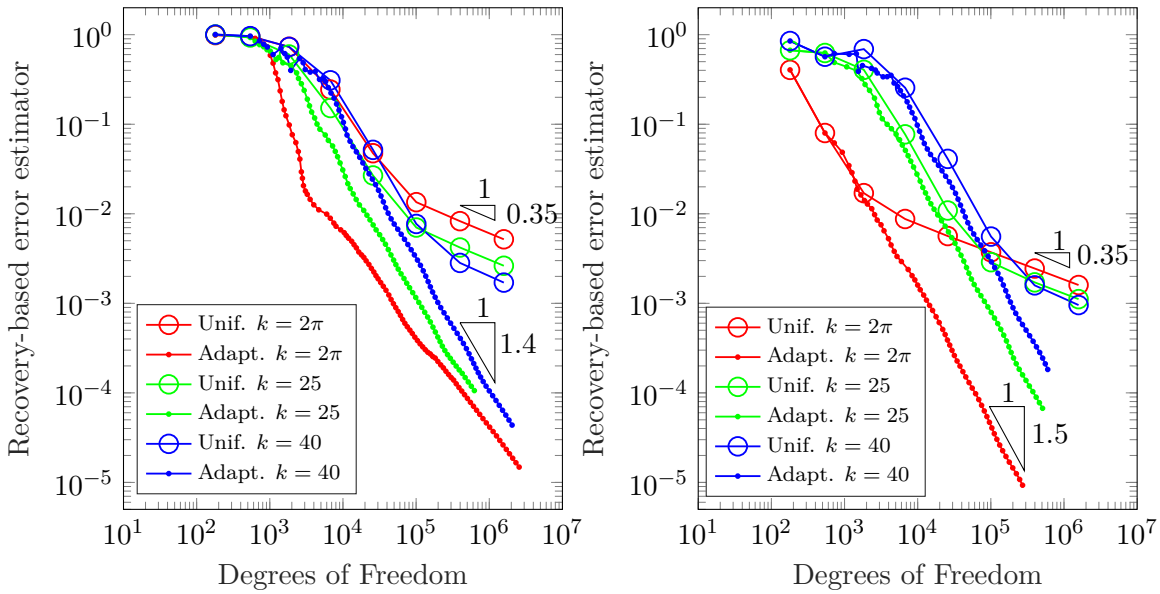

(a) $L = 1$, $W = 0.001$ (b) $L = 1$, $W = 0.1$

Figure 4.14: Thin-plate problem: recovery error estimator in H^1 norm vs. the number of degree of freedom for different k ($p = 3$)

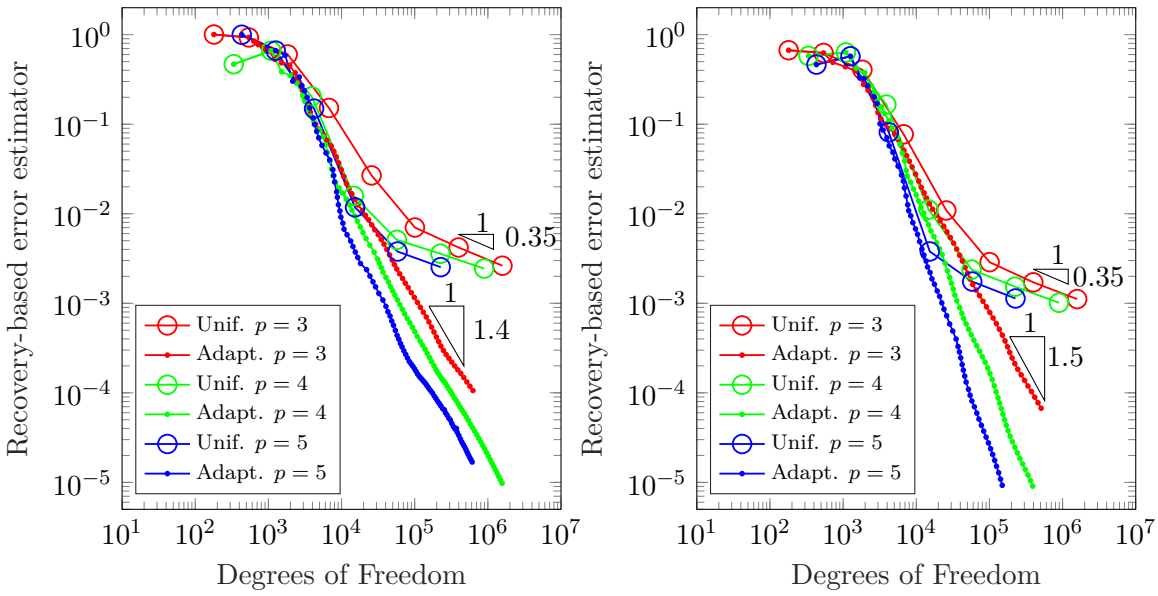

(a) $L = 1$, $W = 0.001$ (b) $L = 1$, $W = 0.1$

Figure 4.15: Thin-plate problem: recovery error estimator in H^1 norm vs. the number of degree of freedom for $k = 25$ and different PHT-Splines degrees p

4.1.3 The star-shaped geometry

In this problem we study a star-shaped scatterer (Figure 4.16) with a plane wave, given by equation (4.6), propagating in direction $\theta^{inc} = 0°$.

On the outer boundary, the BGT2 condition is imposed, so the full boundary value problem is given by eq. (4.5).

The geometry is generated using five patches, as shown in Figure 4.16. Table A.3 shows the knot vector and control points employed for the NURBS parameterization of each patch.

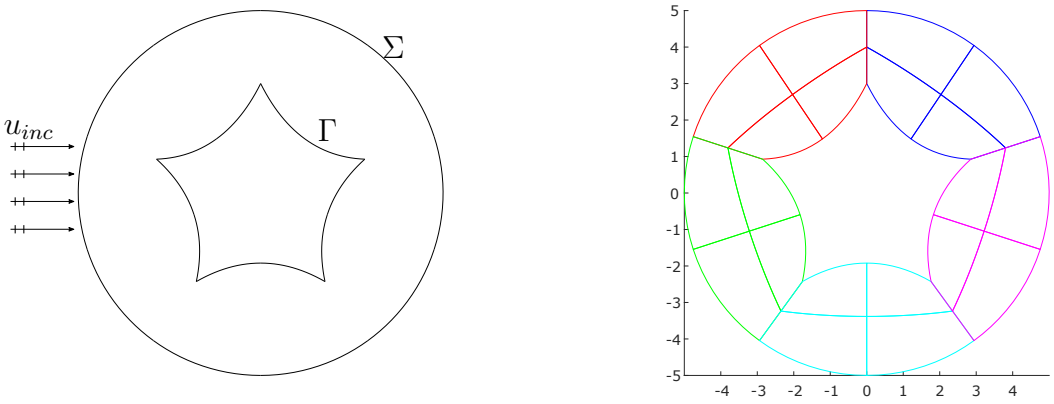

(a) Problem domain.

(b) NURBS patches.

Figure 4.16: Star-shaped problem: Domain and NURBS parameterization

Figure 4.17 shows the numerical solution for the real and imaginary part, taking $k = 10$. Since the analytical solution for this problem is not available, we present the results in terms of the recovery-based error estimator as an error estimator for the H^1 error semi-norm.

Figure 4.18 shows an initial mesh and five different adaptive meshes obtained by the recovery-based adaptive refinement, using $k = 10$ and $p = 3$. As in the thin plate example, the algorithm performs gradient refinement both towards the wave direction ($\theta^{inc} = 0°$) and the corners of the star. Similar patters were also observed in all simulations.

Figure 4.19a shows the convergence study for different k values, fixing the PHT-Splines degree $p = 3$. Figure 4.19b shows the convergence study for different PHT-Splines degrees p, fixing $k = 25$.

The results show again the superiority of the recovery-based adaptive refinement over the uniform refinement, leading to the optimal convergence rate for both different wavenumber k and different PHT-splines degrees p in the pre-asymptotic range.

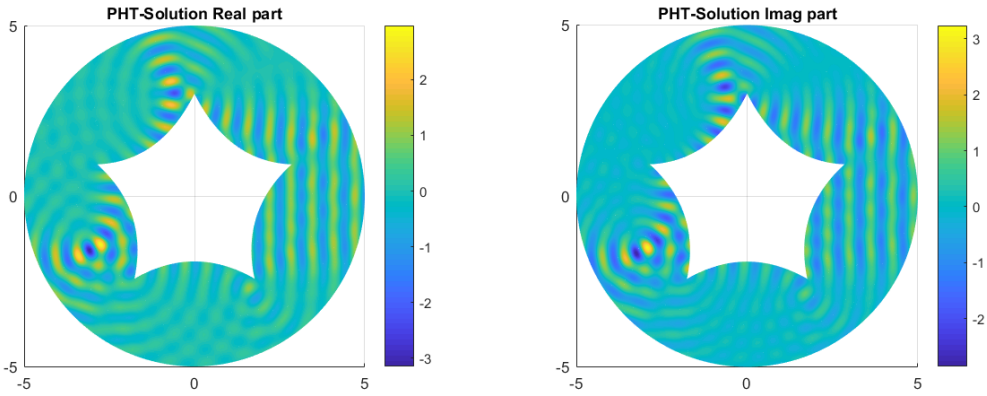

Figure 4.17: Star-shaped problem: numerical solution for $k = 10$

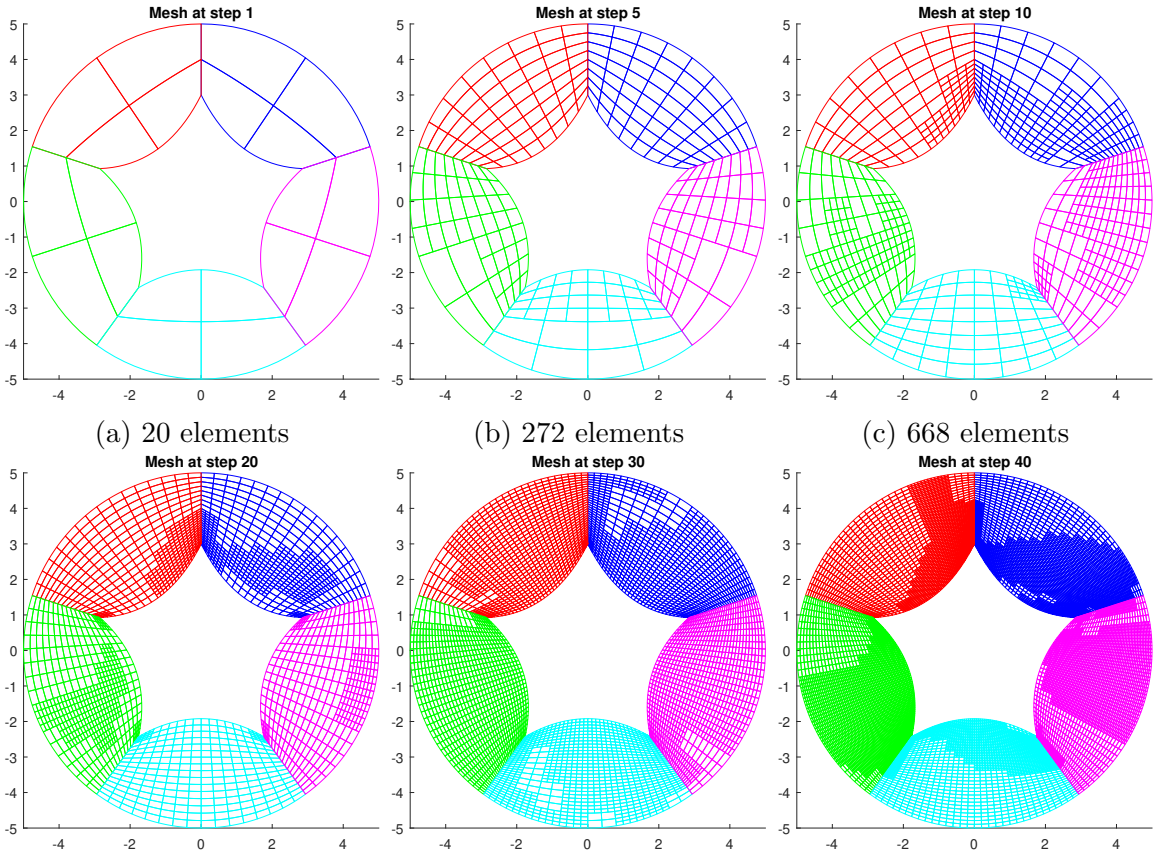

(a) 20 elements (b) 272 elements (c) 668 elements

(d) 2108 elements (e) 4976 elements (f) 14504 elements

Figure 4.18: Star-shaped problem: Initial and refined meshes obtained by using the recovery-based error estimator. $k = 10$ and $p = 3$

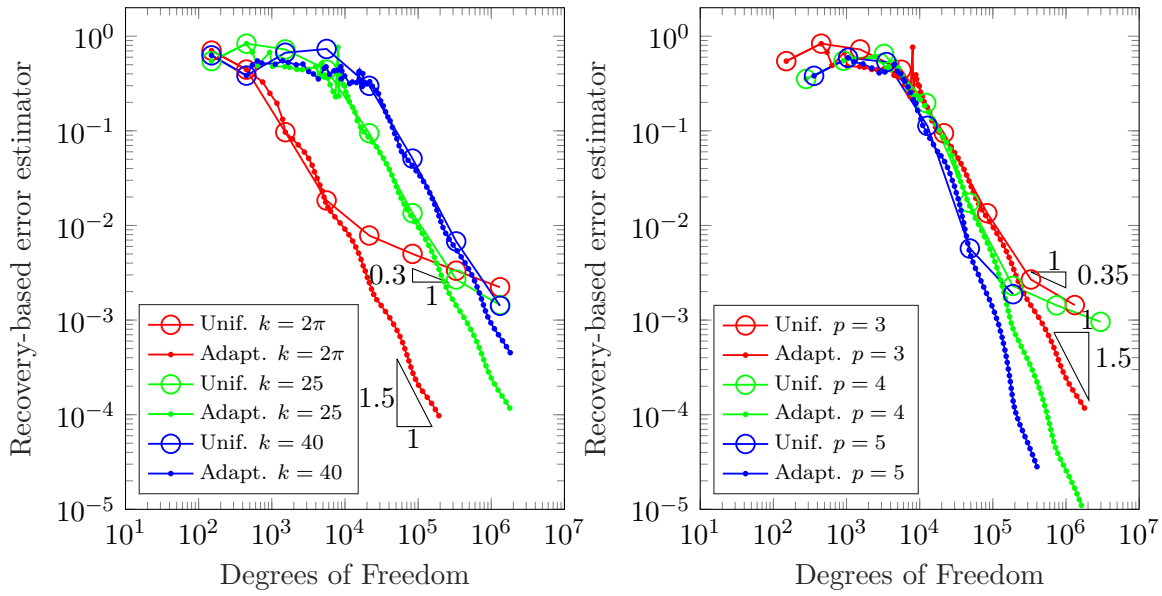

(a) k study, $p = 3$ (b) p study, $k = 25$

Figure 4.19: Star-shaped scatterer: k and p study. Recovery-based error estimator in H^1 semi-norm vs. the number of degrees of freedom

4.2 3D Numerical Examples

4.2.1 The unit cube problem

Consider the unitary cube $\Omega = [0,1] \times [0,1] \times [0,1]$ (Figure 4.20) with boundaries $\Gamma_D = \{(x,y,z) \in \Omega \mid y = 0, (x,z) \in [0,1] \times [0,1]\}$ and $\Gamma_R = \partial\Omega \setminus \Gamma_D$. We consider the following boundary value problem:

$$\begin{aligned} \Delta u + k^2 u &= 0 && \text{in } \Omega, \\ u &= 0 && \text{on } \Gamma_D, \\ \frac{\partial u}{\partial n} + iku &= g + ikg && \text{on } \Gamma_R. \end{aligned} \tag{4.7}$$

where g is the exact solution given by:

$$u^{\text{exact}}(r,\theta,z) = g(r,\theta,z) = J_\alpha(\sqrt{k^2+n^2}r)\sin(\alpha\theta)\,\mathrm{e}^{-nz} \tag{4.8}$$

where (r,θ,z) are 3D cylindrical coordinates and n is an integer.

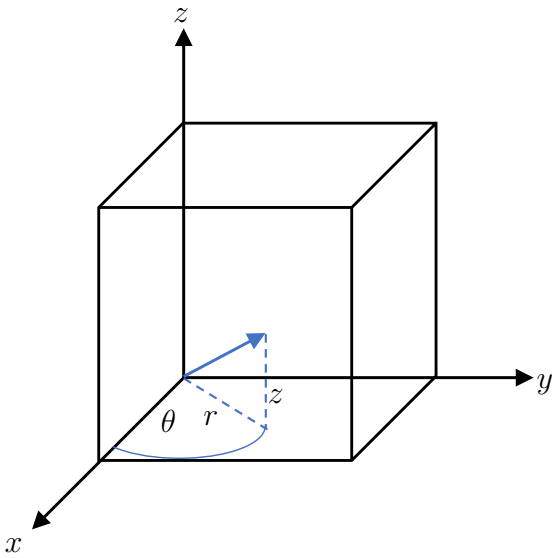

Figure 4.20: The unit cube problem: domain

The geometry is generated using 1 patch NURBS (Table A.4).

Figure 4.21 shows the numerical solution for the real part, taking $k = 10$, $\alpha = 2/3$ and $n = 1$, while figure 4.22 shows the respective initial mesh and five different adaptive meshes obtained by the recovery-based adaptive refinement. In this example, a weak singularity in the first derivative of the analytical solution is given by the Bessel function $J_\alpha(x)$ with $\alpha = 2/3$, and analogously to the L-shaped example, the second order derivative is singular at $r = 0$ with $\alpha = 4/3$. The algorithm performs gradient refinement towards the singular edge. Similar patters were also observed in all simulations.

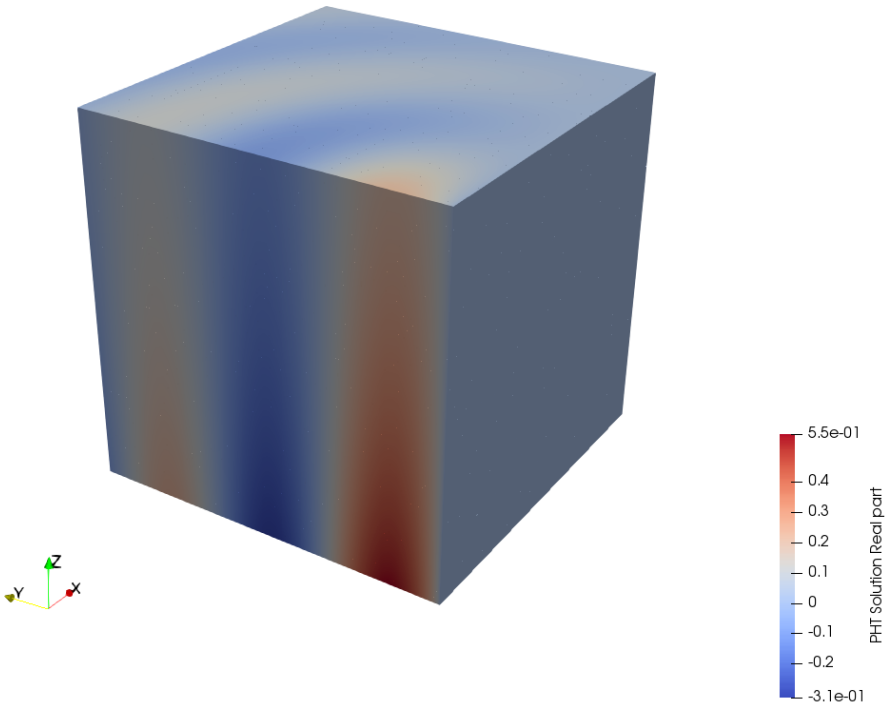

Figure 4.21: The unit cube problem: numerical solution for $k = 10$ and $n = 1$

Figure 4.23 shows the L^2 error plot using uniform, residual-based and recovery-based adaptive refinement, for different real values of k ($n = 1$). Both adaptive refinement algorithms are capable of improving the convergence rate of the uniform refinement, yielding the convergence rate slightly less than the optimal value of $(p + 1)/3$. It is also worth to notice that in the case $\alpha = 2/3$ the residual-based algorithm slightly outperforms the recovery-based one, leading to smaller error for the same number of DOF's, while in the case $\alpha = 4/3$ both error estimators yield quasi-optimal results.

Figure 4.24 shows the H^1 error semi-norm using uniform, residual-based and recovery-based adaptive refinement, for different real values of k ($n = 1$). Again, both adaptive refinement algorithms are capable of improving the convergence rate of the uniform refinement, but for $\alpha = 2/3$ the convergence rate is less than the optimal value of $p/3$, while in the case $\alpha = 4/3$ both error estimators yield quasi-optimal results.

Figures 4.25 and 4.26 show the L^2 error norm and H^1 error semi-norm plots, respectively, using both regular and residual-based adaptive refinement, for different values of p ($n = 1$ and $k = 10$). In both cases, the convergence rate for the uniform refinement is determined by the order of singularity and therefore is the same for all values of p. For the adaptive refinement, the convergence rate is clearly superior compared to the uniform one. However, it is interesting to notice, that in the case $\alpha = 2/3$ the convergence rate of the adaptive algorithm also does not depend on the value of p.

Finally, Figure 4.27 shows the effectivity index plot of the recovery-based error estimator

for both $\alpha = 2/3$ and $\alpha = 4/3$ with $p = 3$ and $n = 1$. It can be seen that for $\alpha = 4/3$ the effectivity index tends to 1, which means that the error estimator tends to the actual error, while for $\alpha = 2/3$ the effectivity index tends to 0.7.

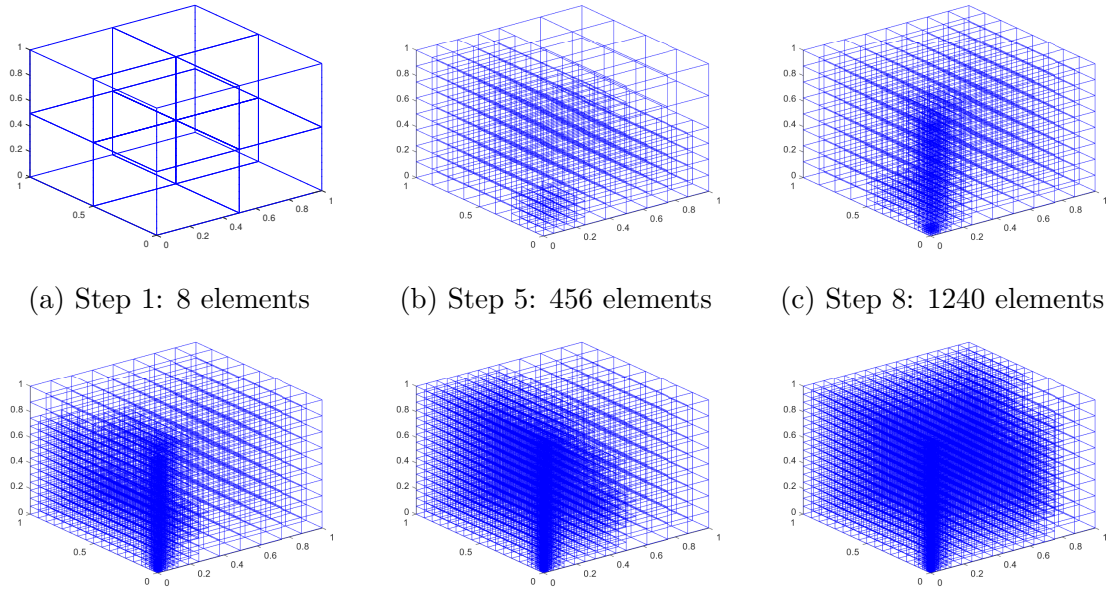

(a) Step 1: 8 elements (b) Step 5: 456 elements (c) Step 8: 1240 elements

(d) Step 10: 2864 elements (e) Step 12: 5272 elements (f) Step 15: 11712 elements

Figure 4.22: The unit cube problem: initial and refined meshes for $k = 10$

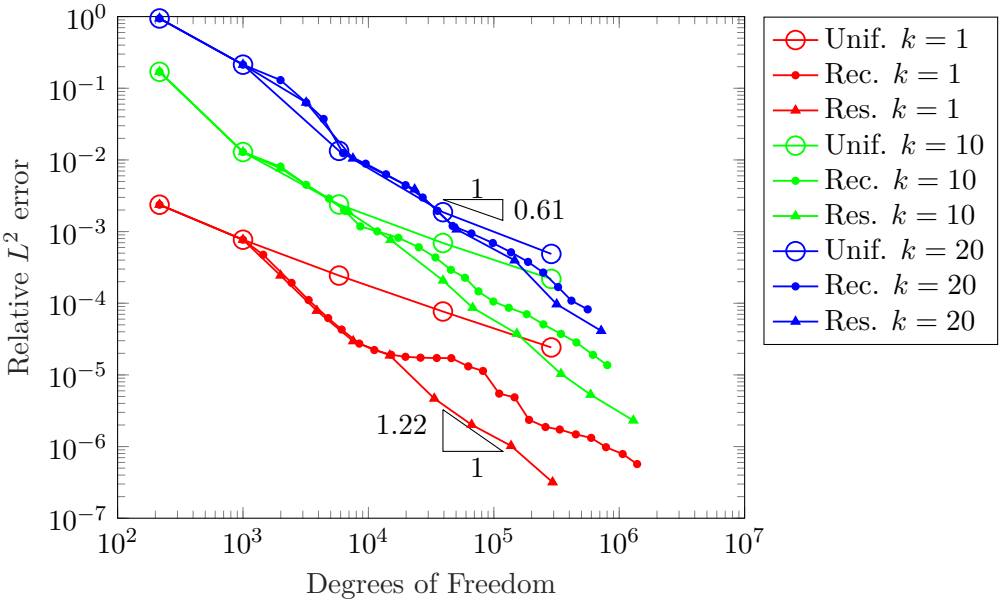

(a) $\alpha = 2/3$

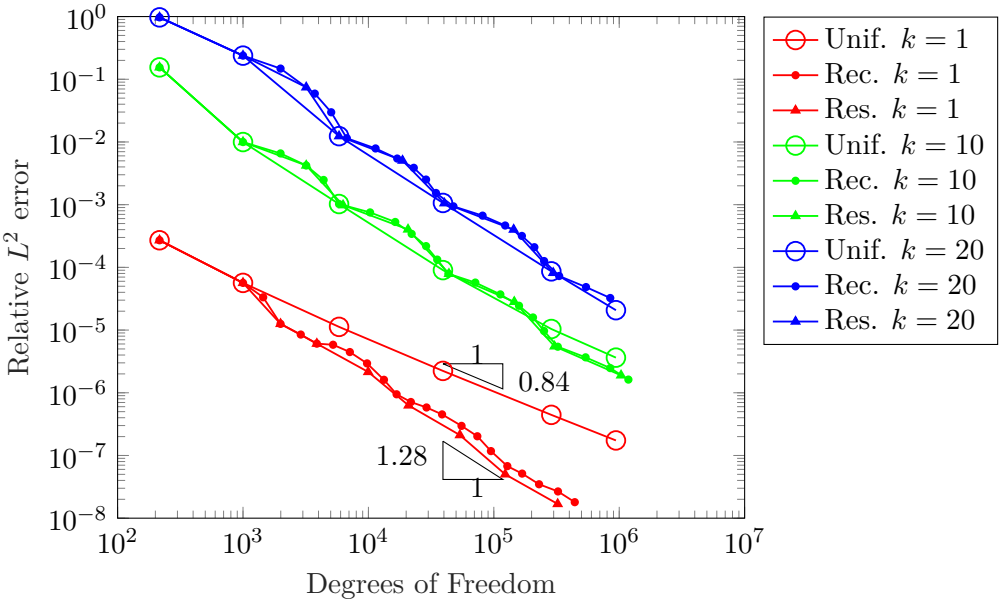

(b) $\alpha = 4/3$

Figure 4.23: The unit cube problem: relative error in L^2 norm vs. the number of degree of freedom for $p = 3$ and different k using recovery-based and error-based adaptive and uniform refinements. Unif. stands for uniform refinement, Rec. stands for adaptive refinement using the recovery-based estimator and Res. stands for adaptive refinement using the residual-based error estimator

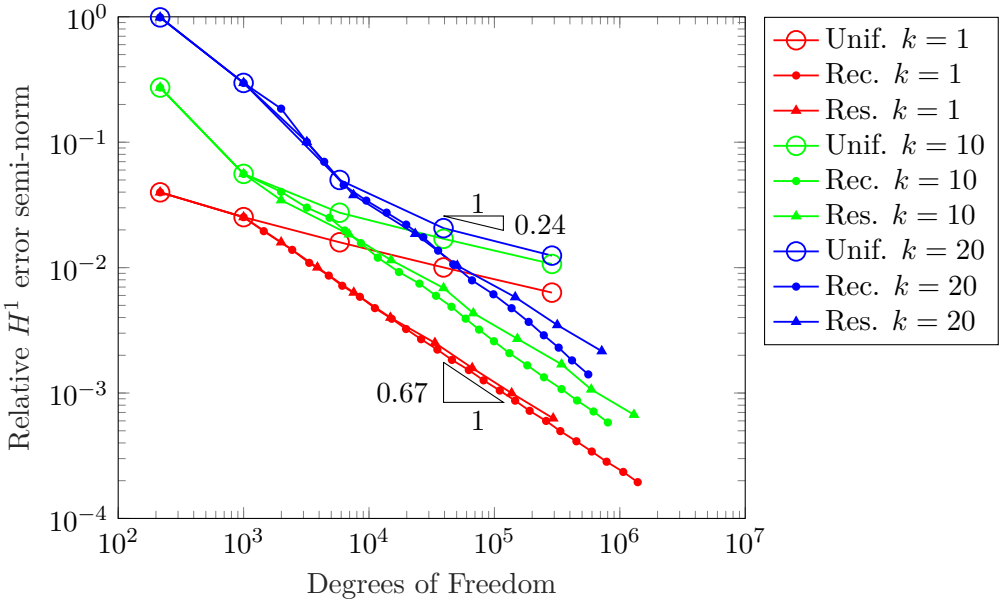

(a) $\alpha = 2/3$

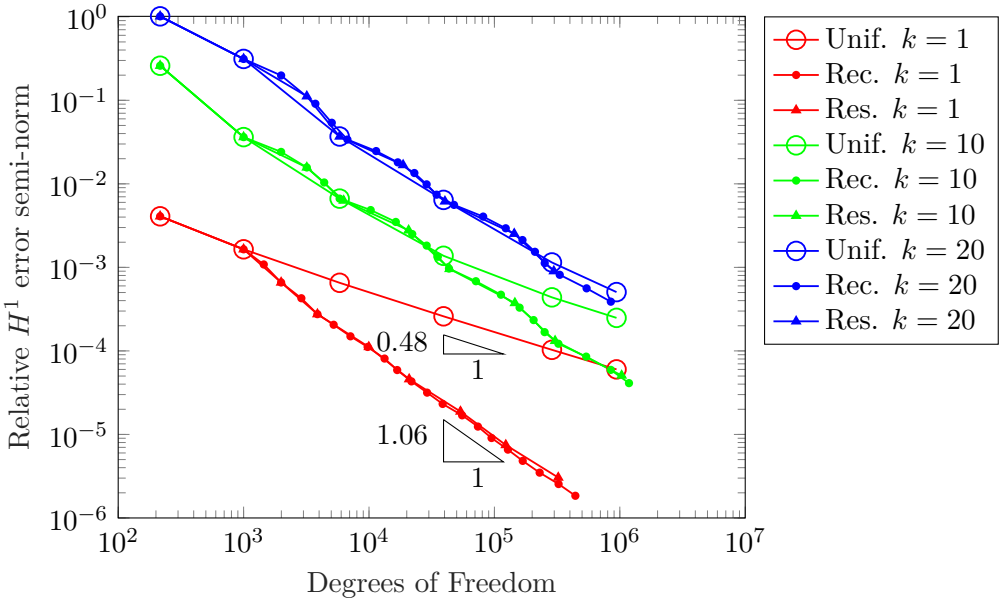

(b) $\alpha = 4/3$

Figure 4.24: The unit cube problem: relative error in H^1 semi-norm vs. the number of degree of freedom for $p = 3$ and different k using recovery-based and error-based adaptive and uniform refinements. Unif. stands for uniform refinement, Rec. stands for adaptive refinement using the recovery-based estimator and Res. stands for adaptive refinement using the residual-based error estimator

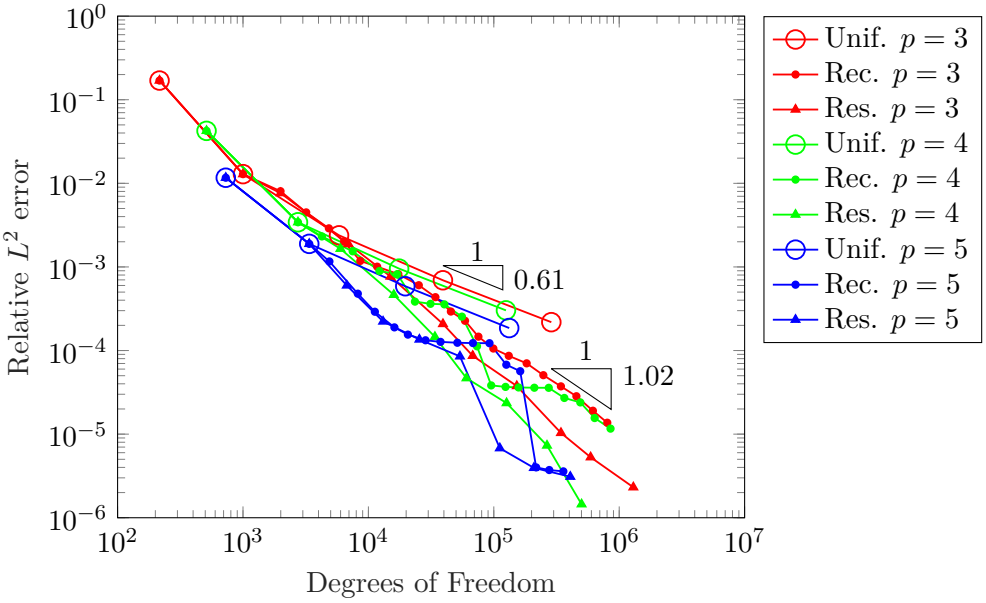

(a) $\alpha = 2/3$

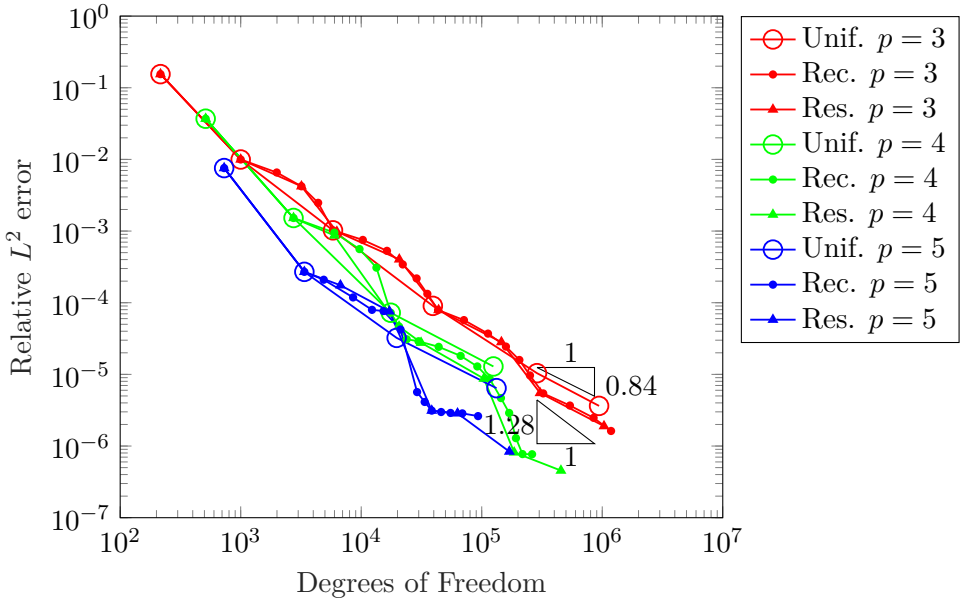

(b) $\alpha = 4/3$

Figure 4.25: The unit cube problem: relative error in L^2 norm vs. the number of degree of freedom for $k = 10$ and different values of p using uniform (Unif.), recovery-based adaptive (Rec.) and residual-based adaptive (Res.) refinements

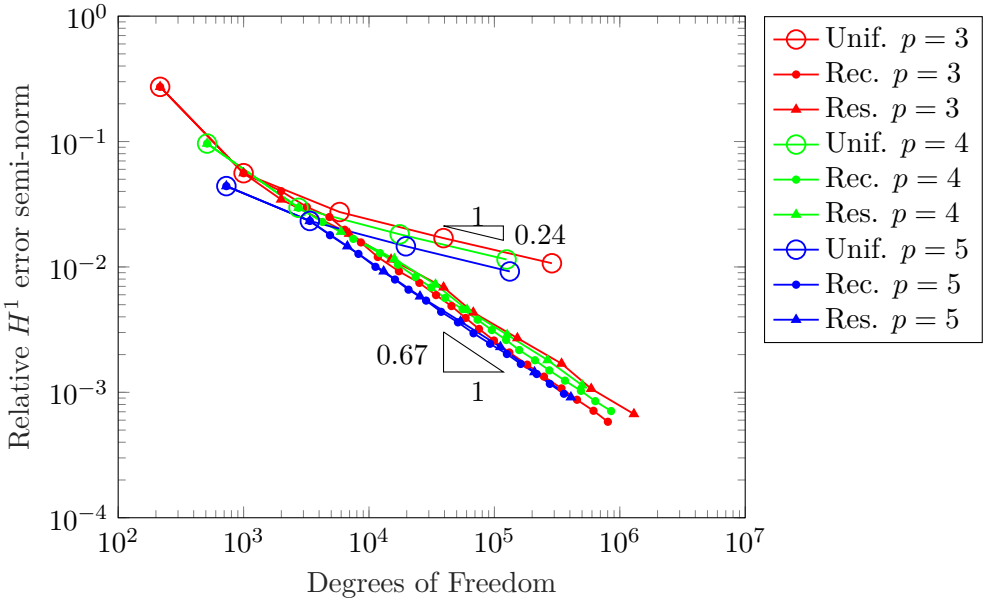

(a) $\alpha = 2/3$

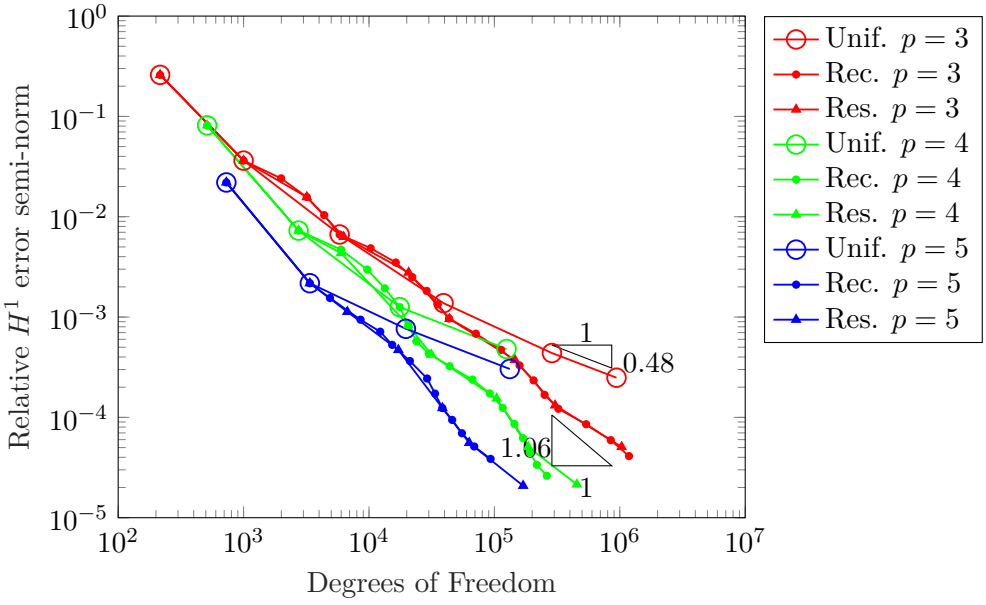

(b) $\alpha = 4/3$

Figure 4.26: The unit cube problem: relative error in H^1 semi-norm vs. the number of degree of freedom for $k = 10$ and different values of p using uniform (Unif.), recovery-based adaptive (Rec.) and residual-based adaptive (Res.) refinements

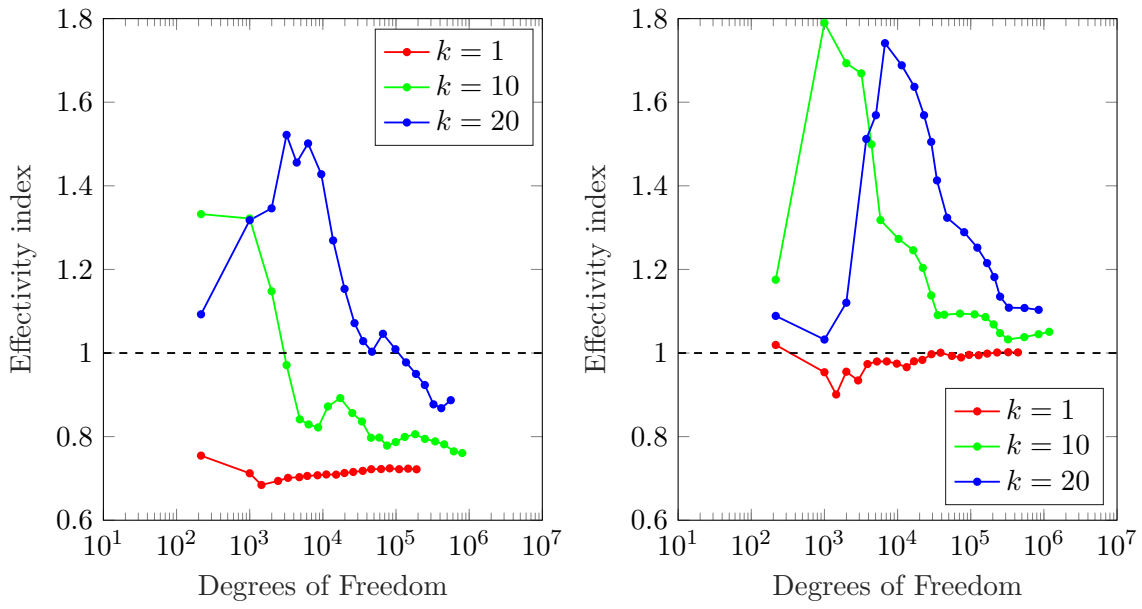

(a) $\alpha = 2/3$ (b) $\alpha = 4/3$

Figure 4.27: The unit cube problem: effectivity index for the recovery-based error estimator. Ratio between the recovery-based error estimator and the H^1 semi-norm vs. the number of degrees of freedom for $p = 3$, and different k

Chapter 5

Numerical Results: Fracture Mechanics of Kirchhoff-Love plates

5.1 Numerical Examples: Bending of plates with cracks

In this section, we present several numerical examples concerned with different static and dynamic behavior of Kirchhoff-Love plates with cracks.

For problems with known analytical solutions, we use the following relative H^2 semi-norm of the error:

$$\frac{\|u-u_h\|_{H^2}}{\|u\|_{H^2}} = \sqrt{\frac{\int_\Omega \left(m(u)-m(u_h)\right)^T D^{-1}\left(m(u)-m(u_h)\right)\mathrm{d}\Omega}{\int_\Omega \left(m(u)\right)^T D^{-1}\left(m(u)\right)\mathrm{d}\Omega}} \tag{5.1}$$

5.1.1 Square plate with an edge crack

In this first numerical example, we solve the problem of a plate with an edge crack of length a under non-homogeneous Dirichlet boundary conditions given by pure mode k_2:

$$u^{\text{exact}} = \frac{(2r)^{3/2}}{2Eh}\frac{(1-\nu^2)}{(3+\nu)}\left[\frac{3\nu+5}{3(\nu-1)}\sin\left(\frac{3\theta}{2}\right)-\sin\left(\frac{\theta}{2}\right)\right] \tag{5.2}$$

This problem is also solved in [102]. The non-homogeneous boundary conditions are imposed using Nitsche's approach [131, 132], and both crack faces are moment and traction free.

The plate dimensions are: length $L = 1$, width $H = 1$, thickness $h = 0.09$ and crack length $a = 0.5$; while the material properties are: Young's Modulus $E = 14.98$[kPa], Poisson's ratio $\nu = 0.3$.

Figure 5.1 shows the numerical vertical displacement obtained using PHT-splines of degree

$p = q = 4$ with adaptive refinement.

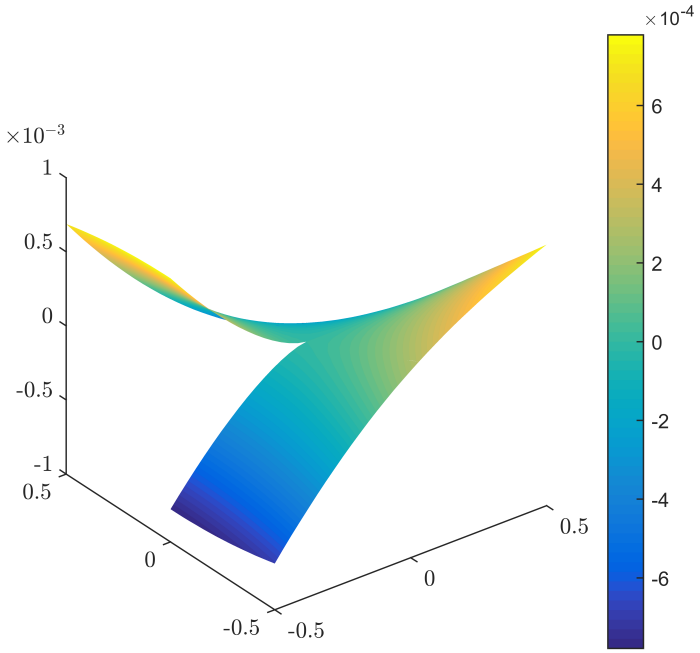

Figure 5.1: Deformation of the infinite plate with a straight crack

Figure 5.2 shows the initial mesh and five different states of the adaptive refinement obtained using the recovery-based error estimator criteria. In these figures, we can see that the refinement process is centered around the tip of the crack. Similar patterns were observed in all simulations.

To impose the non-homogeneous Dirichlet boundary condition with Nitsche's method, we employed the stabilization parameters shown in Table 5.1 for three different PHT-splines degrees. Figure 5.3 shows the convergence rate in the relative L^2 error norm on the boundary for $p = 3, 4, 5$. The convergence rates obtained are similar to the optimal ones $(p + 1)$, so we can conclude that the Nitsche's method is capable of imposing the boundary conditions reliably.

Degree	Stabilization Parameters		
$p = q$	α_Θ	α_W	α_C
3	10^7	10^9	0
4	10^7	10^{11}	0
5	10^7	10^{11}	0

Table 5.1: Values of the stabilization parameters use on the Nitsche's Method

Figure 5.4 shows a comparison between uniform refinement and different percentages (α) of refinement for the adaptive refinement. Different percentages of refinement leads to similar slope, while taking smaller percentages leads to smaller error, making the refinement process

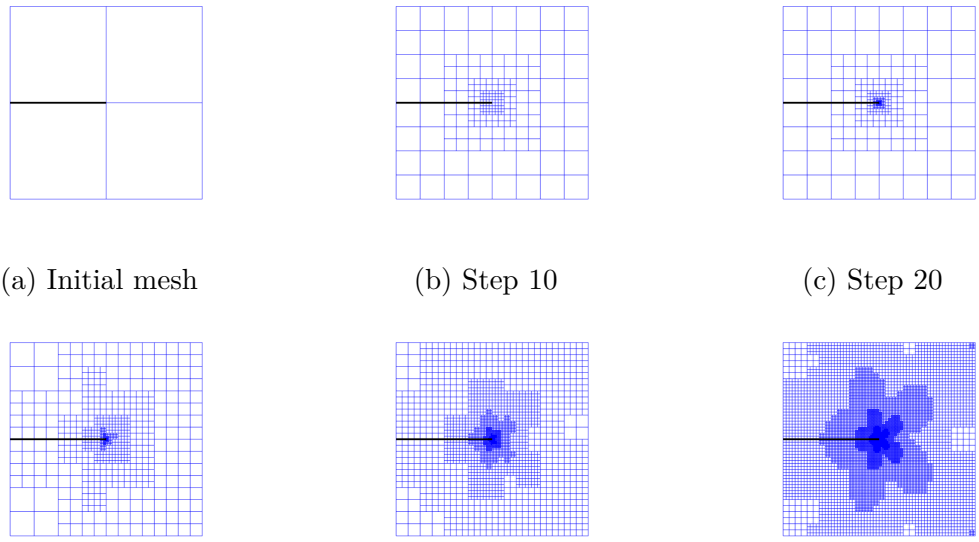

(a) Initial mesh (b) Step 10 (c) Step 20

(d) Step 25 (e) Step 30 (f) Step 35

Figure 5.2: Initial and five refined meshes for the square plate with an edge crack. ($p = 3$). The black line represents the crack

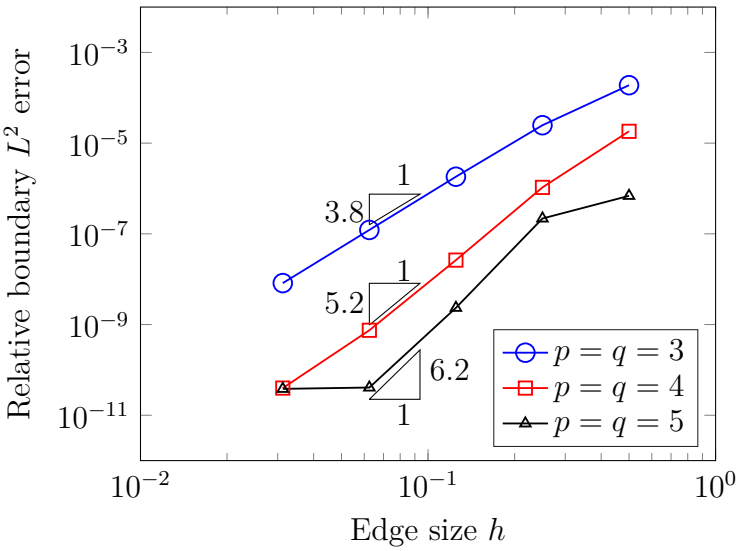

Figure 5.3: Square plate with an edge crack: convergence of the boundary condition imposed by Nitsche's Method

more efficient. Figure 5.5 shows the effectivity index (which is defined as the ratio between the error estimator and the error itself) computed for the uniform and recovery-based adaptive refinement for $p = 3$. It can be concluded that the smaller the α lead to a faster convergence to 1, which means that the error estimator tend to the H^2 error semi-norm. For the following examples we choose $\alpha = 75\%$, since it leads to a good balance between computational cost and reliability in the error estimator.

Figure 5.6 shows the convergence plot in relative H^2 error semi-norm (eq. (5.1)) and the

recovery-based error estimator given by eq. (3.110) for PHT-splines of degree $p = q = 3, 4, 5$ using $\alpha = 75\%$. In all cases, the convergence rate observed for the adaptive refinement is significantly higher than their corresponding uniform refinement.

Finally, Table 5.2 shows the stress intensity factor k_2 computed using the domain integral method (eq. (3.105)) with different inner radius r_d for the domain integral. Both uniform and adaptive refinement results are presented, for $p = 3, 4, 5$. Uniform and adaptive refinement lead to similar results, with the adaptive refinement being significantly smaller in terms of DOF.

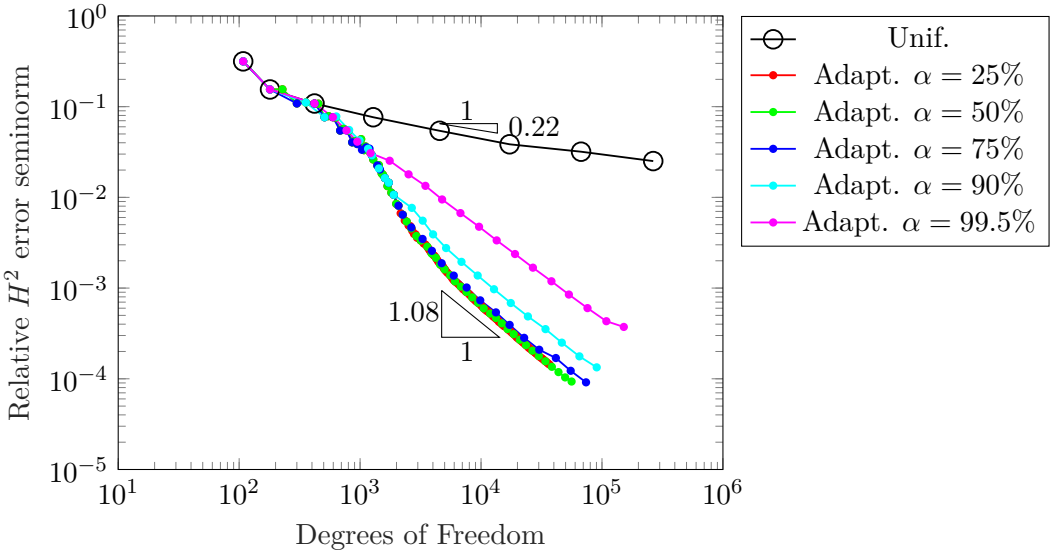

Figure 5.4: Square plate with an edge crack: Study of different α parameters for the recovery-based error estimator. Relative error in H^2 semi-norm vs. the number of degrees of freedom for $p = 3$

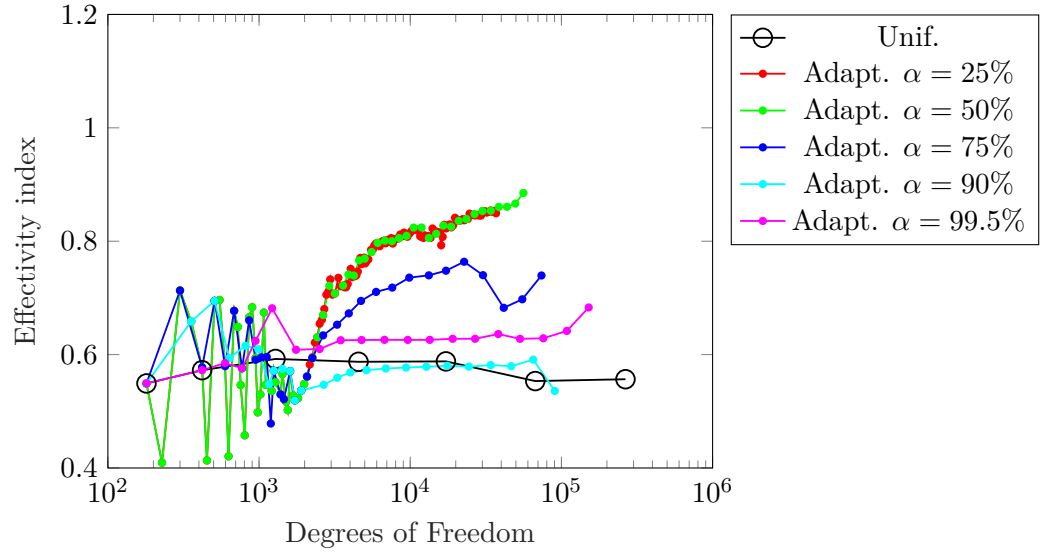

Figure 5.5: Square plate with an edge crack: Study of different α parameters for the recovery-based error estimator. Effectivity index vs. the number of degrees of freedom for $p = 3$

		k_2				
$p = q$		$r_{\mathrm{d}_{shrinking}}$	$r_{\mathrm{d}} = 0.1$	$r_{\mathrm{d}} = 0.2$	$r_{\mathrm{d}} = 0.3$	$r_{\mathrm{d}} = 0.4$
3	Uniform (4548 DOF)	1.012	0.998	0.994	0.978	0.977
	Adaptive (1338 DOF)	0.998	0.996	0.996	1.089	0.996
4	Uniform (9944 DOF)	1.011	0.997	0.993	0.978	0.977
	Adaptive (1874 DOF)	1.001	0.997	0.996	1.088	0.995
5	Uniform (10233 DOF)	1.019	0.962	1.001	0.975	0.983
	Adaptive (2331 DOF)	1.000	0.997	0.997	1.088	0.994

Table 5.2: Square plate with an edge crack: stress intensity factor $k2$ computed by interaction integral using different r_{d} radius. Exact value is $k_2 = 1$

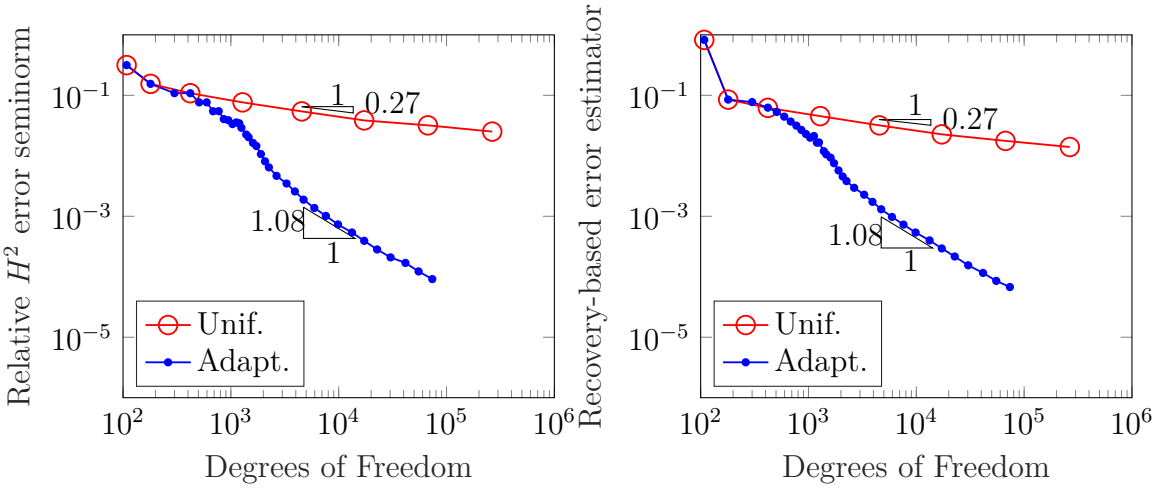

(a) $p = q = 3$, H^2 semi-norm

(b) $p = q = 3$, error estimator

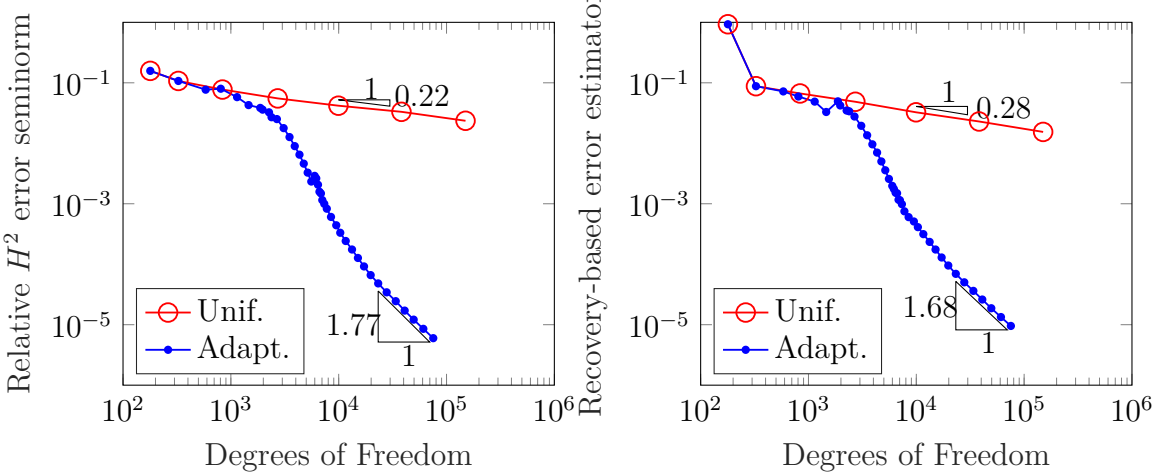

(c) $p = q = 4$, H^2 semi-norm

(d) $p = q = 4$, error estimator

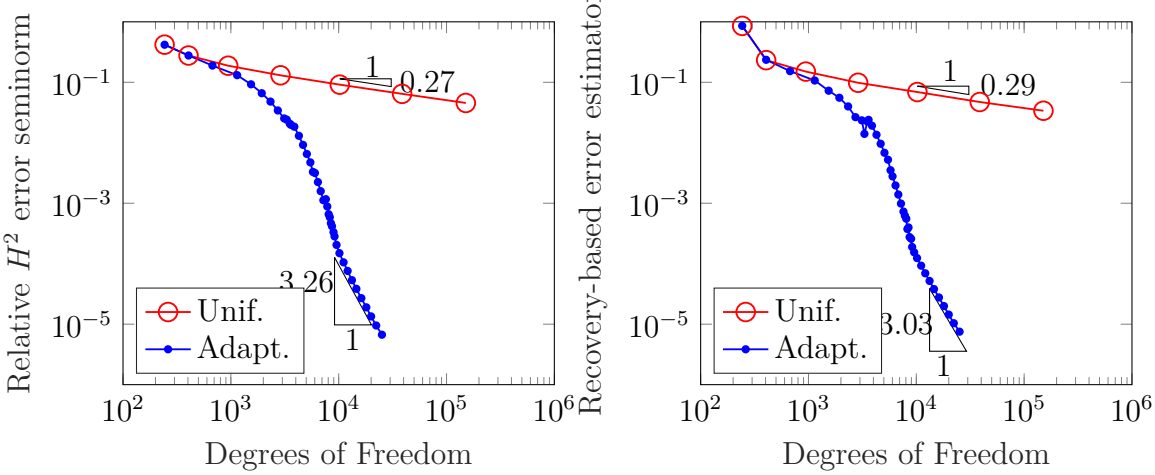

(e) $p = q = 5$, H^2 semi-norm

(f) $p = q = 5$, error estimator

Figure 5.6: Square plate with an edge crack: rates of convergence for (a),(c),(e) H^2 semi-norm and (b),(d),(f) recovery-based error estimator, for different p. Comparison between Uniform (Unif.) and recovery-based adaptive (Adapt.) refinement

5.1.2 Square plate with a central crack

In the second example, as shown in Figure 5.7, we consider a square plate with a central crack under constant moment loading M_0 applied on the two edges that are parallel to the crack.

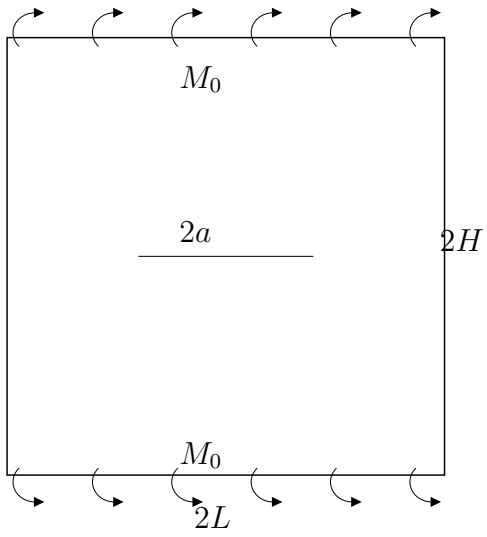

Figure 5.7: Plate with center crack subjected to constant moment M_0 applied on the two edges parallel to the crack

The plate dimensions are taken as: length $L = 2$, width $H = 2$ and thickness $h = 0.09$; while the material parameters are: Young's modulus $E = 14.98$[kPa], Poisson's ratio $\nu = 0.3$ and the constant moment loading $M_0 = 1$. This problem is also considered in [103, 133]. The reference stress intensity factor are:

$$k_1 = \frac{6M_0\sqrt{a}}{h^2} \quad , \quad k_2 = 0 \tag{5.3}$$

Figure 5.8 shows the numerical solution for the vertical displacement obtained using cubic PHT-Splines. Figure 5.9 shows six different adaptive refinement steps generated using PHT-splines of degree $p = q = 3$. Similarly to the previous example, the algorithm performs gradient refinement towards the two crack tips.

Figure 5.10 shows the convergence plots for the recovery-based error estimator using degree $p = q = 3, 4, 5$. Note that there is no known analytical solution in this particular example. As observed in the previous example, the convergence rate for the adaptive refinement is superior to the uniform refinement.

Figure 5.11 shows the plots for the normalized stress intensity factor k_1 using degree $p = q = 3, 4, 5$. It can be seen the improvement on the stress intensity factor k_1 by using the adaptive refinement procedure.

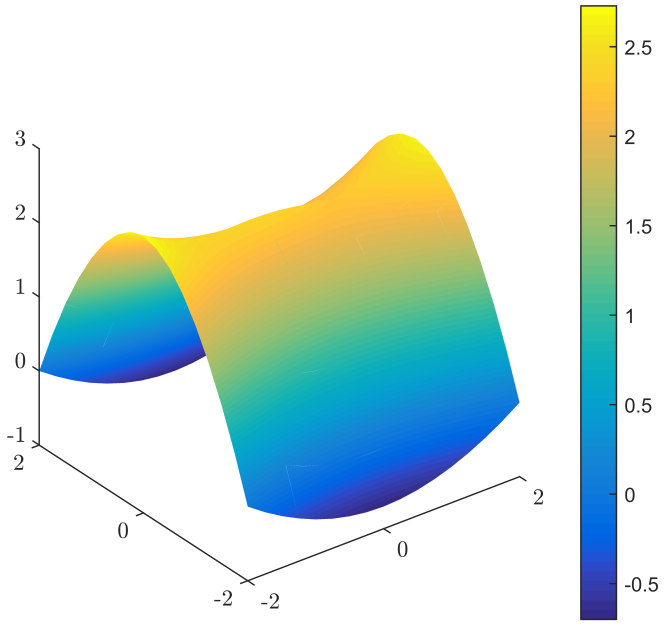

Figure 5.8: Numerical solution for the square plate with a center crack subject to constant moment

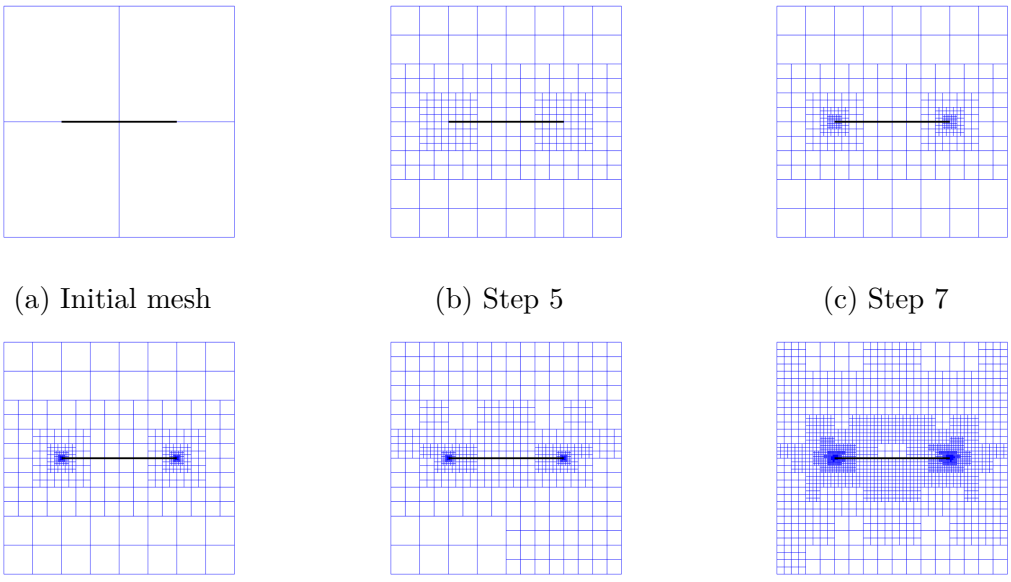

(a) Initial mesh (b) Step 5 (c) Step 7

(d) Step 12 (e) Step 15 (f) Step 20

Figure 5.9: Initial and refined meshes for the plate with central crack. PHT-Splines of degree $p = q = 3$. The black line represents the crack

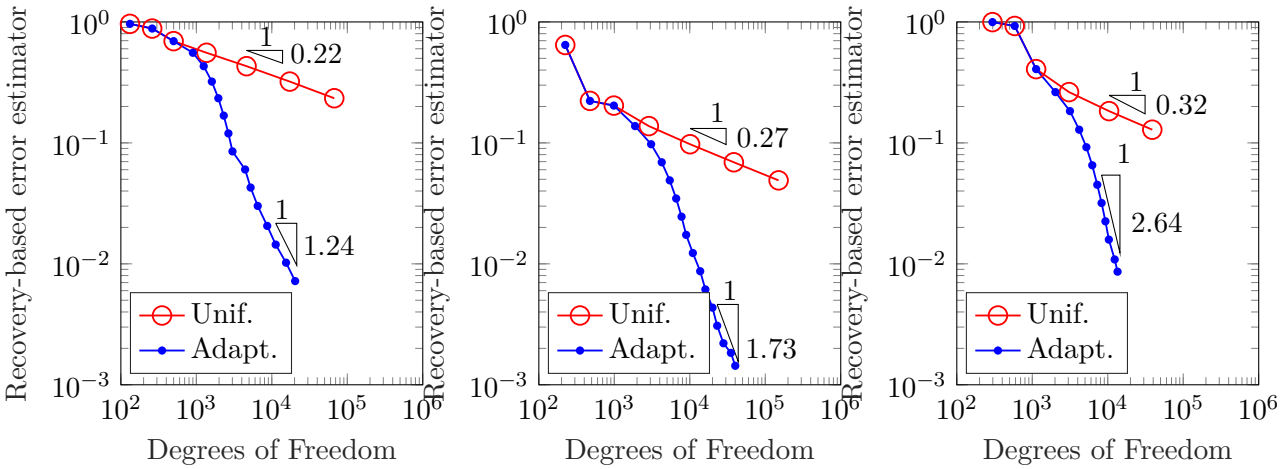

(a) $p = q = 3$. (b) $p = q = 4$. (c) $p = q = 5$.

Figure 5.10: Centered crack with constant moments problem: Convergences of recovery-based error estimator for degrees 3, 4 and 5. Comparison between Uniform (Unif.) and recovery-based adaptive (Adapt.) refinement

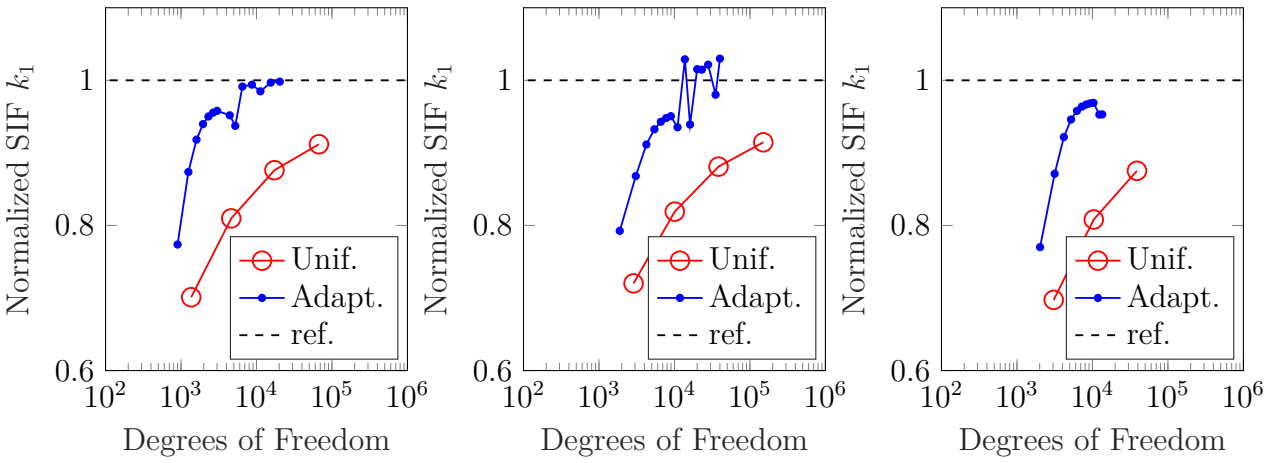

(a) $p = q = 3$. (b) $p = q = 4$. (c) $p = q = 5$.

Figure 5.11: Centered crack with constant moments problem: Normalized stress intensity factor k_1 for degrees 3, 4 and 5. Comparison between Uniform (Unif.) and recovery-based adaptive (Adapt.) refinement. Theoretical value is presented in the dashed line

5.1.3 Square plate with a central crack subjected to constant pressure loading

The following example includes a square plate with a central crack under uniform pressure loading $p = 1$ applied on the top of the plate. The plate is simply supported at all boundaries. This problem is also considered in [101] in the context of thin shell theory and in [123, 127] in the context of phantom node method.

The plate dimensions are: length $L = 1$, width $H = 1$, thickness $h = 0.1$ and crack length $a = 0.8$; while the material parameters are: Young's Modulus $E = 1000$ and Poisson's ratio $\nu = 0.3$ (see Figure 5.12).

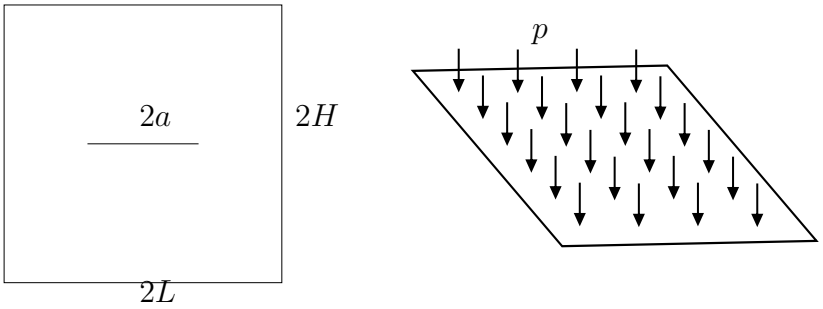

Figure 5.12: Plate with center crack subjected to a constant distributed load p applied on the top surface of the plate

Figure 5.13 shows the deformed shape of the plate using the numerical solution with PHT-Splines $p = q = 3$. Figure 5.14 shows the convergence plots for the recovery-based error estimator using uniform and adaptive refinement with PHT-Splines of degree $p = q = 3, 4, 5$. Again, as observed in the previous two examples, the convergence rate of the adaptive refinement is higher compared to the uniform one.

Figure 5.15 shows the convergence plot of the J-integral (eq.(3.101)) for $p = q = 3$ using uniform and adaptive refinement. The results are also compared with the results reported in [134, 101, 123, 127] for several numerical methods. Both uniform and adaptive refinement results are in agree with the reference results.

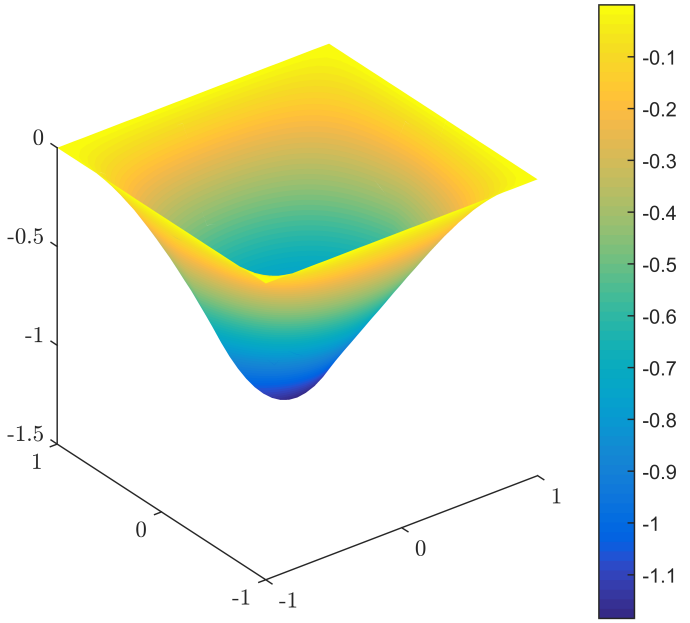

Figure 5.13: Numerical solution for the vertical displacement of the square plate with a straight crack subject to constant distributed loading, $a/L = 0.4$

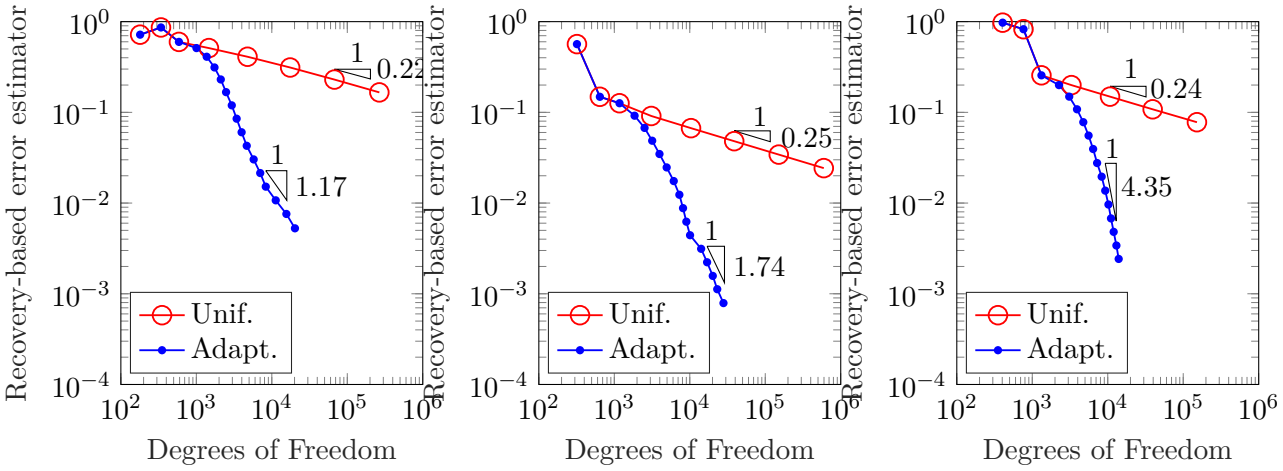

(a) $p = q = 3$. (b) $p = q = 4$. (c) $p = q = 5$.

Figure 5.14: Constant pressure loading problem: Convergence plot of recovery-based error estimator for degrees 3, 4 and 5. Comparison between Uniform (Unif.) and recovery-based adaptive (Adapt.) refinement

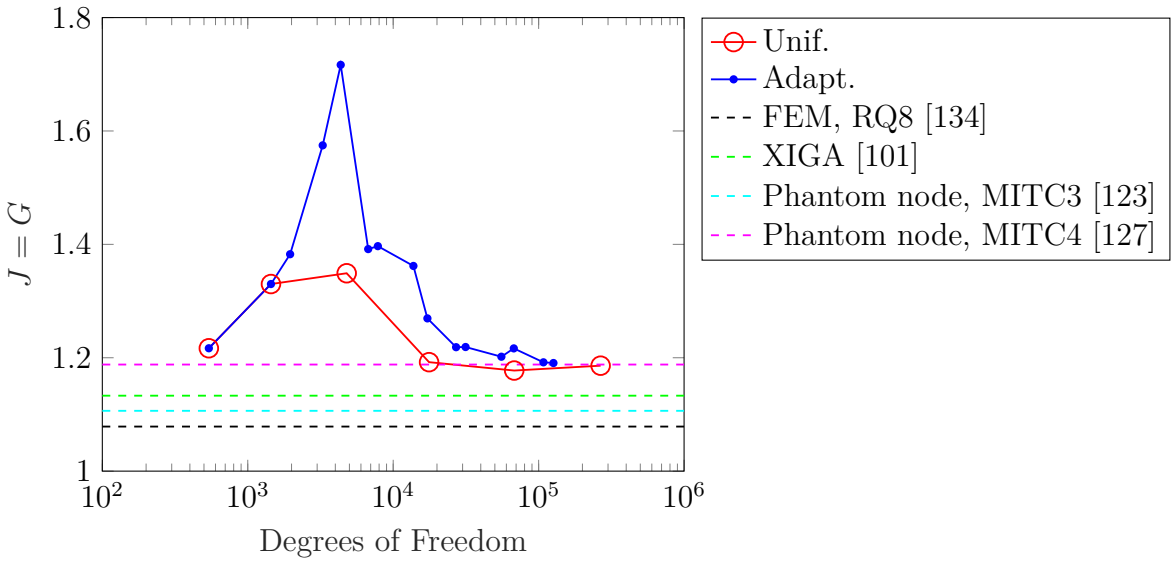

Figure 5.15: Constant pressure loading problem: Convergence plot of the J-integral for $p = 3$ and $a/L = 0.8$

5.2 Vibration of plates with cracks

5.2.1 Square plate with central crack

We perform the vibration analysis of the plate of the same geometry as in the previous example. In this example, the material parameters are: Young's Modulus $E = 2e11$, Poisson's ratio $\nu = 0.3$ and density $\rho = 6000$. The plate dimensions are taken as: $L = H = 5$ and the thickness $h = 0.1$. The crack length a is kept variable to study the influence of the crack length on the natural modes.

The natural frequencies ω are normalized as:

$$\overline{\omega} = \omega L^2 \sqrt{\frac{\rho h}{D}} \tag{5.4}$$

Figure 5.16 shows the convergence plot for the first three vibration modes, using $p = 3, 4, 5$ and $a/L = 0.4$. For each mode, the reference results are also included. In this case, the different degrees leads to similar results with no major difference in the convergence or the number of DOF. Tables 5.3 and 5.4 show the normalized natural frequencies $\overline{\omega}$ obtained for the first six natural modes, using PHT-splines of degree $p = q = 3, 4, 5$ and crack ratio of a/L equal to 0.4 and 0.8, respectively. The results are also compared with the data available in the literature. In both cases ($a/L = 0.4$ and 0.8) the results obtained for different degrees p agree with the results obtained for the other authors. Figure 5.17 shows the first six modes for a simply supported square plate with a crack ratio of $a/L = 0.4$.

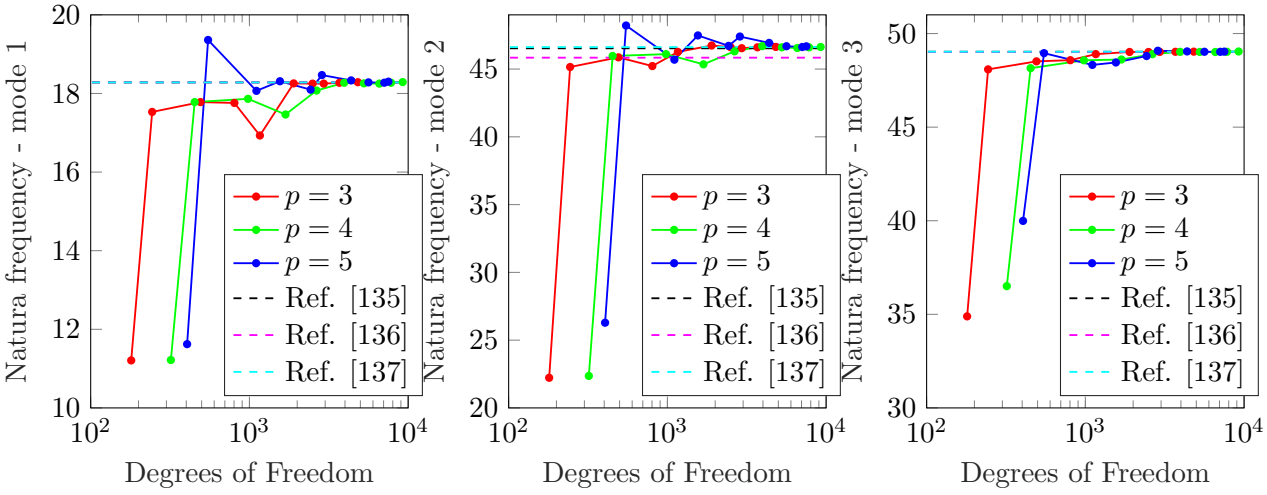

(a) Mode 1 (b) Mode 2 (c) Mode 3

Figure 5.16: Square plate with central crack problem: Convergence plot of the first three vibration modes. Adaptive (Adapt.) refinement using $p = 3, 4, 5$. $a/L = 0.4$

Method	Degree	Modes					
		1	2	3	4	5	6
PHT-Splines GIFT	3	18.287	46.633	49.034	78.612	85.493	98.604
	4	18.290	46.629	49.043	78.610	85.497	98.600
	5	18.283	46.623	49.031	78.609	85.490	98.599
Reference [135]		18.281	46.533	49.028	78.579	85.414	98.678
Reference [136]		18.28	45.84	49.02	78.41	84.96	98.65
Reference [137]		18.28	46.62	49.03	78.60	85.51	98.68

Table 5.3: Normalized natural frequencies of a simply supported plate with a central crack of crack ratio $a/L = 0.4$

Method	Degree	Modes					
		1	2	3	4	5	6
PHT-Splines GIFT	3	16.408	27.765	47.203	65.743	76.359	78.382
	4	16.407	27.761	47.202	65.738	76.359	78.379
	5	16.423	27.760	47.186	65.733	76.360	78.363
Reference [135]		16.401	27.743	47.255	65.587	76.371	78.256
Reference [136]		16.40	26.71	47.23	64.39	76.36	77.96
Reference [137]		16.40	27.77	47.26	65.73	76.37	78.38

Table 5.4: Normalized natural frequencies of a simply supported plate with a central crack of crack ratio $a/L = 0.8$

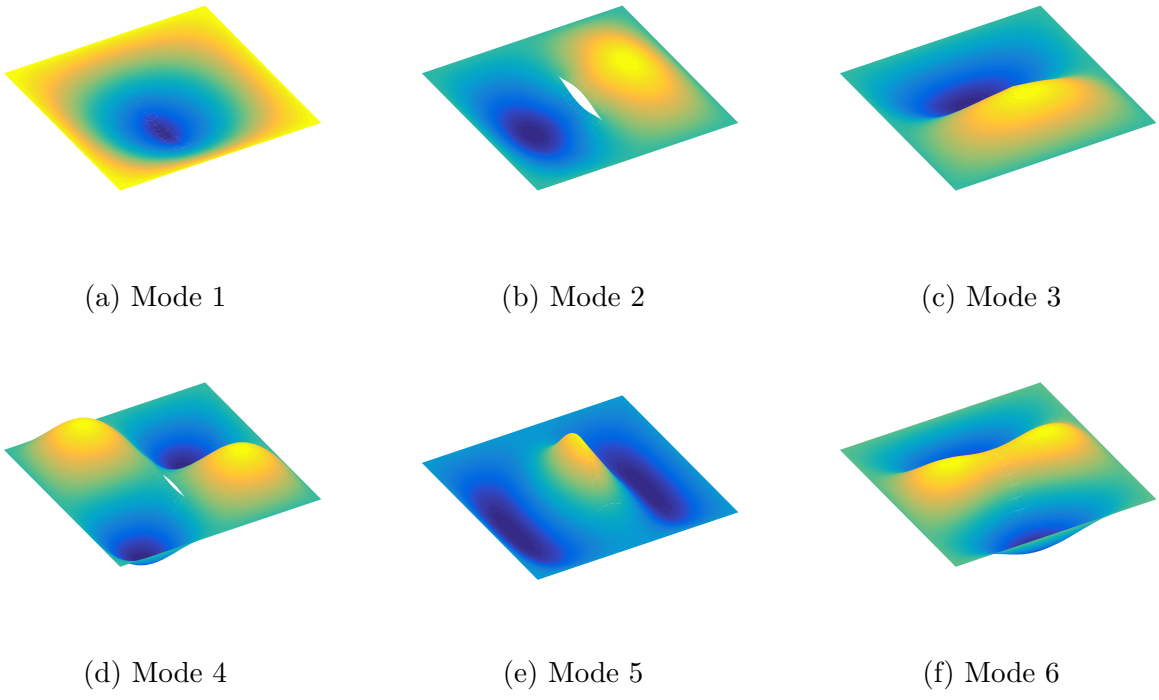

(a) Mode 1 (b) Mode 2 (c) Mode 3

(d) Mode 4 (e) Mode 5 (f) Mode 6

Figure 5.17: The first six vibration mode shape for a simply supported square plate with a crack ratio of $a/L = 0.4$

5.2.2 Clamped circular plate with a central crack

In this problem, the numerical results of the vibration analysis for a circular plate with a central crack are presented. The plate has a radius R, thickness $h = R/2$ and a crack of length $2a$. The plate is fully clamped (see Figure 5.18). The material parameters are: Young's Modulus $E = 70e9$, Poisson's ratio $\nu = 0.3$ and density $\rho = 2707$.

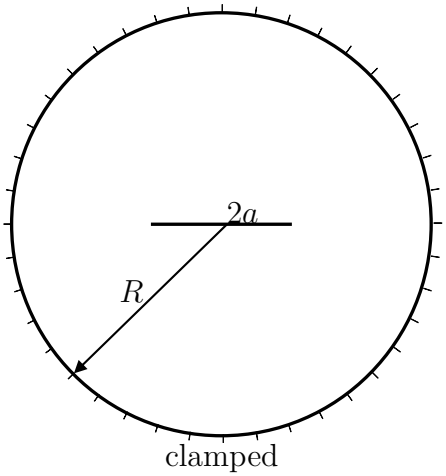

Figure 5.18: Circular plate with center crack

The information necessary to generate the circular geometry with NURBS is presented in the Table A.5. In this example, the normalized natural frequencies are defined as:

$$\overline{\omega} = \omega \frac{R^2}{h} \sqrt{\frac{\rho}{E}} \tag{5.5}$$

Figure 5.19 shows the convergence plot of the first vibration mode, using uniform and adaptive refinement, with $p = 3, 4, 5$. For each degree, the adaptive refinement shows a faster convergence to the vibration mode. Table 5.5 shows the normalized natural frequencies obtained for the first six natural modes, using PHT-splines of degree $p = q = 3, 4, 5$ and crack ratio of a/R equal to 0.25 and 0.5, respectively. Also, this table compares the results obtained by the use of uniform and adaptive refinement for each degree, and we can see that the adaptive refinement provides a more cheaper solution than the uniform refinement (in terms of number of Degrees of freedom) for each case analyzed.

Figure 5.20 shows the first six modes for a clamped circular plate with a crack ratio of $a/R = 0.25$.

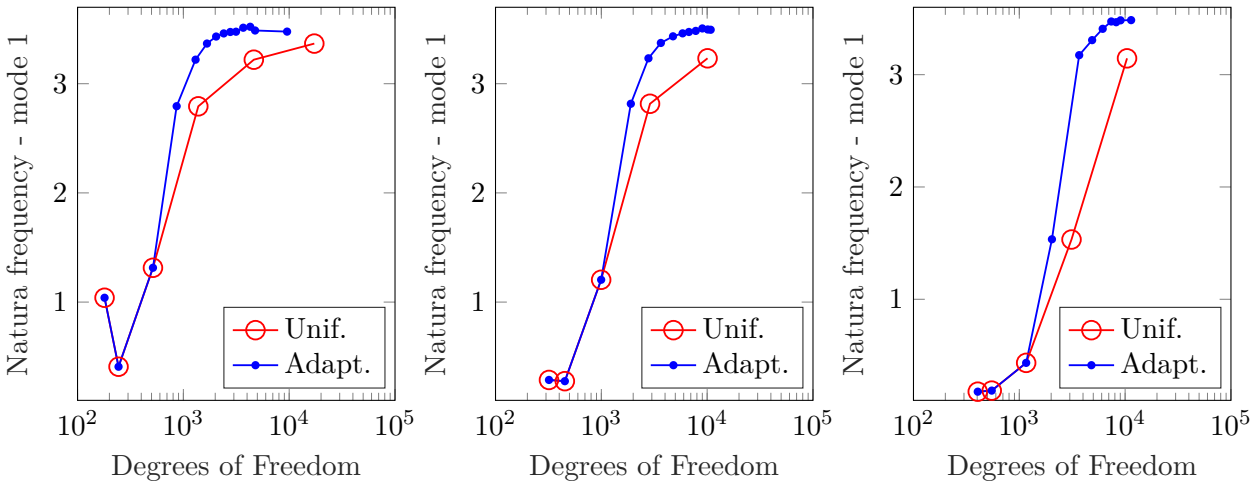

(a) $p = 3$ (b) $p = 4$ (c) $p = 5$

Figure 5.19: Circular plate with a crack: Convergence plot of the first vibration mode. Comparison between uniform (Unif.) and adaptive (Adapt.) refinement using $p = 3, 4, 5$ and a crack ratio of $a/R = 0.25$

a/R	Degree	Type of Refinement	Mode					
			1	2	3	4	5	6
0.25	3	Uniform (17272 DOF)	3.367	6.766	6.901	10.333	11.518	11.830
		Adaptive (9552 DOF)	3.467	6.911	7.071	10.700	11.588	12.059
	4	Uniform (10084 DOF)	3.233	6.528	6.770	9.949	11.374	11.419
		Adaptive (10796 DOF)	3.494	6.910	7.071	10.698	11.588	12.061
	5	Uniform (10422 DOF)	3.145	5.763	6.409	7.109	7.154	9.608
		Adaptive (11394 DOF)	3.486	6.902	7.066	10.679	11.587	12.048
0.5	3	Uniform (17464 DOF)	3.224	4.722	6.648	9.564	10.274	10.598
		Adaptive (14956 DOF)	3.296	5.102	6.808	9.860	10.685	10.865
	4	Uniform (10276 DOF)	3.159	4.740	6.353	9.230	10.399	10.591
		Adaptive (12060 DOF)	3.280	5.098	6.837	9.846	10.683	10.864
	5	Uniform (10638 DOF)	3.116	4.393	5.677	6.989	7.127	9.287
		Adaptive (12150 DOF)	3.319	5.082	6.873	9.836	10.673	10.852

Table 5.5: Normalized natural frequencies for a simply supported circular plate with a central crack

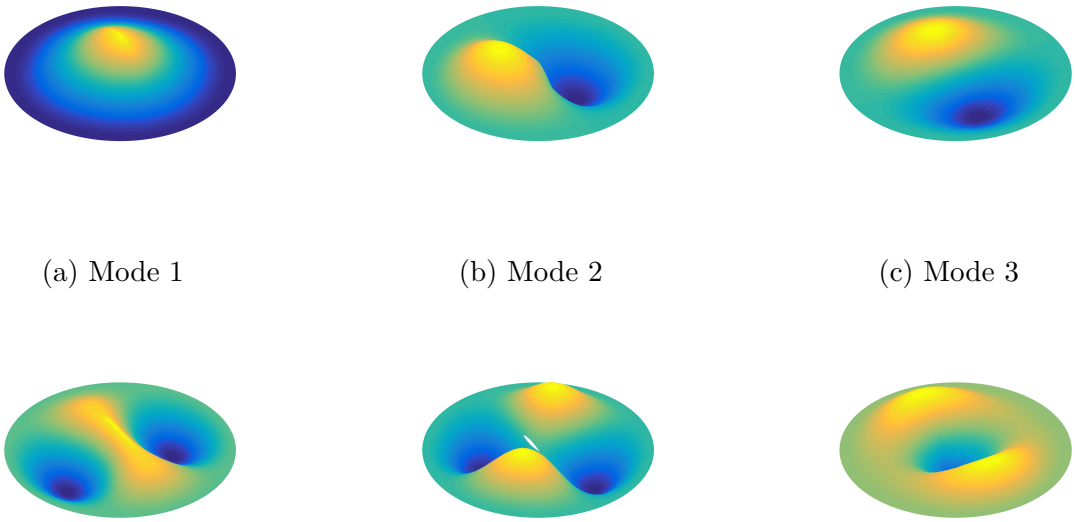

(a) Mode 1 (b) Mode 2 (c) Mode 3

(d) Mode 4 (e) Mode 5 (f) Mode 6

Figure 5.20: The first six vibration mode shape for the circular plate with a center crack with $R = 10$ and crack length $a = 2.5$

5.2.3 Clamped annular plate with 2 symmetric cracks

In this section, the numerical results of the vibration analysis for a annular plate with two symmetric cracks emanating from the inner edge are presented. The plate has internal radius r, external radius R and two symmetric cracks of length $a = 0.1$. The plate is clamped in the exterior radius, while the internal radius is free, as it can be seen in Figure 5.21. The material parameters are: Young's Modulus $E = 70e9$, Poisson's ratio $\nu = 0.3$ and density $\rho = 2707$.

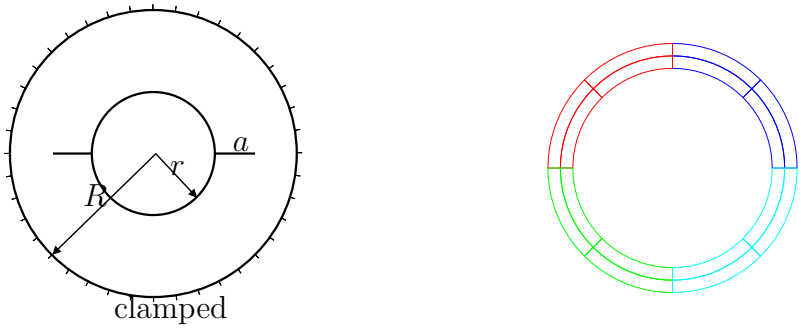

(a) Problem domain. (b) NURBS patches.

Figure 5.21: Annular plate with two symmetric cracks: Problem domain and NURBS patches

The information necessary to generate the annular geometry are presented in the Table A.6. The geometry is parameterized by four symmetric NURBS of degree 1 and 2.

The normalized natural frequencies are defined as

$$\overline{\omega} = \omega \frac{(R-r)^2}{h}\sqrt{\frac{\rho}{E}} \tag{5.6}$$

Table 5.6 shows the normalized natural frequencies obtained for the first six natural modes, using PHT-splines of degree $p = q = 3, 4, 5$ and radius ratio of r/R equal to 0.6 and 0.8, respectively. Also, this table compares the results obtained by the use of uniform and adaptive refinement for each degree, and we can see that the adaptive refinement provide a more precise solution that uniform refinement for each case analyzed.

Figure 5.22 shows the first six modes for a clamped annular plate with a radius ratio of $r/R = 0.8$.

r/R	Degree	Type of Refinement	Mode					
			1	2	3	4	5	6
0.6	3	Uniform (17832 DOF)	1.241	1.258	1.358	1.479	1.501	1.775
		Adaptive (8844 DOF)	1.242	1.259	1.359	1.480	1.506	1.782
	4	Uniform (10592 DOF)	1.238	1.255	1.353	1.477	1.487	1.757
		Adaptive (9002 DOF)	1.242	1.259	1.359	1.480	1.506	1.783
	5	Uniform (11256 DOF)	1.236	1.252	1.349	1.475	1.476	1.743
		Adaptive (10582 DOF)	1.236	1.270	1.360	1.474	1.507	1.783
0.8	3	Uniform (17832 DOF)	1.122	1.123	1.153	1.164	1.166	1.195
		Adaptive (13048 DOF)	1.130	1.143	1.165	1.171	1.203	1.228
	4	Uniform (10592 DOF)	1.063	1.063	1.147	1.153	1.162	1.183
		Adaptive (17012 DOF)	1.131	1.137	1.157	1.164	1.168	1.205
	5	Uniform (11256 DOF)	1.161	1.181	1.194	1.216	1.246	1.298
		Adaptive (16188 DOF)	1.511	1.564	1.729	1.824	1.955	1.973

Table 5.6: Normalized natural frequencies for a clamped annular plate with two symmetric cracks

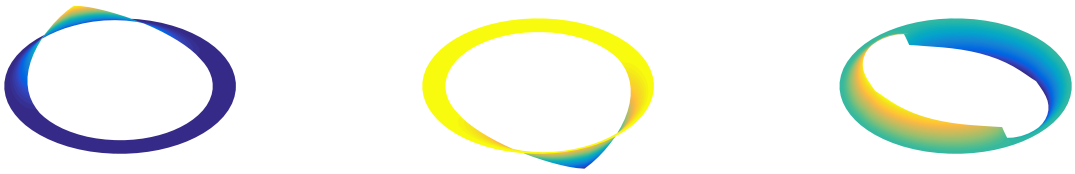

(a) Mode 1 (b) Mode 2 (c) Mode 3

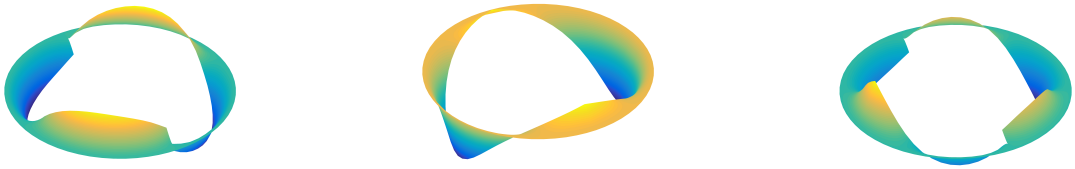

(d) Mode 4 (e) Mode 5 (f) Mode 6

Figure 5.22: The first six vibration mode shape for the clamped annular plate with two symmetric cracks with $R = 1$, $r = 0.8$ and crack length $a = 0.1$

Chapter 6

Conclusion

In this work we show applications of PHT-splines in the framework of Geometry Independent Field approximaTion (GIFT) for problems of time-harmonic acoustics modeled by the Helmholtz equation and fracture mechanics of thin plated modeled by the Kirchhoff-Love theory.

For acoustics problems, the following conclusions can be drawn:

- Numerical simulations demonstrate that, for problems where solutions exhibit singularities, adaptive refinement allows to capture local characteristics of the solution and significantly improve the convergence rate.
- Local refinement is efficient only when the global mesh is fine enough to approximate the oscillations of the solution associated with the value of parameter k. This condition is expressed as $kh/p < 1$ (pre-asymptotic regime), where h is the biggest element in the mesh and p is the degree of the PHT-splines. As the value of k grows, the efficiency of local refinement per number of degree of freedom deteriorates.
- Numerical studies also indicate that residual-based and recovery-based error estimators yield quasi-identical results, although each error estimator was paired with a different marking strategy.
- Regarding the recovery-based error estimator, because the effectivity index tends to 1, it can be concluded that this error estimator is a reliable measure of the error of the solution, and can be employed to study convergence in problems with no known analytical solution.

For fracture mechanics problems of thin plates, the following conclusions can be drawn:

- An extended formulation based on GIFT and XFEM was proposed and implemented. This formulation allows us to model the crack opening in both static and dynamic simulations, as demonstrated by the numerical examples.
- Numerical simulations show that adaptive refinement refines focused on the crack faces and crack tip, allowing to obtain improved results for both error norms and stress intensity factors, using less DOF compared to an uniform refinement.
- In particular, adaptive refinement applied to dynamic analysis allows to compute the

vibration modes with less DOF than an uniform refinement.

- Nevertheless, the recovery-based error estimator and "Dörfler marking" strategy employed for this type of problems seems to be more sensitive to the percentage of refinement considered, allowing to obtain better results with small percentages of refinement.

The results of this work also serve to further verify the concept of Geometry Independent Field approximaTion (GIFT). The original (coarse) NURBS parameterization of the computational domain is paired with the PHT-splines approximation of the solution and remains unchanged during the refinement process. While it was out of scoope of this thesis to probe the efficiency of GIFT-simulations over IGA, it can be noted, that with GIFT, the use of PHT-splines and the necessity to refine and store the control points and their weights, can be avoided, which lead to certain computational savings for big problems.

Bibliography

[1] T. Hughes, J. Cottrell, and Y. Bazilevs, "Isogeometric analysis: CAD, finite elements, NURBS, exact geometry and mesh refinement," *Computer Methods in Applied Mechanics and Engineering*, vol. 194, no. 39, pp. 4135–4195, 2005.

[2] X. Zhang, C. Jin, P. Hu, X. Zhu, W. Hou, J. Xu, C. Wang, Y. Zhang, Z.-D. Ma, and H. Smith, "NURBS modeling and isogeometric shell analysis for complex tubular engineering structures," *Computational and Applied Mathematics*, vol. 36, no. 4, pp. 1659–1679, 2017.

[3] W. A. Wall, M. A. Frenzel, and C. Cyron, "Isogeometric structural shape optimization," *Computer Methods in Applied Mechanics and Engineering*, vol. 197, no. 33-40, pp. 2976–2988, 2008.

[4] Y.-D. Seo, H.-J. Kim, and S.-K. Youn, "Shape optimization and its extension to topological design based on isogeometric analysis," *International Journal of Solids and Structures*, vol. 47, no. 11-12, pp. 1618–1640, 2010.

[5] B. Hassani, S. M. Tavakkoli, and N. Moghadam, "Application of isogeometric analysis in structural shape optimization," *Scientia Iranica*, vol. 18, no. 4, pp. 846–852, 2011.

[6] Y. Bazilevs, V. Calo, Y. Zhang, and T. Hughes, "Isogeometric fluid–structure interaction analysis with applications to arterial blood flow," *Computational Mechanics*, vol. 38, no. 4-5, pp. 310–322, 2006.

[7] Y. Bazilevs, V. Calo, T. Hughes, and Y. Zhang, "Isogeometric fluid-structure interaction: theory, algorithms, and computations," *Computational Mechanics*, vol. 43, no. 1, pp. 3–37, 2008.

[8] Y. Bazilevs, M.-C. Hsu, and M. Scott, "Isogeometric fluid–structure interaction analysis with emphasis on non-matching discretizations, and with application to wind turbines," *Computer Methods in Applied Mechanics and Engineering*, vol. 249, pp. 28–41, 2012.

[9] J. Kiendl, K.-U. Bletzinger, J. Linhard, and R. Wüchner, "Isogeometric shell analysis with Kirchhoff–Love elements," *Computer Methods in Applied Mechanics and Engineering*, vol. 198, no. 49-52, pp. 3902–3914, 2009.

[10] D. Benson, Y. Bazilevs, M.-C. Hsu, and T. Hughes, "Isogeometric shell analysis: the

Reissner–Mindlin shell," *Computer Methods in Applied Mechanics and Engineering*, vol. 199, no. 5-8, pp. 276–289, 2010.

[11] J. Cottrell, A. Reali, Y. Bazilevs, and T. Hughes, "Isogeometric analysis of structural vibrations," *Computer Methods in Applied Mechanics and Engineering*, vol. 195, no. 41-43, pp. 5257–5296, 2006.

[12] A. Reali, "An isogeometric analysis approach for the study of structural vibrations," *Journal of Earthquake Engineering*, vol. 10, no. spec01, pp. 1–30, 2006.

[13] S. Shojaee, E. Izadpanah, N. Valizadeh, and J. Kiendl, "Free vibration analysis of thin plates by using a NURBS-based isogeometric approach," *Finite Elements in Analysis and Design*, vol. 61, pp. 23–34, 2012.

[14] E. De Luycker, D. Benson, T. Belytschko, Y. Bazilevs, and M. Hsu, "X-FEM in isogeometric analysis for linear fracture mechanics," *International Journal for Numerical Methods in Engineering*, vol. 87, no. 6, pp. 541–565, 2011.

[15] S. Ghorashi, N. Valizadeh, and S. Mohammadi, "Extended isogeometric analysis for simulation of stationary and propagating cracks," *International Journal for Numerical Methods in Engineering*, vol. 89, no. 9, pp. 1069–1101, 2012.

[16] S. Ghorashi, N. Valizadeh, S. Mohammadi, and T. Rabczuk, "Extended isogeometric analysis of plates with curved cracks," in *Proceedings of the eighth international conference on engineering computational technology, Civil-Comp Press, Stirlingshire, UK*, 2012.

[17] L. Bernal, V. M. Calo, N. Collier, G. Espinosa, F. Fuentes, and J. Mahecha, "Isogeometric analysis of hyperelastic materials using PetIGA," *Procedia Computer Science*, 2013.

[18] T. Elguedj and T. Hughes, "Isogeometric analysis of nearly incompressible large strain plasticity," *Computer Methods in Applied Mechanics and Engineering*, vol. 268, pp. 388–416, 2014.

[19] J. Kiendl, M.-C. Hsu, M. C. Wu, and A. Reali, "Isogeometric Kirchhoff–Love shell formulations for general hyperelastic materials," *Computer Methods in Applied Mechanics and Engineering*, vol. 291, pp. 280–303, 2015.

[20] E. Atroshchenko, S. Tomar, G. Xu, and S. Bordas, "Weakening the tight coupling between geometry and simulation in isogeometric analysis: From sub-and super-geometric analysis to Geometry-Independent Field approximaTion (GIFT)," *International Journal for Numerical Methods in Engineering*, vol. 114, no. 10, pp. 1131–1159, 2018.

[21] A. Perduta and R. Putanowicz, "Tools and techniques for building models for isogeometric analysis," *Advances in Engineering Software*, vol. 127, pp. 70–81, 2019.

[22] GiD The personal pre and post processor, *Isogeometric analysis (IGA) Archives*, (accessed November 8, 2018). `https://www.gidhome.com/category/examples/iga/`.

[23] Y. Lai, L. Liu, Y. J. Zhang, J. Chen, E. Fang, and J. Lua, "Rhino 3D to Abaqus: A T-Spline Based Isogeometric Analysis Software Framework," in *Advances in Computational Fluid-Structure Interaction and Flow Simulation*, pp. 271–281, Springer, 2016.

[24] T. Sederberg, J. Zheng, A. Bakenov, and A. Nasri, "T-splines and T-NURCCs," *ACM transactions on graphics (TOG)*, vol. 22, no. 3, pp. 477–484, 2003.

[25] T. Sederberg, D. Cardon, G. Finnigan, N. North, J. Zheng, and T. Lyche, "T-spline simplification and local refinement," *ACM transactions on graphics (TOG)*, vol. 23, no. 3, pp. 276–283, 2004.

[26] Y. Bazilevs, V. Calo, J. Cottrell, J. Evans, T. Hughes, S. Lipton, M. Scott, and T. Sederberg, "Isogeometric analysis using T-splines," *Computer Methods in Applied Mechanics and Engineering*, vol. 199, no. 5, pp. 229–263, 2010.

[27] M. Dörfel, B. Jüttler, and B. Simeon, "Adaptive isogeometric analysis by local h-refinement with T-splines," *Computer Methods in Applied Mechanics and Engineering*, vol. 199, no. 5, pp. 264–275, 2010.

[28] L. Beirão da Veiga, A. Buffa, D. Cho, and G. Sangalli, "Isogeometric analysis using T-splines on two-patch geometries," *Computer Methods in Applied Mechanics and Engineering*, vol. 200, no. 21, pp. 1787–1803, 2011.

[29] S. Ghorashi, N. Valizadeh, S. Mohammadi, and T. Rabczuk, "T-spline based XIGA for fracture analysis of orthotropic media," *Computers & Structures*, vol. 147, pp. 138–146, 2015.

[30] J. Deng, F. Chen, and Y. Feng, "Dimensions of spline spaces over T-meshes," *Journal of Computational and Applied Mathematics*, vol. 194, no. 2, pp. 267–283, 2006.

[31] J. Deng, F. Chen, X. Li, C. Hu, W. Tong, Z. Yang, and Y. Feng, "Polynomial splines over hierarchical T-meshes," *Graphical models*, vol. 70, no. 4, pp. 76–86, 2008.

[32] P. Wang, J. Xu, J. Deng, and F. Chen, "Adaptive isogeometric analysis using rational PHT-splines," *Computer-Aided Design*, vol. 43, no. 11, pp. 1438–1448, 2011.

[33] N. Nguyen-Thanh, H. Nguyen-Xuan, S. Bordas, and T. Rabczuk, "Isogeometric analysis using polynomial splines over hierarchical T-meshes for two-dimensional elastic solids," *Computer Methods in Applied Mechanics and Engineering*, vol. 200, no. 21, pp. 1892–1908, 2011.

[34] N. Nguyen-Thanh, J. Muthu, X. Zhuang, and T. Rabczuk, "An adaptive three-dimensional RHT-splines formulation in linear elasto-statics and elasto-dynamics," *Computational Mechanics*, vol. 53, no. 2, pp. 369–385, 2014.

[35] N. Nguyen-Thanh, J. Kiendl, H. Nguyen-Xuan, R. Wüchner, K. Bletzinger, Y. Bazilevs, and T. Rabczuk, "Rotation free isogeometric thin shell analysis using PHT-splines," *Computer Methods in Applied Mechanics and Engineering*, vol. 200, no. 47, pp. 3410–3424, 2011.

[36] N. Nguyen-Thanh and K. Zhou, "Extended isogeometric analysis based on PHT-splines for crack propagation near inclusions," *International Journal for Numerical Methods in Engineering*, 2017.

[37] N. Nguyen-Thanh, K. Zhou, X. Zhuang, P. Areias, H. Nguyen-Xuan, Y. Bazilevs, and T. Rabczuk, "Isogeometric analysis of large-deformation thin shells using RHT-splines for multiple-patch coupling," *Computer Methods in Applied Mechanics and Engineering*, vol. 316, pp. 1157–1178, 2017.

[38] B. Marussig, J. Zechner, G. Beer, and T. Fries, "Fast isogeometric boundary element method based on independent field approximation," *Computer Methods in Applied Mechanics and Engineering*, vol. 284, pp. 458–488, 2015.

[39] C. Anitescu, M. Hossain, and T. Rabczuk, "Recovery-based error estimation and adaptivity using high-order splines over hierarchical T-meshes," *Computer Methods in Applied Mechanics and Engineering*, vol. 328, pp. 638–662, 2018.

[40] P. Yu, C. Anitescu, S. Tomar, S. Bordas, and P. Kerfriden, "Adaptive isogeometric analysis for plate vibrations: An efficient approach of local refinement based on hierarchical a posteriori error estimation," *Computer Methods in Applied Mechanics and Engineering*, vol. 342, pp. 251–286, 2018.

[41] O. Zienkiewicz and J. Zhu, "A simple error estimator and adaptive procedure for practical engineering analysis," *International Journal for Numerical Methods in Engineering*, vol. 24, no. 2, pp. 337–357, 1987.

[42] O. Zienkiewicz and J. Zhu, "The superconvergent patch recovery and a posteriori error estimates. Part 1: The recovery technique," *International Journal for Numerical Methods in Engineering*, vol. 33, no. 7, pp. 1331–1364, 1992.

[43] O. Zienkiewicz and J. Zhu, "The superconvergent patch recovery and *a posteriori* error estimates. Part 2: Error estimates and adaptivity," *International Journal for Numerical Methods in Engineering*, vol. 33, no. 7, pp. 1365–1382, 1992.

[44] M. Ainsworth and J. Oden, "A posteriori error estimation in finite element analysis," *Computer Methods in Applied Mechanics and Engineering*, vol. 142, no. 1-2, pp. 1–88, 1997.

[45] M. Ainsworth and J. Oden, *A posteriori error estimation in finite element analysis*, vol. 37. John Wiley & Sons, 2011.

[46] I. Babuvška and W. C. Rheinboldt, "Error estimates for adaptive finite element computations," *SIAM Journal on Numerical Analysis*, vol. 15, no. 4, pp. 736–754, 1978.

[47] I. Babuvška and W. C. Rheinboldt, "Reliable Error Estimation and Mesh Adaptation for the Finite Element Method," *Computational Methods in Nonlinear Mechanics*, pp. 67–109, 1980.

[48] I. Babuvška and W. C. Rheinboldt, "A posteriori error analysis of finite element so-

lutions for one-dimensional problems," *SIAM Journal on Numerical Analysis*, vol. 18, no. 3, pp. 565–589, 1981.

[49] J. Oden, S. Prudhomme, and L. Demkowicz, "A posteriori error estimation for acoustic wave propagation problems," *Archives of Computational Methods in Engineering*, vol. 12, no. 4, pp. 343–389, 2005.

[50] O. Zienkiewicz, B. Boroomand, and J. Zhu, "Recovery procedures in error estimation and adaptivity Part I: Adaptivity in linear problems," *Computer Methods in Applied Mechanics and Engineering*, vol. 176, no. 1-4, pp. 111–125, 1999.

[51] I. Babuška, T. Strouboulis, C. Upadhyay, and S. Gangaraj, "Computer-Based Proof of the Existence of Superconvergence Points in the Finite Element Method; Superconvergence of the Derivatives in Finite Element Solutions of Laplace's, Poisson's, and the Elasticity Equations," *Numerical Methods for Partial Differential Equations*, vol. 12, no. 3, pp. 347–392, 1996.

[52] C. Anitescu, Y. Jia, Y. J. Zhang, and T. Rabczuk, "An isogeometric collocation method using superconvergent points," *Computer Methods in Applied Mechanics and Engineering*, vol. 284, pp. 1073–1097, 2015.

[53] M. Kumar, T. Kvamsdal, and K. Johannessen, "Superconvergent patch recovery and a posteriori error estimation technique in adaptive isogeometric analysis," *Computer Methods in Applied Mechanics and Engineering*, vol. 316, pp. 1086–1156, 2017.

[54] S. Bordas and M. Duflot, "Derivative recovery and a posteriori error estimate for extended finite elements," *Computer Methods in Applied Mechanics and Engineering*, vol. 196, no. 35-36, pp. 3381–3399, 2007.

[55] S. Bordas, M. Duflot, and P. Le, "A simple error estimator for extended finite elements," *Communications in Numerical Methods in Engineering*, vol. 24, no. 11, pp. 961–971, 2008.

[56] M. Duflot and S. Bordas, "A posteriori error estimation for extended finite elements by an extended global recovery," *International Journal for Numerical Methods in Engineering*, vol. 76, no. 8, pp. 1123–1138, 2008.

[57] A. Ben-Menahem and S. Singh, *Seismic waves and sources*. Springer Science & Business Media, 2012.

[58] P. Kumar, "Theoretical analysis of extreme wave oscillation in Paradip Port using a 3-D boundary element method," *Ocean Engineering*, vol. 164, pp. 13–22, 2018.

[59] J. Cruz, *Ocean wave energy: current status and future prespectives*. Springer Science & Business Media, 2007.

[60] J. Scruggs and P. Jacob, "Harvesting ocean wave energy," *Science*, vol. 323, no. 5918, pp. 1176–1178, 2009.

[61] N. Booij, R. Ris, and L. Holthuijsen, "A third-generation wave model for coastal regions: 1. Model description and validation," *Journal of Geophysical Research: Oceans*, vol. 104, no. C4, pp. 7649–7666, 1999.

[62] R. Kapoor, S. Ramasamy, A. Gardi, R. Schyndel, and R. Sabatini, "Acoustic Sensors for Air and Surface Navigation Applications," *Sensors*, vol. 18, no. 2, p. 499, 2018.

[63] P. Lasaygues, R. Guillermin, and J. Lefebvre, "Ultrasonic computed tomography," in *Bone Quantitative Ultrasound*, pp. 441–459, Springer, 2011.

[64] G. Gladwell, "A variational formulation of damped acousto structural vibration problems," *Journal of Sound and Vibration*, vol. 4, no. 2, pp. 172 – 186, 1966.

[65] I. Babuška and S. Sauter, "Is the pollution effect of the FEM avoidable for the Helmholtz equation considering high wave numbers?," *SIAM Journal on Numerical Analysis*, vol. 34, no. 6, pp. 2392–2423, 1997.

[66] F. Ihlenburg and I. Babuška, "Finite Element Solution of the Helmholtz Equation with High Wave Number Part I: The h-Version of the FEM," *Computers and Mathematics with Applications*, vol. 30, no. 9, pp. 9 – 37, 1995.

[67] F. Ihlenburg and I. Babuška, "Finite Element Solution of the Helmholtz Equation with High Wave Number Part II: The h-p Version of the FEM," *SIAM Journal on Numerical Analysis*, vol. 34, no. 1, pp. 315 – 358, 1997.

[68] J. M. Melenk and S. Sauter, "Convergence analysis for finite element discretizations of the Helmholtz equation with Dirichlet-to-Neumann boundary conditions," *Mathematics of Computation*, vol. 79, no. 272, pp. 1871–1914, 2010.

[69] M. Ainsworth, "Discrete Dispersion Relation for hp-Version Finite Element Approximation at High Wave Number," *SIAM Journal on Numerical Analysis*, vol. 42, no. 2, pp. 553–575, 2005.

[70] I. Babuška and S. Sauter, "Is the Pollution Effect of the FEM Avoidable for the Helmholtz Equation Considering High Wave Numbers?," *SIAM Journal on Numerical Analysis*, vol. 6, no. 34, pp. 2392–2423, 1997.

[71] K. Baumeister, "Analysis of sound propagation in ducts using the wave envelope concept," *Technical report, NASA TN D-7719*, 1974.

[72] E. Giladi and J. Keller, "A Hybrid Numerical Asymptotic Method for Scattering Problems," *Journal of Computational Physics*, vol. 174, no. 1, pp. 226 – 247, 2001.

[73] C. Geuzaine, J. Bedrossian, and X. Antoine, "An Amplitude Formulation to Reduce the Pollution Error in the Finite Element Solution of Time-Harmonic Scattering Problems," *IEEE Transactions on Magnetics*, vol. 44, pp. 782–785, June 2008.

[74] X. Antoine and C. Geuzaine, "Phase reduction models for improving the accuracy of the finite element solution of time-harmonic scattering problems I: General approach

and low-order models," *Journal of Computational Physics*, vol. 228, pp. 3114–3136, May 2009.

[75] T. Strouboulis, I. Babuška, and R. Hidajat, "The generalized finite element method for Helmholtz equation: theory, computation, and open problems," *Computer Methods in Applied Mechanics and Engineering*, vol. 195, no. 37, pp. 4711–4731, 2006.

[76] K. Christodoulou, O. Laghrouche, M. Mohamed, and J. Trevelyan, "High-order finite elements for the solution of Helmholtz problems," *Computers & Structures*, vol. 191, pp. 129–139, 2017.

[77] M. Dinachandra and S. Raju, "Plane wave enriched Partition of Unity Isogeometric Analysis (PUIGA) for 2D-Helmholtz problems," *Computer Methods in Applied Mechanics and Engineering*, vol. 335, pp. 380–402, 2018.

[78] M. Peake, J. Trevelyan, and G. Coates, "Extended isogeometric boundary element method (XIBEM) for two-dimensional Helmholtz problems," *Computer Methods in Applied Mechanics and Engineering*, vol. 259, pp. 93–102, 2013.

[79] A. Bayliss and E. Turkel, "Radiation Boundary Conditions for Wave-Like Equations," *Communications on Pure and Applied Mathematics*, vol. 33, pp. 707–725, 1980.

[80] A. Bayliss, M. Gunzburger, and E. Turkel, "Boundary Conditions for the Numerical Solution of Elliptic Equations in Exterior Regions," *SIAM Journal on Applied Mathematics*, vol. 42, no. 2, pp. 430–451, 1982.

[81] X. Antoine, H. Barucq, and A. Bendali, "Bayliss–Turkel-like radiation conditions on surfaces of arbitrary shape," *Journal of Mathematical Analysis and Applications*, vol. 229, no. 1, pp. 184–211, 1999.

[82] M. Medvinsky and E. Turkel, "On surface radiation conditions for an ellipse," *Journal of Computational and Applied Mathematics*, vol. 234, no. 6, pp. 1647 – 1655, 2010. Eighth International Conference on Mathematical and Numerical Aspects of Waves (Waves 2007).

[83] I. Harari, "A survey of finite element methods for time-harmonic acoustics," *Computer Methods in Applied Mechanics and Engineering*, vol. 195, no. 13, pp. 1594 – 1607, 2006. A Tribute to Thomas J.R. Hughes on the Occasion of his 60th Birthday.

[84] L. L. Thompson, "A review of finite-element methods for time-harmonic acoustics," *Acoustical Society of America Journal*, vol. 119, p. 1315, 2006.

[85] D. Givoli, "High-order local non-reflecting boundary conditions: a review," *Wave Motion*, vol. 39, no. 4, pp. 319 – 326, 2004. New computational methods for wave propagation.

[86] A. E. H. Love, "The small free vibrations and deformation of a thin elastic shell," *Philosophical Transactions of the Royal Society of London. A*, vol. 179, pp. 491–546, 1888.

[87] N. Moës, J. Dolbow, and T. Belytschko, "A finite element method for crack growth without remeshing," *International journal for numerical methods in engineering*, vol. 46, no. 1, pp. 131–150, 1999.

[88] Y. Abdelaziz and A. Hamouine, "A survey of the extended finite element," *Computers & Structures*, vol. 86, no. 11-12, pp. 1141–1151, 2008.

[89] S. Mohammadi, *Extended finite element method: for fracture analysis of structures*. John Wiley & Sons, 2008.

[90] G. Zi, T. Rabczuk, and W. Wall, "Extended meshfree methods without branch enrichment for cohesive cracks," *Computational Mechanics*, vol. 40, no. 2, pp. 367–382, 2007.

[91] D. J. Benson, Y. Bazilevs, E. De Luycker, M.-C. Hsu, M. Scott, T. Hughes, and T. Belytschko, "A generalized finite element formulation for arbitrary basis functions: from isogeometric analysis to XFEM," *International Journal for Numerical Methods in Engineering*, vol. 83, no. 6, pp. 765–785, 2010.

[92] X. Peng, E. Atroshchenko, P. Kerfriden, and S. Bordas, "Isogeometric boundary element methods for three dimensional static fracture and fatigue crack growth," *Computer Methods in Applied Mechanics and Engineering*, vol. 316, pp. 151–185, 2017.

[93] N. Nguyen-Thanh, J. Huang, and K. Zhou, "An isogeometric-meshfree coupling approach for analysis of cracks," *International Journal for Numerical Methods in Engineering*, vol. 113, no. 10, pp. 1630–1651, 2018.

[94] J. Dolbow, N. Moës, and T. Belytschko, "Modeling fracture in Mindlin–Reissner plates with the extended finite element method," *International Journal of Solids and Structures*, vol. 37, no. 48-50, pp. 7161–7183, 2000.

[95] P. Baiz, S. Natarajan, S. Bordas, P. Kerfriden, and T. Rabczuk, "Linear buckling analysis of cracked plates by SFEM and XFEM," *Journal of Mechanics of Materials and Structures*, vol. 6, no. 9, pp. 1213–1238, 2012.

[96] C. Xing, Y. Wang, and H. Waisman, "Fracture analysis of cracked thin-walled structures using a high-order XFEM and Irwin's integral," *Computers & Structures*, vol. 212, pp. 1–19, 2019.

[97] P. M. Areias and T. Belytschko, "Non-linear analysis of shells with arbitrary evolving cracks using XFEM," *International Journal for Numerical Methods in Engineering*, vol. 62, no. 3, pp. 384–415, 2005.

[98] H. Bayesteh and S. Mohammadi, "XFEM fracture analysis of shells: the effect of crack tip enrichments," *Computational Materials Science*, vol. 50, no. 10, pp. 2793–2813, 2011.

[99] T. Rabczuk and P. Areias, "A meshfree thin shell for arbitrary evolving cracks based on an extrinsic basis," *CMES - Computer Modeling in Engineering and Sciences*, vol. 16,

no. 2, pp. 115–130, 2006.

[100] T. Rabczuk, P. Areias, and T. Belytschko, "A meshfree thin shell method for non-linear dynamic fracture," *International Journal for Numerical Methods in Engineering*, vol. 72, no. 5, pp. 524–548, 2007.

[101] N. Nguyen-Thanh, N. Valizadeh, M. Nguyen, H. Nguyen-Xuan, X. Zhuang, P. Areias, G. Zi, Y. Bazilevs, L. De Lorenzis, and T. Rabczuk, "An extended isogeometric thin shell analysis based on Kirchhoff–Love theory," *Computer Methods in Applied Mechanics and Engineering*, vol. 284, pp. 265–291, 2015.

[102] J. Lasry, J. Pommier, Y. Renard, and M. Salaün, "extended finite element methods for thin cracked plates with Kirchhoff–Love theory," *International Journal for Numerical Methods in Engineering*, vol. 84, no. 9, pp. 1115–1138, 2010.

[103] J. Lasry, Y. Renard, and M. Salaün, "Stress intensity factors computation for bending plates with extended finite element method," *International Journal for Numerical Methods in Engineering*, vol. 91, no. 9, pp. 909–928, 2012.

[104] V. Nguyen, C. Anitescu, S. Bordas, and T. Rabczuk, "Isogeometric analysis: an overview and computer implementation aspects," *Mathematics and Computers in Simulation*, vol. 117, pp. 89–116, 2015.

[105] J. Cottrell, T. Hughes, and Y. Bazilevs, *Isogeometric analysis: toward integration of CAD and FEA*. John Wiley & Sons, 2009.

[106] M. J. Borden, M. A. Scott, J. A. Evans, and T. Hughes, "Isogeometric finite element data structures based on Bézier extraction of NURBS," *International Journal for Numerical Methods in Engineering*, vol. 87, no. 1-5, pp. 15–47, 2011.

[107] E. M. Garau and R. Vázquez, "Algorithms for the implementation of adaptive isogeometric methods using hierarchical B-splines," *Applied Numerical Mathematics*, vol. 123, pp. 58–87, 2018.

[108] A. Buffa and C. Giannelli, "Adaptive isogeometric methods with hierarchical splines: error estimator and convergence," *Mathematical Models and Methods in Applied Sciences*, vol. 26, no. 01, pp. 1–25, 2016.

[109] A. Buffa and C. Giannelli, "Adaptive isogeometric methods with hierarchical splines: Optimality and convergence rates," *Mathematical Models and Methods in Applied Sciences*, vol. 27, no. 14, pp. 2781–2802, 2017.

[110] G. Gantner, D. Haberlik, and D. Praetorius, "Adaptive IGAFEM with optimal convergence rates: Hierarchical B-splines," *Mathematical Models and Methods in Applied Sciences*, vol. 27, no. 14, pp. 2631–2674, 2017.

[111] C. Bracco, C. Giannelli, and R. Vázquez, "Refinement algorithms for adaptive isogeometric methods with hierarchical splines," *Axioms*, vol. 7, no. 3, p. 43, 2018.

[112] J. R. Stewart and T. J. R. Hughes, "Explicit residual-based a posteriori error estimation for finite element discretizations of the Helmholtz equation: Computation of the constant and new measures of error estimator quality," *Computer Methods in Applied Mechanics and Engineering*, vol. 131, no. 3-4, pp. 335–363, 1996.

[113] W. Dörfler, "A convergent adaptive algorithm for Poisson's equation," *SIAM Journal on Numerical Analysis*, vol. 33, no. 3, pp. 1106–1124, 1996.

[114] M. L. Bittencourt, *Computational Solid Mechanics: Variational Formulation and High Order Approximation*. CRC Press, 2014.

[115] R. G. Anderson, B. Irons, and O. Zienkiewicz, "Vibration and stability of plates using finite elements," *International Journal of Solids and Structures*, vol. 4, no. 10, pp. 1031–1055, 1968.

[116] S. Osher and J. A. Sethian, "Fronts propagating with curvature-dependent speed: algorithms based on Hamilton-Jacobi formulations," *Journal of computational physics*, vol. 79, no. 1, pp. 12–49, 1988.

[117] N. Sukumar, D. L. Chopp, N. Moës, and T. Belytschko, "Modeling holes and inclusions by level sets in the extended finite-element method," *Computer Methods in Applied Mechanics and Engineering*, vol. 190, no. 46-47, pp. 6183–6200, 2001.

[118] É. Béchet, H. Minnebo, N. Moës, and B. Burgardt, "Improved implementation and robustness study of the X-FEM for stress analysis around cracks," *International Journal for Numerical Methods in Engineering*, vol. 64, no. 8, pp. 1033–1056, 2005.

[119] M. L. Williams, "The bending stress distribution at the base of a stationary crack," *Journal of applied mechanics*, vol. 28, no. 1, pp. 78–82, 1961.

[120] C. Hui and A. T. Zehnder, "A theory for the fracture of thin plates subjected to bending and twisting moments," *International Journal of Fracture*, vol. 61, no. 3, pp. 211–229, 1993.

[121] A. T. Zehnder and M. J. Viz, "Fracture mechanics of thin plates and shells under combined membrane, bending, and twisting loads," *Applied Mechanics Reviews*, vol. 58, no. 1, pp. 37–48, 2005.

[122] G. C. Sih, P. Paris, and F. Erdogan, "Crack-tip, stress-intensity factors for plane extension and plate bending problems," *Journal of Applied Mechanics*, vol. 29, no. 2, pp. 306–312, 1962.

[123] T. Chau-Dinh, G. Zi, P.-S. Lee, T. Rabczuk, and J.-H. Song, "Phantom-node method for shell models with arbitrary cracks," *Computers & Structures*, vol. 92, pp. 242–256, 2012.

[124] D. Roylance, "Transformation of stresses and strains," *Lecture Notes for Mechanics of Materials*, 2001.

[125] G. Nikishkov and S. Atluri, "Calculation of fracture mechanics parameters for an arbitrary three-dimensional crack, by the 'equivalent domain integral' method," *International Journal for Numerical Methods in Engineering*, vol. 24, no. 9, pp. 1801–1821, 1987.

[126] N. Moës, A. Gravouil, and T. Belytschko, "Non-planar 3D crack growth by the extended finite element and level sets–Part I: Mechanical model," *International Journal for Numerical Methods in Engineering*, vol. 53, no. 11, pp. 2549–2568, 2002.

[127] T. Chau-Dinh, C. Mai-Van, G. Zi, and T. Rabczuk, "New kinematical constraints of cracked MITC4 shell elements based on the phantom-node method for fracture analysis," *Engineering Fracture Mechanics*, 2018.

[128] B. Brank, A. Ibrahimbegović, and U. Bohinc, "On Discrete-Kirchhoff Plate Finite Elements: Implementation and Discretization error," in *Shell and Membrane Theories in Mechanics and Biology*, pp. 109–131, Springer, 2015.

[129] T. Huttunen, P. Gamallo, and R. Astley, "Comparison of two wave element methods for the Helmholtz problem," *Communications in Numerical Methods in Engineering*, vol. 25, no. 1, pp. 35–52, 2009.

[130] X. Antoine and C. Geuzaine, "Phase reduction models for improving the accuracy of the finite element solution of time-harmonic scattering problems I: General approach and low-order models," *Journal of Computational Physics*, vol. 228, no. 8, pp. 3114–3136, 2009.

[131] I. Harari and E. Shavelzon, "Embedded kinematic boundary conditions for thin plate bending by Nitsche's approach," *International Journal for Numerical Methods in Engineering*, vol. 92, no. 1, pp. 99–114, 2012.

[132] A. Embar, J. Dolbow, and I. Harari, "Imposing Dirichlet boundary conditions with Nitsche's method and spline-based finite elements," *International Journal for Numerical Methods in Engineering*, vol. 83, no. 7, pp. 877–898, 2010.

[133] M. J. Viz, D. O. Potyondy, A. T. Zehnder, C. C. Rankin, and E. Riks, "Computation of membrane and bending stress intensity factors for thin, cracked plates," *International Journal of Fracture*, vol. 72, no. 1, pp. 21–38, 1995.

[134] H. A. Sosa and J. W. Eischen, "Computation of stress intensity factors for plate bending via a path-independent integral," *Engineering Fracture Mechanics*, vol. 25, no. 4, pp. 451–462, 1986.

[135] N. Nguyen-Thanh, W. Li, and K. Zhou, "Static and free-vibration analyses of cracks in thin-shell structures based on an isogeometric-meshfree coupling approach," *Computational Mechanics*, pp. 1–23, 2018.

[136] H. Zhang, J. Wu, and D. Wang, "Free vibration analysis of cracked thin plates by quasi-convex coupled isogeometric-meshfree method," *Frontiers of Structural and Civil Engineering*, vol. 9, no. 4, pp. 405–419, 2015.

[137] B. Stahl and L. Keer, "Vibration and stability of cracked rectangular plates," *International Journal of Solids and Structures*, vol. 8, no. 1, pp. 69–91, 1972.

Appendix A

Geometry Parameterization employed in the Numerical Examples

Patch	Knot Vector		Control Points		
	U	V	x	y	w
1	[0,0,1,1]	[0,0,1,1]	0.0000	0.0000	1.0000
			0.0000	-1.0000	1.0000
			-1.0000	0.0000	1.0000
			-1.0000	-1.0000	1.0000
2	[0,0,1,1]	[0,0,1,1]	0.0000	0.0000	1.0000
			-1.0000	0.0000	1.0000
			0.0000	1.0000	1.0000
			-1.0000	1.0000	1.0000
3	[0,0,1,1]	[0,0,1,1]	0.0000	0.0000	1.0000
			0.0000	1.0000	1.0000
			1.0000	0.0000	1.0000
			1.0000	1.0000	1.0000

Table A.1: Geometry Information for the L-shaped domain

Patch	Knot Vector		Control Points		
	U	V	x	y	w
1	[0,0,0,0.5,1,1,1]	[0,0,1,1]	$-L$	0.0000	1.0000
			$-L$	W	1.0000
			$-L$	W	1.0000
			0.0000	W	1.0000
			-2.0000	0.0000	1.0000
			-1.7071	0.7071	0.8536
			-0.7071	1.7071	0.8536
			0.0000	2.0000	1.0000
2	[0,0,0,0.5,1,1,1]	[0,0,1,1]	0.0000	$-W$	1.0000
			$-L$	$-W$	1.0000
			$-L$	$-W$	1.0000
			$-L$	0.0000	1.0000
			0.0000	2.0000	1.0000
			-0.7071	-1.7071	0.8536
			-1.7071	-0.7071	0.8536
			-2.0000	0.0000	1.0000
3	[0,0,0,0.5,1,1,1]	[0,0,1,1]	L	0.0000	1.0000
			L	$-W$	1.0000
			L	$-W$	1.0000
			0.0000	$-W$	1.0000
			2.0000	0.0000	1.0000
			1.7071	-0.7071	0.8536
			0.7071	-1.7071	0.8536
			0.0000	-2.0000	1.0000
4	[0,0,0,0.5,1,1,1]	[0,0,1,1]	0.0000	W	1.0000
			L	W	1.0000
			L	W	1.0000
			L	0.0000	1.0000
			0.0000	2.0000	1.0000
			0.7071	1.7071	0.8536
			1.7071	0.7071	0.8536
			2.0000	0.0000	1.0000

Table A.2: Geometry Information for the thin plate problem

Patch	Knot Vector		Control Points		
	U	V	x	y	w
1	[0,0,1,1]	[0,0,0,1,1,1]	2.8532	0.9271	1.0000
			4.7553	1.5451	1.0000
			1.0000	1.0000	1.0000
			3.6327	5.0000	0.8090
			0.0000	3.0000	1.0000
			0.0000	5.0000	1.0000
2	[0,0,1,1]	[0,0,0,1,1,1]	0.0000	3.0000	1.0000
			0.0000	5.0000	1.0000
			-1.0000	1.0000	1.0000
			-3.6327	5.0000	0.8090
			-2.8532	0.9271	1.0000
			-4.7553	1.5451	1.0000
3	[0,0,1,1]	[0,0,0,1,1,1]	-2.8532	0.9271	1.0000
			-4.7553	1.5451	1.0000
			-1.3450	-0.4370	1.0000
			-5.8779	-1.9098	0.8090
			-1.7634	-2.4271	1.0000
			-2.9389	-4.0451	1.0000
4	[0,0,1,1]	[0,0,0,1,1,1]	-1.7634	-2.4271	1.0000
			-2.9389	-4.0451	1.0000
			0.0000	-1.4142	1.0000
			0.0000	-6.1803	0.8090
			1.7634	-2.4271	1.0000
			2.9389	-4.0451	1.0000
5	[0,0,1,1]	[0,0,0,1,1,1]	1.7634	-2.4271	1.0000
			2.9389	-4.0451	1.0000
			1.3450	-0.4370	1.0000
			5.8779	-1.9098	0.8090
			2.8532	0.9271	1.0000
			4.7553	1.5451	1.0000

Table A.3: Geometry Information for the Star-shaped problem

Patch	Knot Vector		Control Points			
	U	V	x	y	z	w
1	[0,0,1,1]	[0,0,1,1]	0.0000	0.0000	0.0000	1.0000
			0.0000	1.0000	0.0000	1.0000
			1.0000	0.0000	0.0000	1.0000
			1.0000	1.0000	0.0000	1.0000
			0.0000	0.0000	1.0000	1.0000
			0.0000	1.0000	1.0000	1.0000
			1.0000	0.0000	1.0000	1.0000
			1.0000	1.0000	1.0000	1.0000

Table A.4: Geometry Information for the unit cube problem

Patch	Knot Vector		Control Points		
	U	V	x	y	w
1	[0,0,0,1,1,1]	[0,0,0,1,1,1]	$-R\frac{\sqrt{2}}{2}$	$R\frac{\sqrt{2}}{2}$	1
			$-R\sqrt{2}$	0	$\frac{\sqrt{2}}{2}$
			$-R\frac{\sqrt{2}}{2}$	$-R\frac{\sqrt{2}}{2}$	1
			0	$R\sqrt{2}$	$\frac{\sqrt{2}}{2}$
			0	0	1
			0	$-R\sqrt{2}$	$\frac{\sqrt{2}}{2}$
			$R\frac{\sqrt{2}}{2}$	$R\frac{\sqrt{2}}{2}$	1
			$R\sqrt{2}$	0	$\frac{\sqrt{2}}{2}$
			$R\frac{\sqrt{2}}{2}$	$-R\frac{\sqrt{2}}{2}$	1

Table A.5: Geometry Information for the circular geometry

Patch	Knot Vector		Control Points		
	U	V	x	y	w
1	[0,0,1,1]	[0,0,0,1,1,1]	r	0	1
			$r\frac{\sqrt{2}}{2}$	$r\frac{\sqrt{2}}{2}$	$\frac{\sqrt{2}}{2}$
			0	r	1
			R	0	1
			$R\frac{\sqrt{2}}{2}$	$R\frac{\sqrt{2}}{2}$	$\frac{\sqrt{2}}{2}$
			0	R	1
2	[0,0,1,1]	[0,0,0,1,1,1]	0	r	1
			$-r\frac{\sqrt{2}}{2}$	$r\frac{\sqrt{2}}{2}$	$\frac{\sqrt{2}}{2}$
			$-r$	0	1
			0	R	1
			$-R\frac{\sqrt{2}}{2}$	$R\frac{\sqrt{2}}{2}$	$\frac{\sqrt{2}}{2}$
			$-R$	0	1
3	[0,0,1,1]	[0,0,0,1,1,1]	r	0	1
			$-r\frac{\sqrt{2}}{2}$	$-r\frac{\sqrt{2}}{2}$	$\frac{\sqrt{2}}{2}$
			0	$-r$	1
			$-R$	0	1
			$-R\frac{\sqrt{2}}{2}$	$-R\frac{\sqrt{2}}{2}$	$\frac{\sqrt{2}}{2}$
			0	$-R$	1
4	[0,0,1,1]	[0,0,0,1,1,1]	0	$-r$	1
			$r\frac{\sqrt{2}}{2}$	$-r\frac{\sqrt{2}}{2}$	$\frac{\sqrt{2}}{2}$
			r	0	1
			0	$-R$	1
			$R\frac{\sqrt{2}}{2}$	$-R\frac{\sqrt{2}}{2}$	$\frac{\sqrt{2}}{2}$
			R	0	1

Table A.6: Geometry Information for the annular geometry